

BACHELOR THESIS

---

# Aerodynamic Package of a Formula Student Racing Car

---

*Authors:*  
Romain Seppey  
Aaron Sütsch

*Supervisors:*  
Prof. Dr. Leonardo Manfredini  
Tobias Zihlmann

Project conducted in partnership with

**ZURICH UAS**  
R A C I N G

Study program:  
Bachelor of Science in Aviation UAS Zurich

## DECLARATION OF ORIGINALITY

### Bachelor's Thesis at the School of Engineering

#### DECLARATION OF ORIGINALITY

##### Bachelor's Thesis at the School of Engineering

By submitting this Bachelor's thesis, the undersigned student confirms that this thesis is his/her own work and was written without the help of a third party. (Group works: the performance of the other group members are not considered as third party).

The student declares that all sources in the text (including Internet pages) and appendices have been correctly disclosed. This means that there has been no plagiarism, i.e. no sections of the Bachelor thesis have been partially or wholly taken from other texts and represented as the student's own work or included without being correctly referenced.

Any misconduct will be dealt with according to paragraphs 39 and 40 of the General Academic Regulations for Bachelor's and Master's Degree courses at the Zurich University of Applied Sciences (Rahmenprüfungsordnung ZHAW (RPO)) and subject to the provisions for disciplinary action stipulated in the University regulations.

**City, Date:**

Winterthur, 09.06.2023

Winterthur, 09.06.2023

**Name Student:**

Romain Seppey

Aaron Süttsch

# Abstract

Formula Student is the largest engineering competition in the world. Student teams design and create their race cars to participate in events that take place worldwide. Zurich UAS Racing competes in these events with a new racing car each year and thus needs continuously improved mechanical and electrical systems. The aerodynamic package of the 2022/2023 car was designed by several team members in previous projects mainly by means of Computational Fluid Dynamics (CFD). This thesis aims to validate the results obtained by building a 1:4 scale model of the car and testing it in the low-speed wind tunnel of the ZHAW School of Engineering. The model was fitted with modular axles, which allowed an investigation of the influence of the ride heights (RH) and rake angles (RA). For this purpose, a study of the forces acting on the model was conducted, as well as of the pressure distribution along the underbody and airflow visualisation. Additionally, a CFD simulation of the scale model were conducted to compare it with the results obtained experimentally. Measurements were done between 17 and 23 m/s to investigate the effect of changing Reynolds number on downforce and drag. To represent reality as accurately as possible, the results with the highest Reynolds numbers were used to compare the overall performance. The results reveal the influence of the model configuration on downforce and drag, further indicating that increasing RA leads to increased downforce, with the highest efficiency achieved at RA 3°. Furthermore, the RA has a larger influence at lower RH, where the performance can be increased up to 10%. The pressure distribution analysis along the underbody demonstrates the effectiveness of the infuser and diffuser for different RH and RA. The qualitative analysis of flow visualisation using tufts helps comprehending the behaviour of the airflow around the model and determining potential turbulent or separated flow regimes. Overall, the results obtained from this comprehensive investigation contribute to a deeper understanding of this year's Zurich UAS Racing Formula Student racing car performance and provide valuable insights for optimising the setup. Despite some divergences with respect to the CFD simulations, attributable to a variety of factors, the results are comparable and thus valid.

# Zusammenfassung

Formula Student ist der grösste Ingenieurwettbewerb der Welt. Studententeams entwerfen und konstruieren ihre Rennwagen für die Teilnahme an Veranstaltungen, die weltweit stattfinden. Zurich UAS Racing nimmt jedes Jahr mit einem neuen Rennwagen an diesen Veranstaltungen teil und benötigt daher ständig verbesserte mechanische und elektrische Systeme. Das aerodynamische Paket des Rennwagens 2022/2023 wurde von mehreren Teammitgliedern in früheren Projekten hauptsächlich mit Hilfe von Computational Fluid Dynamics (CFD) entworfen. Diese Arbeit zielt darauf ab, die erzielten Ergebnisse zu validieren, indem ein Modell des Fahrzeugs im Massstab 1:4 gebaut und im Niedergeschwindigkeits-Windkanal der ZHAW School of Engineering getestet wird. Das Modell wurde mit modularen Achsen ausgestattet, was eine Untersuchung des Einflusses der Ride Height (RH) und des Rake Angles (RA) ermöglichte. Dazu wurde eine Studie der auf das Modell wirkenden Kräfte, der Druckverteilung entlang des Unterbodens und der Strömungsvisualisierung durchgeführt. Außerdem wurden CFD-Simulationen des massstabgetreuen Modells durchgeführt, um die Ergebnisse mit den experimentell gewonnenen zu vergleichen. Es wurden Messungen zwischen 17 und 23 m/s durchgeführt, um die Auswirkungen einer Änderung der Reynoldszahl auf den Abtrieb und den Luftwiderstand zu untersuchen. Um die Realität so genau wie möglich abzubilden, wurden die Ergebnisse mit den höchsten Reynoldszahlen zum Vergleich der Gesamtleistung herangezogen. Die Ergebnisse zeigen den Einfluss der Modellkonfiguration auf den Anpressdruck und den Luftwiderstand und weisen darauf hin, dass eine Erhöhung des RA zu einem erhöhten Anpressdruck führt, wobei die höchste Effizienz bei RA  $3^\circ$  erreicht wird. Darüber hinaus hat der RA einen größeren Einfluss bei niedrigeren RH, wo die Leistung um bis zu 10% gesteigert werden kann. Die Druckverteilungsanalyse entlang des Unterbodens zeigt die Effektivität des Inpusors und des Diffusors für verschiedene RH und RA. Die qualitative Analyse der Strömungsvisualisierung mit Hilfe von Tufts hilft, das Verhalten der Luftströmung um das Modell zu verstehen und potenzielle turbulente oder getrennte Strömungsregime zu bestimmen. Insgesamt tragen die Ergebnisse dieser umfassenden Untersuchung zu einem tieferen Verständnis der Leistung des diesjährigen Zurich UAS Racing Formula Student-Rennwagens bei und liefern wertvolle Erkenntnisse zur Optimierung des Setups. Trotz einiger Abweichungen gegenüber den CFD-Simulationen, die auf verschiedene Faktoren zurückzuführen sind, sind die Ergebnisse vergleichbar und damit gültig.

# Acknowledgements

We would like to express our gratitude to our thesis supervisor, Prof. Dr. Leonardo Manfriani, for his invaluable guidance, expertise, and continuous support throughout the entire project.

We are also very grateful to Mr. Tobias Zihlmann for his assistance and insightful feedback during the course of this research. His attention to detail and constructive criticism have greatly contributed to the refinement of our work.

We would like to extend our sincere appreciation to Mr. Marco Giachi for his valuable input and expertise as an external advisor for this thesis. His expertise in motorsport aerodynamics and wind tunnel testing has provided us with valuable perspectives and enriched the quality of our study.

Furthermore, we would like to express our heartfelt appreciation to our colleagues and friends from Zurich UAS Racing. Special thanks to Sean de Jong, Thomas Rüdts, Nicola Schneider, Fabrice Grübel and Basil Tschudi, your support has been indispensable, and we are truly grateful for the opportunity to have worked with such remarkable individuals.

Finally, we would like to express our heartfelt appreciation to all the other people who also contributed directly or indirectly to the completion of this thesis. Among them, Mr. Michael Ammann and Mr. Adrian Schödler, Mr. Hanspeter Sautter and his associates from the Institute of Product Development and Production Technologies and Mr. Hans-Werner Dyck.

# Contents

<b>Declaration of Originality</b>	<b>i</b>
<b>Abstract</b>	<b>ii</b>
<b>Zusammenfassung</b>	<b>iii</b>
<b>Acknowledgements</b>	<b>iv</b>
<b>Contents</b>	<b>v</b>
<b>1 Introduction</b>	<b>1</b>
1.1 Project Framework . . . . .	1
1.2 Aim . . . . .	2
1.3 Overview . . . . .	2
<b>2 Theoretical Principles</b>	<b>3</b>
2.1 Racing Car Aerodynamics . . . . .	3
2.1.1 Downforce and Drag Calculation . . . . .	6
2.1.2 Ground Effect . . . . .	7
2.1.3 Vortex Generators . . . . .	7
2.1.4 Gurney Flap . . . . .	8
2.2 Wind Tunnel . . . . .	10
2.2.1 Wind Tunnel Types . . . . .	10
2.2.2 Wind Tunnel Models . . . . .	11
2.2.3 Similarity Parameters . . . . .	12
2.2.4 Motorsport Application . . . . .	12
<b>3 Methods</b>	<b>14</b>
3.1 Model Design and Construction . . . . .	14
3.1.1 3D Modelling . . . . .	14
3.1.2 Wheel Drive System . . . . .	15
3.1.3 Model Test Configurations . . . . .	17
3.1.4 Manufacturing and Assembly . . . . .	19
3.2 Measuring Equipment . . . . .	20
3.2.1 ALFA Wind Tunnel . . . . .	20
3.2.2 RUAG Balance . . . . .	20
3.2.3 <i>MicroDaq</i> Pressure Scanner . . . . .	21
3.2.4 Power Supply . . . . .	24
3.2.5 GTC TA110 Laser Tachometer . . . . .	25
3.2.6 <i>MATLAB</i> . . . . .	26
3.2.7 Tufts . . . . .	26
3.2.8 <i>GoPro</i> Camera . . . . .	27

3.3	Test Setup . . . . .	28
3.3.1	Test Section Setup . . . . .	28
3.3.2	Flow Similarity . . . . .	29
3.3.3	Testing Procedure . . . . .	30
3.4	Data . . . . .	31
3.4.1	Data Filtering . . . . .	31
3.4.2	Repetition Measurement . . . . .	32
3.4.3	Influence of the Reynolds number . . . . .	32
<b>4</b>	<b>Results</b>	<b>35</b>
4.1	Aerodynamic Forces . . . . .	35
4.1.1	Downforce and Drag depending on Model Configuration . . . . .	35
4.1.2	Contour Plots . . . . .	37
4.1.3	Downforce Distribution . . . . .	39
4.2	Pressure Distribution . . . . .	40
4.3	CFD Results . . . . .	42
4.4	Flow Visualisation . . . . .	43
<b>5</b>	<b>Discussion and Conclusion</b>	<b>47</b>
5.1	Validity . . . . .	47
5.1.1	Wind Tunnel Model . . . . .	47
5.1.2	Wind Tunnel Testing Setup . . . . .	47
5.1.3	Reynolds Effect . . . . .	47
5.1.4	Comparison with CFD Results . . . . .	48
5.2	Improvements . . . . .	50
5.2.1	Model Manufacturing . . . . .	50
5.2.2	Test Section Setup . . . . .	50
5.2.3	CFD Simulation . . . . .	50
5.3	Conclusion . . . . .	52
5.3.1	Performance . . . . .	52
5.3.2	Goals and Research Questions . . . . .	52
	<b>Bibliography</b>	<b>54</b>
	<b>List of Figures</b>	<b>57</b>
	<b>List of Tables</b>	<b>60</b>
	<b>List of Abbreviations</b>	<b>61</b>
	<b>Physical Constants</b>	<b>62</b>
	<b>List of Symbols</b>	<b>63</b>
<b>A</b>	<b>Basic Aerodynamics Knowledge</b>	<b>64</b>
A.1	Continuity Equation . . . . .	64
A.2	Bernoulli Principle . . . . .	66
A.3	Laminar and Turbulent Flow . . . . .	67
A.4	Reynolds Number . . . . .	68
A.5	Boundary Layer . . . . .	69
A.5.1	Displacement Thickness . . . . .	70

<b>B</b>	<b>Project Management</b>	<b>71</b>
B.1	Project Objectives . . . . .	71
B.2	Research Questions . . . . .	72
B.3	Project Gantt Chart . . . . .	73
B.4	Project Risk Matrix . . . . .	74
B.5	Wind Tunnel . . . . .	75
	B.5.1 Wind Tunnel Schedule . . . . .	75
	B.5.2 Wind Tunnel Test Matrix . . . . .	76
<b>C</b>	<b>MATLAB Scripts</b>	<b>77</b>
C.1	Wind Tunnel Model . . . . .	77
	C.1.1 Axle Height . . . . .	77
	C.1.2 Drive System . . . . .	78
C.2	Setup . . . . .	79
	C.2.1 Displacement Thickness . . . . .	79
	C.2.2 Mach Number . . . . .	79
C.3	Data Processing . . . . .	80
	C.3.1 Files Reading . . . . .	80
	C.3.2 Filtering . . . . .	80
	C.3.3 Repetition Measurement . . . . .	82
	C.3.4 RH 12.5 mm, all RA . . . . .	84
	C.3.5 Overall Comparison . . . . .	90
	C.3.6 Pressure Distribution . . . . .	92
<b>D</b>	<b>Additional Plots</b>	<b>97</b>
D.1	Filtering . . . . .	97
D.2	Boxplots . . . . .	100
D.3	Line Plots . . . . .	102



# Chapter 1

## Introduction

### 1.1 Project Framework

Formula Student (FS) is the largest engineering competition in the world. Teams of engineering students from all over the world design, create and test their race cars to compete in a championship with events worldwide, during which not only the performance of the car is assessed, but also the design of its various systems, its efficiency and the operational aspects of the project. The authors of this thesis cooperate with Zurich UAS Racing (ZUR) [1], the Formula Student team of the Zurich University of Applied Sciences (ZHAW), and in the European regulatory framework of FS issued by Formula Student Germany (FSG) [2]. This bachelor thesis continues in the line of the project thesis conducted in 2022 by the same authors [3], in which the underbody and diffuser of the racing car were designed and simulated by means of Computational Fluid Dynamics (CFD) using *Ansys CFX*.



FIGURE 1.1: Zurich UAS Racing Formula Student racing car for the 2022/2023 season

## 1.2 Aim

The goal of the present thesis is to experimentally test the final aerodynamic package of the car in the low-speed wind tunnel made available by the ZHAW Centre for Aviation (ZAV). Since the full-scale car does not fit in the test section of the wind tunnel, a 1:4 scale model was made to simulate the actual aerodynamic qualities under controlled conditions, so as to reproduce real conditions that the race car will experience. To that end, the geometry of the model should be as accurate as possible with respect to the ZUR racing car; however, some compromises had to be made in the manufacturing to keep the complexity level within achievable limits. Moreover, the wind tunnel model should have modular axles to investigate the effect of modifying the ride height (RH) and rake angle (RA). These concepts will be explained in more details in Section 3.1.3.

This thesis will mainly answer the following research questions:

- What are key considerations when building a wind tunnel model of a racing car, and how can they affect the accuracy and reliability of the test results?
- How can 3D printing and other advanced manufacturing techniques be used to build a high-fidelity wind tunnel model of a racing car?
- What are the potential limitations and trade-offs of building a wind tunnel model of a racing car, and how can they be minimised or mitigated?
- How does adjusting the ride height affect the aerodynamic performance of a racing car in a wind tunnel test?
- What is the optimal rake angle for a racing car in a wind tunnel test, and how does it affect the car's aerodynamic performance?

Further research questions were formulated and can be found in Appendix B.2.

## 1.3 Overview

The present thesis is structured as follows: Chapter 2 outlines the theoretical frame of the project and explains relevant aerodynamic principles applied to motorsports and theory about wind tunnels. Chapter 3 describes the methods used for the design and manufacturing of the model as well as the measuring equipment, the process during the wind tunnel testing and data-processing, while the results are presented in Chapter 4. In Chapter 5, a discussion determines the validity of the results and what can be improved for future projects.

## Chapter 2

# Theoretical Principles

This chapter is based on the basic principles of aerodynamics applied to motorsports as well as basic theory of wind tunnel testing. In order to fully understand the content of this thesis, a basic knowledge of classical physics and fluid mechanics is necessary; additional key aerodynamics principles are introduced in Appendix A. Since both authors of this thesis are aeronautical engineering students, the variables used in the equations may be different from other study fields. Therefore, a list of variables, constants and their respective units can be found at the end of the thesis. Moreover, part of the theory presented in this chapter is an updated version of that from the project thesis that was added here by the same authors [3] in order to provide a complete understanding without the reader having to review both documents.

### 2.1 Racing Car Aerodynamics

The purpose of this section is to provide theoretical knowledge on the main interaction of the forces acting on a racing car. A coordinate system first has to be defined to reach an agreement on the direction of the force vectors. Figure 2.1 displays the coordinate system of a racing car as used in this study as well as the main forces acting along its axes. Note that the length of the force vectors as well as the position of the centres illustrated below do not represent reality.

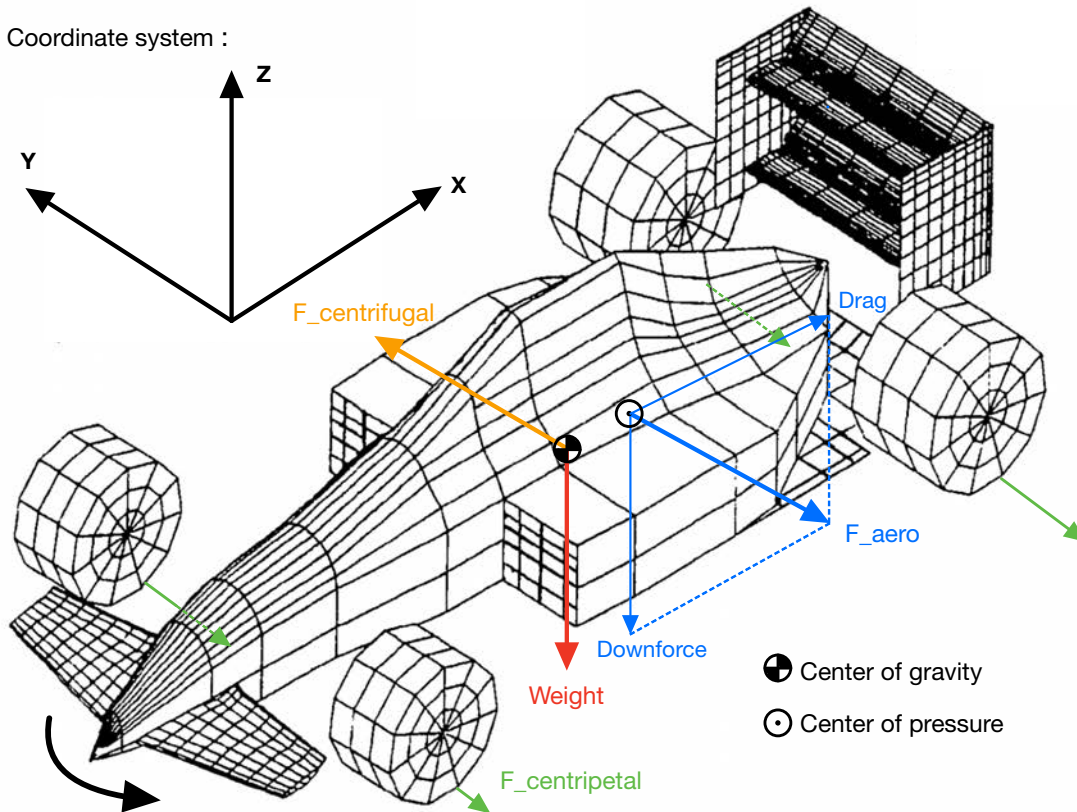


FIGURE 2.1: Main mechanical and aerodynamic forces acting on a racing car, illustration from [4] annotated with vectors and labels for clarity purposes

During driving, braking and cornering, friction forces are generated between the track and the tyres. If those forces become too high, especially while turning, the car risks losing its grip and therefore manoeuvrability. To prevent that, the car would have to be loaded with extra weight so that its gravitational force would increase and allow higher friction forces. However, increasing the weight is not a viable option since it diminishes the performance of the car. Therefore, a downward pressure is created on the car by the air flowing over its surfaces, what is known as downforce, which allows it to increase its cornering speed and thus racing performance. To quantify the amount of downforce applied to a certain surface or object, the equation of aerodynamic lift is used, but instead of resulting in an upwards force, this “lift” points downwards. Therefore, the equation of downforce is identical to the inverse of the lift equation. However, for the sake of clarity, instead of using the lift coefficient  $C_l$ , the downforce coefficient  $C_z$  with an opposite sign to his counterpart will be preferred. Needless to say that in a sports at the forefront of performance such as *Formula 1*, a downforce increase, no matter how small, makes for a winning car.

$$F_{lift} = \frac{1}{2}\rho V^2 C_l S \quad (2.1)$$

$$F_{downforce} = -F_{lift} = -\frac{1}{2}\rho V^2 C_l S = \frac{1}{2}\rho V^2 C_z S \quad (2.2)$$

Drag, on the other side, is a less desirable effect. It is physically defined as the friction of the car with the surrounding air and its magnitude is directly proportional to the surface area in contact with the airflow. Hence, in aircraft and car design, manufacturers try to limit the area which is exposed to the flow as much as possible to improve the performance of the body, especially at high speeds. Moreover, as explained by [5], *Formula 1* cars generally have a higher coefficient of drag compared to grand touring (GT) racing cars (on the left in Figure 2.2), because their wheels are not covered. The main difference between these is mainly the amount of downforce created. To provide a reference, the Downforce-to-Drag ratio ( $F_{downforce}/F_{drag}$ ) results in 3:1 for a *Formula 1* car and 0.6:1 for a GT racing car.

$$F_{drag} = \frac{1}{2}\rho V^2 C_x S \quad (2.3)$$



FIGURE 2.2: Difference between a GT race car (left) and a *Formula 1* race car (right) [5]

Both these equations (2.1 and 2.3) contain the same variables, apart from the downforce/drag coefficients. The reason behind this is that they both represent a force resulting from the interaction of the body with the airflow. Indeed,  $\frac{1}{2}\rho V^2$  represents the dynamic pressure  $q$ , which is essentially the kinetic energy of the incoming airflow, while  $C_{l/x}S$  depend on the exposed surface's geometry, position and area. The sum of downforce and drag is called the "aerodynamic force"  $F_{aero}$  [6].

Next, the centrifugal and centripetal forces will be introduced. These forces are opposed by definition and express the forces felt by the car in a turn of a certain radius. The centrifugal force is essentially the force that must be counterbalanced to avoid losing grip, whereas the centripetal force is the one that keeps the racing car on the track. The total centripetal force is the sum of the grip generated by each tyre in a turn. It can be quantified as the amount of vertical load multiplied by the friction coefficient of the track. Hence, an equilibrium equation between the centrifugal and centripetal force can be expressed that describes the circumstances in which the car is able to turn with a certain cornering speed  $V$ .

Thus for  $F_{centrifugal} = F_{centripetal}$ :

$$\frac{V^2}{R} = (mg + \frac{1}{2}\rho V_{\infty}^2 C_z S) \quad (2.4)$$

The above equation clearly shows that to allow as high a turning speed as possible, the absolute value of the downforce coefficient  $C_z$  must be maximised since all



the other variables are considered constant and non-modifiable. To demonstrate the essential role of aerodynamic downforce, the following *MATLAB* plot displays the maximum allowable cornering speeds for different turn radii for a variety of downforce coefficients.

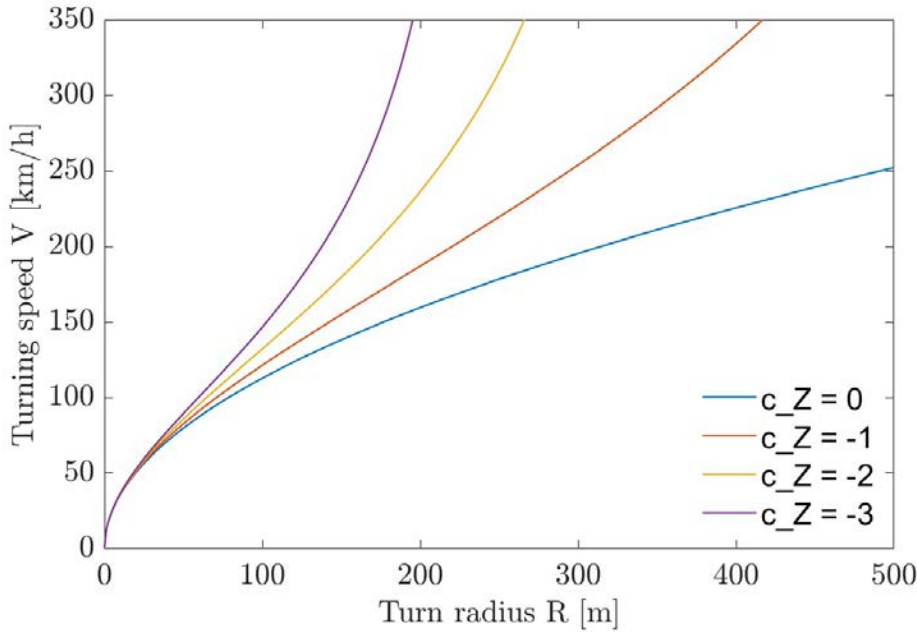


FIGURE 2.3: Turning speed vs turn radius for different downforce coefficients ( $C_z$ )

### 2.1.1 Downforce and Drag Calculation

From the above equations on lift and drag, it is possible to isolate the coefficients as follows:

$$C_l = \frac{F_{lift}}{qS} = \frac{F_{lift}}{\frac{1}{2}\rho V^2 S} \quad (2.5)$$

$$C_x = \frac{F_{drag}}{qS} = \frac{F_{drag}}{\frac{1}{2}\rho V^2 S} \quad (2.6)$$

In the automotive application, the downforce coefficient  $C_z$  will be favored. Note that the downforce coefficient is negative since the downforce vector points in the direction opposite to the reference coordinate system (see Figure 2.1).

$$C_z = \frac{F_{downforce}}{qS} = \frac{F_{downforce}}{\frac{1}{2}\rho V^2 S} \quad (2.7)$$

Given that the lifting force of an aircraft is nothing else than the result of a pressure difference between the lower side and the upper side of the wing profile, the lift

(respectively downforce) can also be determined with the pressure coefficient  $C_p$  as follows. The exhaustive equation development is available in Appendix A.2.

$$C_p = \frac{p - p_\infty}{q_\infty} = \frac{p - p_\infty}{\frac{1}{2}\rho_\infty V_\infty^2} \quad (2.8)$$

### 2.1.2 Ground Effect

In aerodynamics, the ground effect describes the particular phenomenon that occurs when a wing approaches a flat surface. First and foremost, however, it is necessary to discern the aircraft ground effect from the racing car ground effect. The first occurs when an airplane is relatively close to the ground (within a distance of one to two wingspans). The ground interacts with the airflow surrounding the wing, disturbing its wingtip vortices, which in turn reduces the induced drag, increasing the lift-to-drag ratio. However, the racing car ground effect does not exactly work the same way. When a race car's underbody travels close to the ground, the airflow moving over its lower side (lower pressure) is constrained by the ground, which forces it to accelerate and thus decreases the local pressure. As a result, the difference between the lower pressure which prevails under the car and the higher pressure on the upper side of the car generates downforce. [7]. If this concept is efficiently applied, the resulting downforce can become considerable, as was the case with the Lotus 79, shown in Figure 2.4, that dominated the *Formula 1* championship in the year it was designed. Indeed, both phenomena work in accordance with the Bernoulli principle (see Appendix A.2), only their applications differ. The denomination "wing car" was sometimes used to describe the aerodynamic concept.

**LOTUS 79**

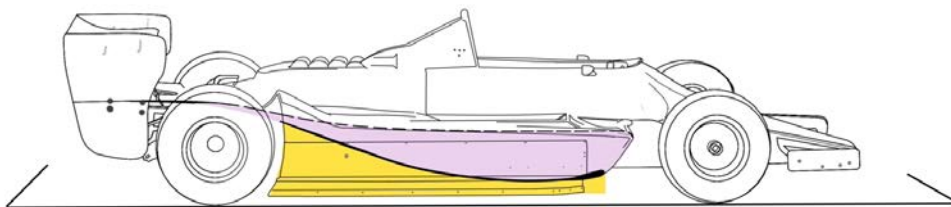


FIGURE 2.4: Lotus 79, first racing car to utilise the ground effect on the sidepods in the 1977/1978 *Formula 1* season [7]

### 2.1.3 Vortex Generators

Vortex generators are small aerodynamic devices that allow the flow to remain attached longer to a surface before separating. Generally a bit taller than the boundary layer and located near the expected separation point, they utilise the free stream to generate a vortex and transmit momentum to the boundary layer, enabling it to delay flow separation [4]-[8]. In addition to preventing the detrimental generation of drag allocated to flow separation to take place, vortex generators also enhance lift at high lift coefficients (downforce in the case of racing car aerodynamics) as a result of

smaller separated flow regions. A comparison between an airfoil with and without vortex generators at different angles of attack is illustrated in Figure 2.5.

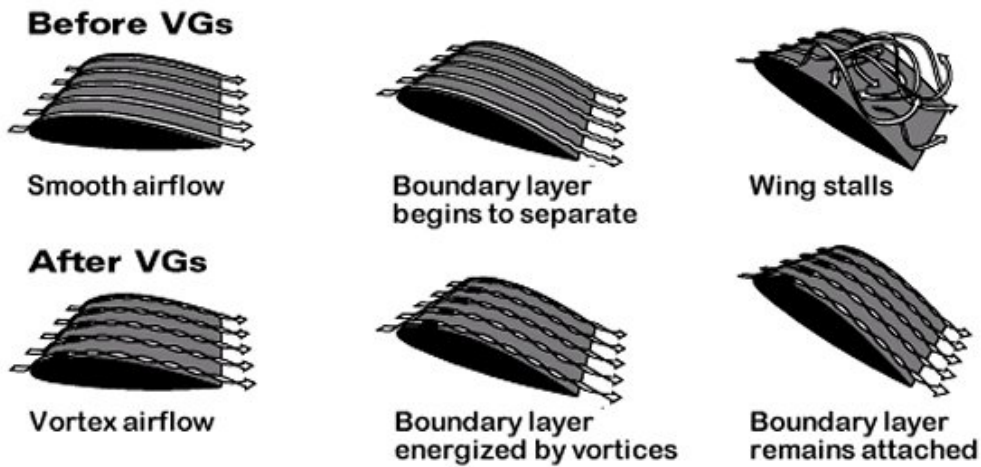


FIGURE 2.5: Illustration of the effect of vortex generators (VGs) on a wing with increasing angle of attack [8]

Their geometry varies from basic wing profiles to fancier shapes as can be seen in Figure 2.6 below.

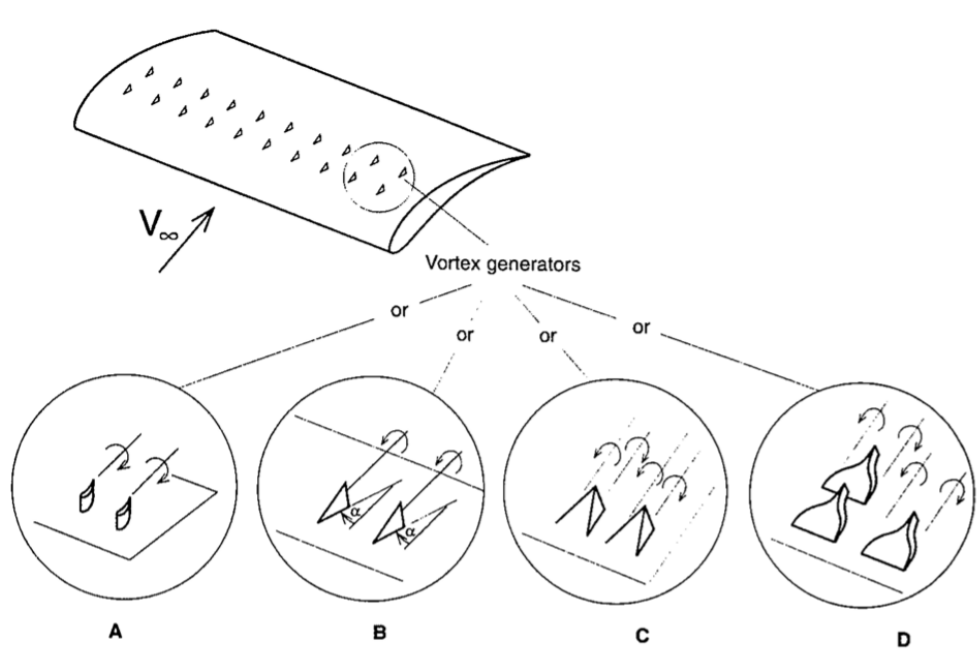


FIGURE 2.6: Main vortex generator types used on wings or other aerodynamic surfaces [4]

### 2.1.4 Gurney Flap

A Gurney flap, sometimes also referred to as “nolder”, is a small angular element usually positioned on the trailing edge of a wing or other aerodynamic surface. Named after its inventor Dan Gurney, founder of the *All American Racers* team in the 1970s [9], this device consists of a small rectangular surface (usually between 1%



and 5% of the airfoil chord length) positioned perpendicular to the airflow. Although it seems counter-intuitive, this flap generates downforce at the cost of a minor drag increase [4]. Counter-rotative vortices are created on the upper and lower sides of the wing, amplifying the aerodynamic circulation around the profile and creating extra downforce, as depicted in Figures 2.7 and 2.8. It was initially mainly used to easily adjust the aerodynamic load to prevent over- or understeering without having to change the angle of incidence of an airfoil [9]. It is one of the very few innovations to originate from motorsports and to have found an application in other sectors, like aeronautics, instead of the other way around. Further research was conducted by the authors of this thesis on the possible implementation of Gurney flaps on the rear wing of the 2023 Zurich UAS Racing car by means of CFD and is available on request [10].

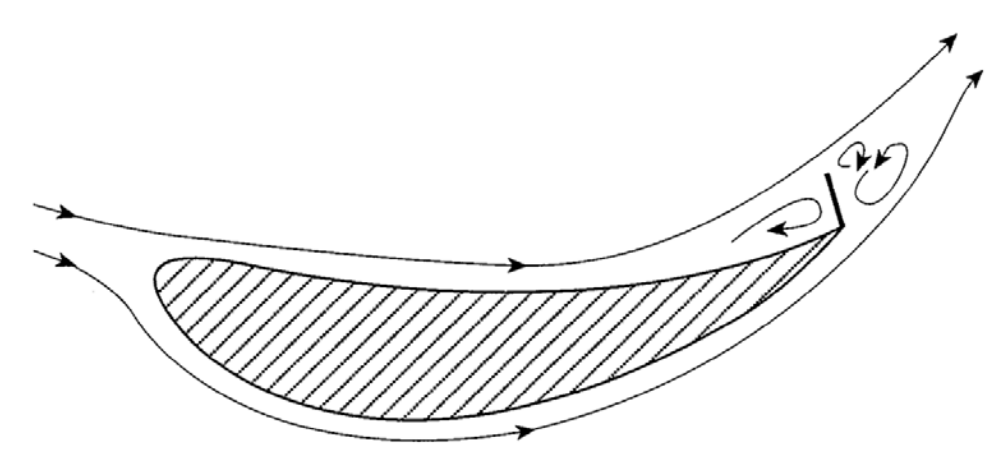


FIGURE 2.7: Theoretical effect of a Gurney flap on the airflow circulation around a wing [4]

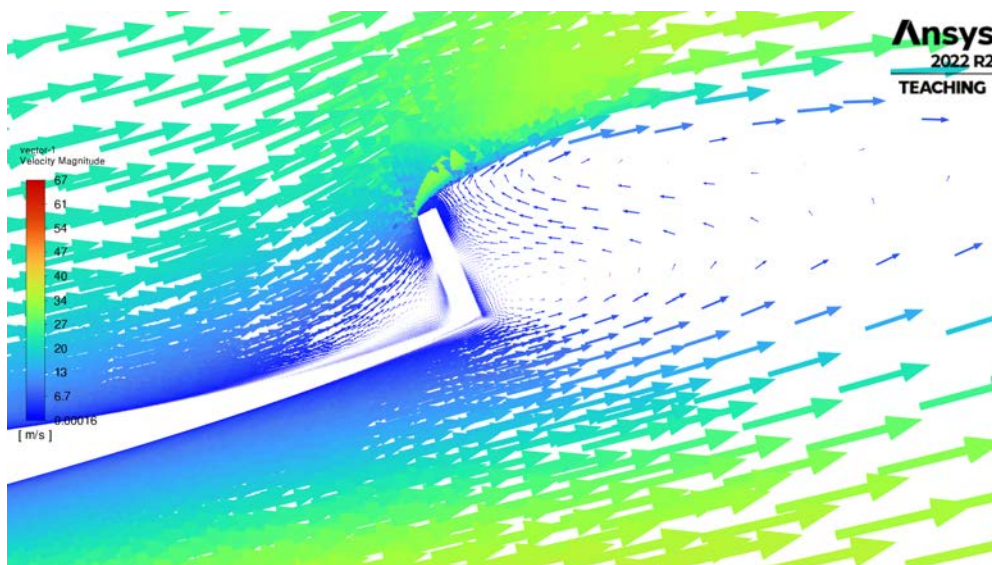


FIGURE 2.8: Actual effect of a Gurney flap on the airflow at the trailing edge of a wing profile, visualised by means of CFD (Ansys Fluent) [10]

## 2.2 Wind Tunnel

A wind tunnel is a facility that is used to test, develop and optimise components or systems experimentally. The principle of operation is to propel air onto a fixed test specimen in order to study its aerodynamic characteristics and how it interacts with the flow under specific, controlled conditions. It utilises the principle of mechanical relativity, which states that an object moving through air at a certain speed is no different than air being moved towards said object at the same speed. In the following sections, different aspects of wind tunnel testing will be introduced.

### 2.2.1 Wind Tunnel Types

Wind tunnels are devices used to simulate the flow of air around an object in a controlled environment. They are widely used in aerodynamics and fluid mechanics research, as well as in the design and testing of aircraft, cars, rockets, and other vehicles. Wind tunnels of all sizes exist, the biggest one being capable of testing aircraft as large as a Boeing 737 (NASA National Full-Scale Aerodynamics Complex in California [11], see Figure 2.9). In terms of velocity, wind tunnels range from the low subsonic regime ( $M \ll 1$ ) all the way to the hypersonic regime ( $M > 5$ ), depending on their intended use.

- Open circuit wind tunnels: In an open circuit wind tunnel, air is drawn into the tunnel from the surrounding environment and then released out the other end.
- Closed circuit wind tunnels: In a closed circuit wind tunnel, air is recirculated within the tunnel, which helps to maintain a consistent flow environment.
- Open test section wind tunnels: In an open test section wind tunnel, the test section is exposed to the surrounding environment, meaning that there are no physical walls or boundaries enclosing the test section.
- Closed test section wind tunnels: In a closed test section wind tunnel, the test section is enclosed by walls on all sides. The airflow is contained within the test section, and the walls help to guide and control the flow.
- Vertical wind tunnels: Some wind tunnels are turned vertical, most commonly to study spin recovery after an aircraft stall.
- Cryogenic wind tunnels: Operating with a low-temperature pure nitrogen flow, a cryogenic wind tunnel can faithfully reproduce real high-lift and high-speed flight characteristics of modern transport aircraft, as characterised by the Mach number and the Reynolds number. When the temperature of the gas flow decreases, the viscosity of the gas as well as the speed of sound decrease and the density increases, that enables the Reynolds number to grow rapidly while reducing the velocity required to simulate a flight at high Mach number (see Section 2.2.3) [12].

These are just a few examples of the various kinds of wind tunnels that are employed in the study of aerodynamics. Every type of wind tunnel has unique characteristics and benefits, and the choice of wind tunnel depends on the individual research goals and test program needs.



FIGURE 2.9: Full-scale F/A-18 fighter aircraft undergoing high angle of attack (AOA) wind tunnel tests at NASA's Ames Research Center [11]

### 2.2.2 Wind Tunnel Models

In order to obtain relevant wind tunnel data, the wind tunnel model should fulfill some requirements. Most importantly, the wind tunnel model should have a geometric shape and dimensions that accurately represent the real object or system being studied. To effectively mimic the flow behaviour around the item, the model must include all necessary elements, including surface contours, proportions, and appendages. Also, the model should be made of materials that guarantee a certain stability and robustness to avoid vibrations and ensure that it endures the testing process. Commonly used materials are aluminum and titanium alloys, steel and composite materials like carbon fibre. Moreover, mounting points must be provided to secure the model in a balanced manner and without disrupting the airflow.



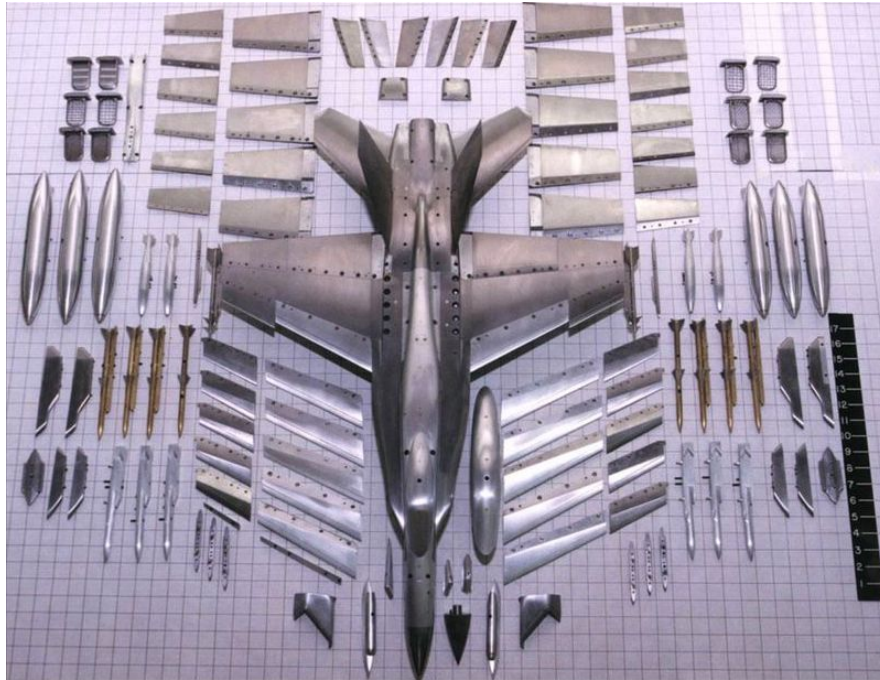


FIGURE 2.10: F/A-18 wind tunnel scale model with interchangeable parts to reproduce different flight configurations [13]

### 2.2.3 Similarity Parameters

For practical reasons, a lot of objects or systems that are to be tested in a wind tunnel must be scaled first. In order to appropriately reproduce the aerodynamic forces acting on the full-scale object, similarity parameters are required [12]. These are as follows:

1. Geometry
2. Reynolds number  $Re = \frac{\rho V l}{\mu}$
3. Mach number  $M = \frac{V}{a}$  (with  $a = \sqrt{\gamma R T}$ )

First, the most obvious and important is the geometrical similarity. Two bodies are said to be "geometrically similar" if the geometry of one can be achieved by applying a certain scale factor to the geometry of the other [14]. This condition is a prerequisite to obtaining flow similarity. Second, the Reynolds number (explained in more details in Appendix A.4) accounts for the viscosity of the flow [15] and other characteristics such as flow separation [5]. In order to achieve similitude between two flows, their respective  $Re$  must match. Finally, the same condition must apply to their respective  $M$ , representing the compressibility effects. Note that other similarity parameters such as Froude or Weber numbers also exist for special study cases of fluid dynamics [14].

### 2.2.4 Motorsport Application

Wind tunnel testing is a primordial aspect of developing and optimising racing cars because it allows engineers to investigate the aerodynamics of the car in a controlled environment. By simulating different driving conditions and wind speeds, wind

tunnel testing may give vital insights into how the car will behave on the track and assist engineers in making design adjustments that can improve its overall performance and handling. In *Formula 1* for example, in order to reduce the gaps between the teams, the *Fédération Internationale de l'Automobile* (FIA) approved a rule that reduces the wind tunnel testing time of the leading teams and increases that of less successful teams [16]. This demonstrates the importance of aerodynamic testing and optimisation in the success of a racing car. As a result, due to the high costs and limited time associated to wind tunnel operation, teams tend to first design and simulate the aerodynamic package by means of CFD before experimentally evaluating the race car [17].



FIGURE 2.11: Scale model of a *Formula 1* car in a wind tunnel with moving belt, courtesy of Mr. Marco Giachi, standing in the picture

Wind tunnel testing for racing cars often entails creating scale models of the car to be placed in the wind tunnel's test section. These models are meticulously outfitted with pressure sensors, flow visualisation tools, and other measuring equipment, allowing engineers to investigate how air flows around the car and identify areas for improvement. Moreover, for the sake of fidelity, most of the wind tunnels used for motorsports are equipped with a moving belt to simulate the ground travelling at free stream velocity under the car, as can be seen in Figure 2.11.

## Chapter 3

# Methods

### 3.1 Model Design and Construction

#### 3.1.1 3D Modelling

The first step in the design of the wind tunnel model consisted in scaling and adjusting the real car by means of Computer-Aided Design (CAD) into a 3D-model that would represent reality as accurately as possible. The software platform *3DEXPERIENCE* by *Dassault Systèmes* [18] was used to create, assemble and test the interactions between the parts. Once an individual part was ready, it was 3D printed.

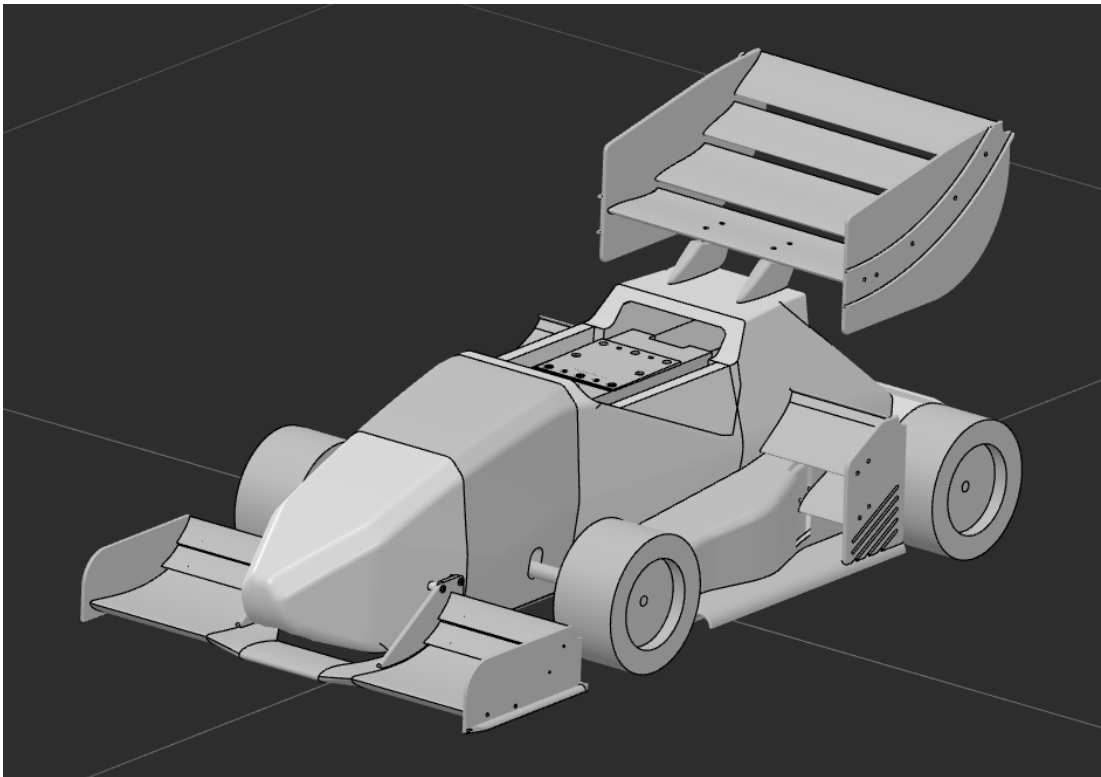


FIGURE 3.1: Final version of the 3D wind tunnel model, designed and assembled on *3DEXPERIENCE*

The geometric similarity (see Section 2.2.3) was respected as far as possible. However, some measures were adopted to ensure the stability and stiffness of the model, which run counter to geometric similarity. For example, the guide vanes under the



sidepods on the full-scale race car are 2 mm thick, scaling this for the model would yield a thickness of 0.5 mm, which is inconvenient for the manufacturing and assembly process. For this reason, a minimal thickness of 2 mm was selected for the most sensitive parts. In addition to the absence of the helmet, which is supposed to represent the driver, the front and rear wing attachments have been constructed differently on the model than on the car, for the sake of simplicity.

### 3.1.2 Wheel Drive System

In order to come closer to reality, the model should have rotating wheels. However, printing wheels in 3D not being a viable solution because of the high instability due to the inconsistent printing infill, it was decided that already existing remote-controlled (RC) car wheels with similar dimensions should be used. The drive system consisted of two axles and two motors, recovered from the previous year's wind tunnel model [19], four pulleys (one per motor and axle) and two timing belts. Moreover, in order for the belts to be tensioned regardless of the height of the axles, the motors were movable on the rectangular metal tube. The *MATLAB* script used to calculate the required belts length can be found in Appendix C.1.2.

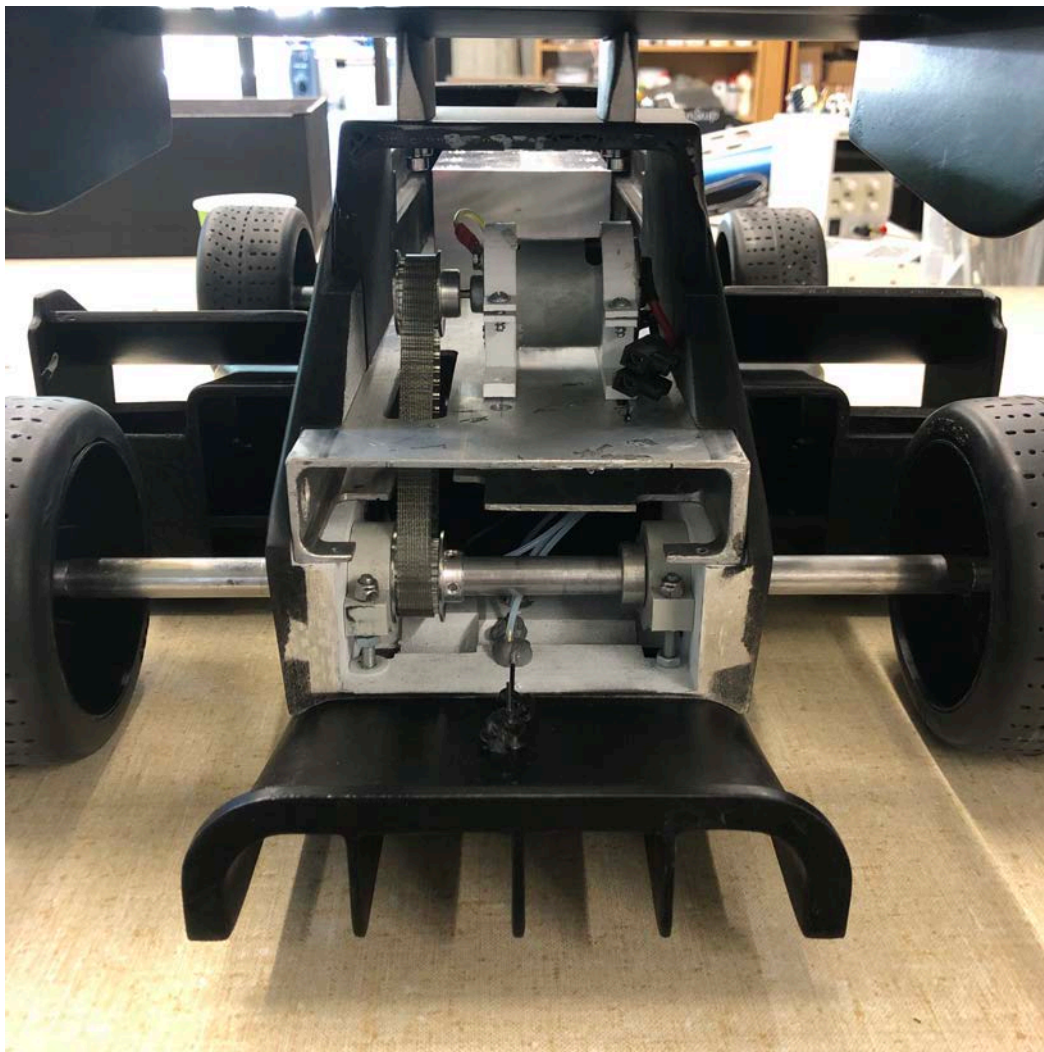


FIGURE 3.2: Wheel drive system used for the wind tunnel model

Upon testing the setup, vibrations began to occur on the model from 1800 revolutions per minute (RPM) upwards. During two studies who investigated the drag difference between stationary and turning bicycle wheels [20]-[21] using both a wind tunnel and CFD at comparable speeds, the standing wheel had a 20% lower drag coefficient than its rotating counterpart. Despite some major differences in the wheel and tyre type (width and surface), the methods are similar and thus these studies were used as references. The following hypothesis was thus formulated: if drag is assumed to increase linearly with increasing angular velocity of a wheel, as suggested by [22], then a rotating wheel will generate more drag than a static wheel, and a wheel rotating faster than another will also generate more drag.

To investigate these effects, wind tunnel tests with stationary and rotating wheels were performed. Figures 3.3 and 3.4 show that the difference mainly impacts drag and not the resulting downforce. The resulting error is depicted in Figure 3.5, which displays a drag increase of up to 10% with rotating wheels, thus confirming the validity of the previously cited studies. With the primary goal to reduce vibrations to a minimum, it was decided to run the wheels at 1500 RPM, which would reduce the error in drag measurement.

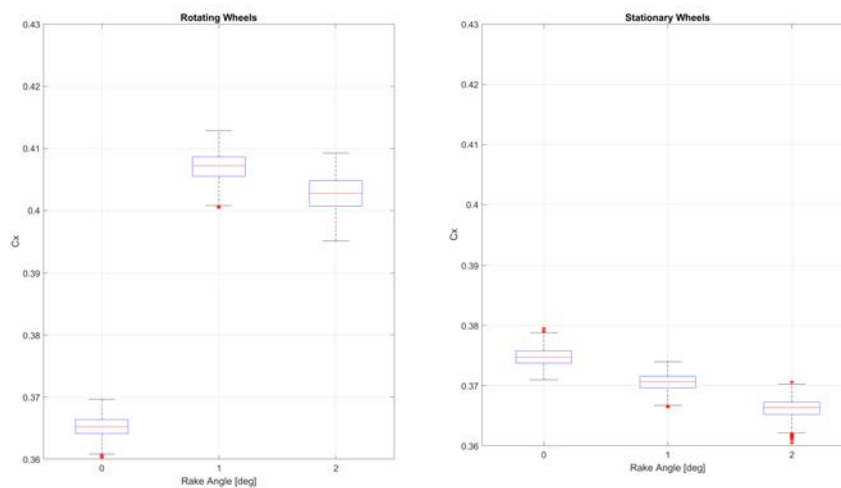


FIGURE 3.3: Effect of rotational versus stationary wheels on drag coefficient



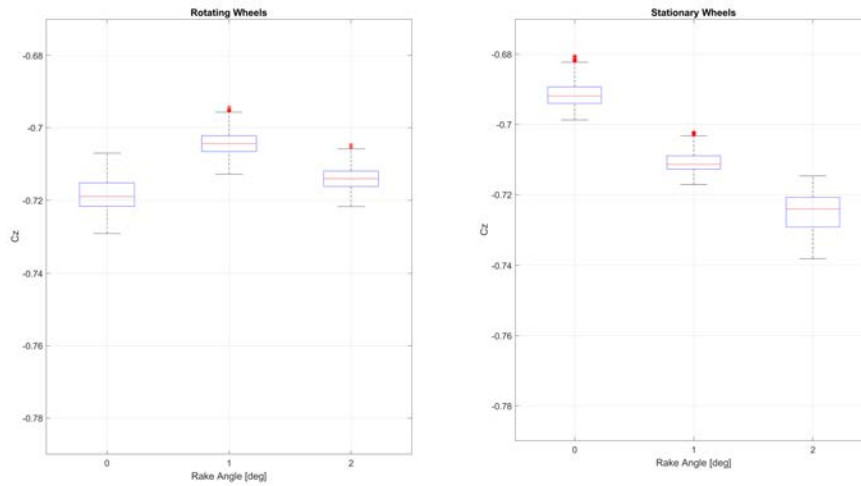


FIGURE 3.4: Effect of rotational versus stationary wheels on downforce coefficient

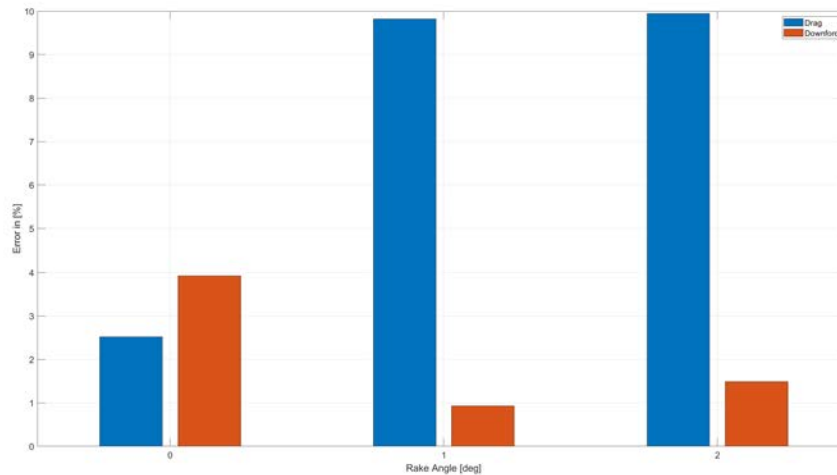


FIGURE 3.5: Resulting error of rotational versus stationary wheels on drag and downforce

### 3.1.3 Model Test Configurations

Additionally, the wind tunnel model should be tested in several configurations, namely with different ride heights (RH), which is the distance between the lowest point of the car underbody and the ground, and rake angles (RA), which corresponds to a forward tilt of the car. For this purpose, the axle holders (see Figure 3.6 below) were used to modify the axle positions was implemented, allowing to control the height of each axle individually. By passing a screw through the holder and placing a nut at the other end, as can be seen in Figure 3.2, the position of the holder could be precisely determined by using the thread of the screw. The required axle positions were directly deducted from the CAD software by using the internal distance calculator.

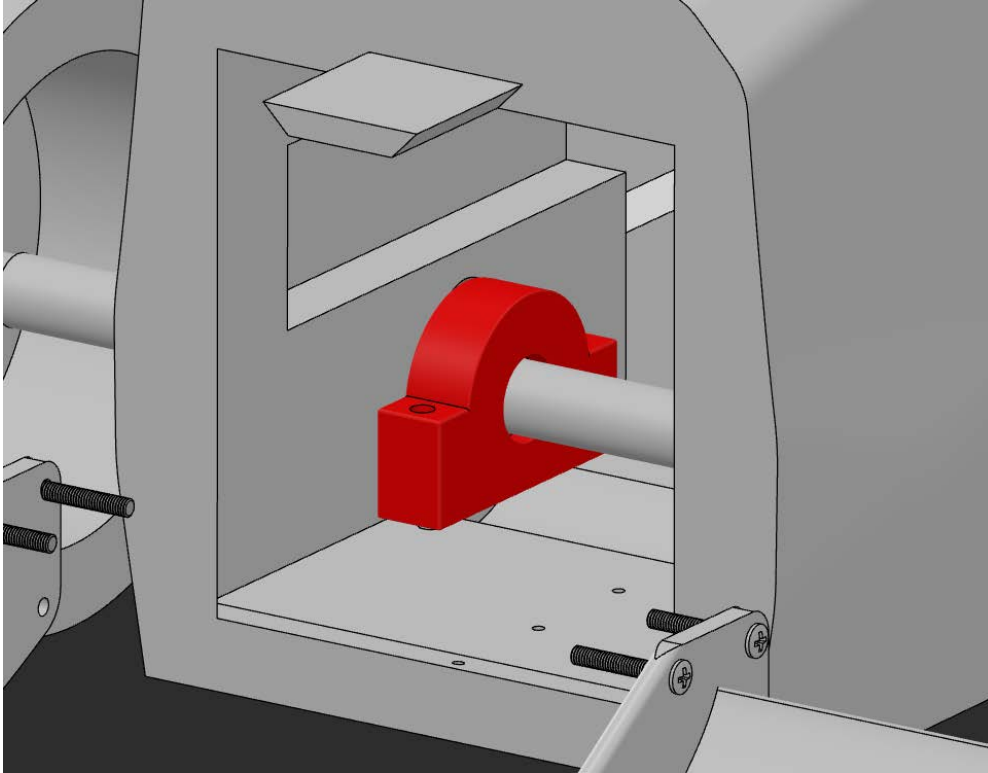


FIGURE 3.6: Axle holder (highlighted in red) used to adjust the axle height

In Table 3.1 below, the initially-planned test configurations are displayed. Since the minimal allowed ride height of the real car is 30 mm according to the regulations [2], 1/4 of this distance is the minimal height allowed for the wind tunnel model (i.e. 7.5 mm). In addition, it was decided to test two other ride heights, namely 10 mm and 12.5 mm (40 mm and 50 mm on the full-scale car, respectively). For the rake angles, an intermediate tilt of 1° and a maximum of 2° were initially chosen.

TABLE 3.1: Initial list of the test configurations with their corresponding ride heights (RH) and rake angles (RA)

Configuration #	Front RH [mm]	Rear RH [mm]	RA [°]
1	7.5	7.5	0
2	10	10	0
3	12.5	12.5	0
4	7.5	14.2	1
5	10	16.7	1
6	12.5	19.2	1
7	7.5	20.9	2
8	10	23.4	2
9	12.5	25.9	2

Keep in mind that the illustrated values for the ride heights are ideal and solely calculated with trigonometry, they do not correspond to the actual height of the axle above the ground since the ride height corresponds to the distance from the lowest

point of the car to the ground. Moreover, for a configuration with no RA, the real front axle height is not the same as the real rear axle height.

After the first tests, it was however decided to add a supplementary RA ( $3^\circ$ ) at 7.5 mm and 12.5 mm front RH for validation purposes. The rake angle was modified by rotating the mount (see Section 3.3.1) and the *RUAG* balance and by adjusting the rear axle to keep the same distance between the wheels and the floor at both axles.

TABLE 3.2: Additional configurations tested to further determine the influence of the rake angle

Configuration #	Front RH [mm]	Rear RH [mm]	RA [°]
10	7.5	27.6	3
11	12.5	32.6	3

### 3.1.4 Manufacturing and Assembly

As said previously, the body parts were first individually 3D printed. Then, sealant was used to cover the slightly rough surface resulting from 3D printing as well as any remaining impurity. Indeed, any rough surface on a 1:4 scale model would result in a four-times-bigger roughness on the real car, which is not acceptable for a study on aerodynamics. After that, the parts were sanded by hand to remove any surplus of sealant and smoothen the skin of the body as much as possible. The parts were then assembled using either pre-fabricated bindings, screws or glue to form the final version of the wind tunnel model, which can be seen in Figure 3.7 below.



FIGURE 3.7: Fully assembled wind tunnel model

## 3.2 Measuring Equipment

### 3.2.1 ALFA Wind Tunnel

The ALFA Laboratory is the low speed wind tunnel of the ZAV used mostly for research purposes. It is a closed circuit wind tunnel with a 1.2m X 0.9m X 0.6m test section in which airspeeds from 5 m/s to 50 m/s can be reached [23]. It can be equipped with various test trolleys or measuring equipment depending on the intended use, in this case a universal test trolley and other measuring devices were used (see Sections 3.2.2 and 3.2.3). It is fitted with sensors that measure and calculate all the relevant wind tunnel parameters (free stream density, free stream velocity, free stream static pressure, ...) and connected to a computer which acquires and records the data. External measuring devices can also be connected to the computer and their data combined with those from the wind tunnel. A sampling rate of 1 kHz was adopted for the data logging.



FIGURE 3.8: ALFA low speed wind tunnel of the ZAV [23]

### 3.2.2 RUAG Balance

The RUAG 6-component block-type balance from the 798 family was used to collect data about the forces acting on the wind tunnel model. Its dimensions are 160mm X 75mm X 50mm, it weighs 3.8 kg and uses strain gauges to calculate the forces and moments [24]. It was attached to the rectangular tube integrated in the body as well as to the mount and calculated both forces and moments in all three dimensions.

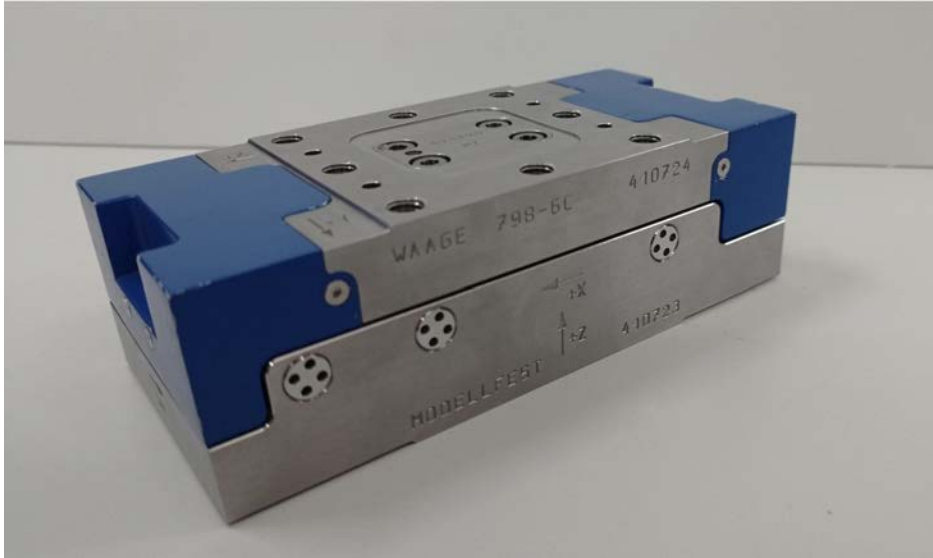


FIGURE 3.9: RUAG 798-C block-type balance

### 3.2.3 *MicroDaq* Pressure Scanner

In addition to the measurement of the forces and moments, the authors also decided to measure the static pressure distribution along the underbody and diffuser of the model. For this purpose, 26 holes were drilled through the lower side of the model and 0.9 mm internal diameter tubes made of brass were glued in each hole and served as static pressure ports. The tubes were then linked to a *MicroDaq* 32 Pressure Scanner (110mm X 45mm X 29mm) [25], which was itself placed in the wind tunnel model (see Figure 3.12). This small device is capable of measuring the gauge pressure (relative pressure) between a reference port and 32 different measurement ports. The use of brass tubes is due to the geometric precision required to conduct an accurate static pressure measurement. Indeed, as explained in the Numerical and Experimental Aerodynamics (NEA) course at the ZHAW School of Engineering [12], "best results are obtained with small, sharp edged holes, perpendicular to a wall parallel to a laminar flow. Hole diameters below 0.5 mm result in slow response times and danger of blockage by dust. Large holes are less accurate because they disturb the flow field more. Main sources of errors are: recirculating flow in the cavity, Mach number effects, stagnation due to orifice geometry and burrs" (see Figure 3.10).

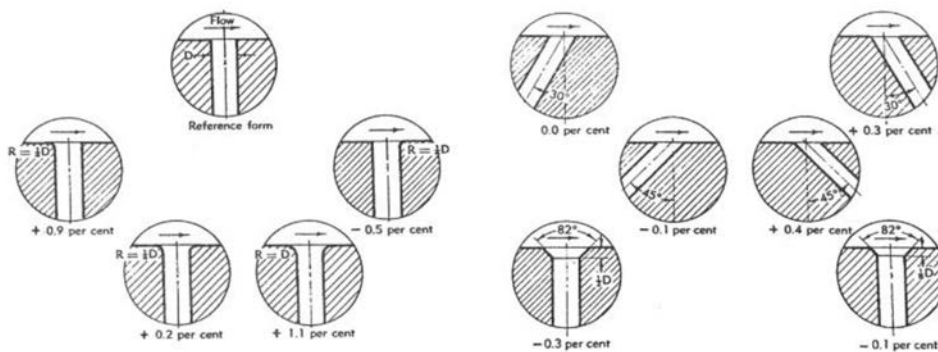


FIGURE 3.10: Static pressure errors depending on the geometry of the orifices [26]





FIGURE 3.11: *MicroDaq* 32 Pressure Scanner

During testing, the reference pressure hose was placed outside of the test section, so as not to be disrupted by the airflow generated by the wind tunnel. The following Figures (3.12 and 3.13) display the static pressure measurement system.



FIGURE 3.12: *MicroDaq* 32 Pressure Scanner connected to plastic hoses spread along the underbody and diffuser



FIGURE 3.13: Static pressure ports on the underbody of the wind tunnel model

From the measured gauge pressures, the coefficient of pressure ( $C_p$ ) was calculated as follows:

$$p_{static} = p_{ref} - p_{gauge_{average}} \quad (3.1)$$

$$C_p = \frac{p_{static} - p_{\infty}}{q} \quad (3.2)$$

Further, to determine the location of the centre of pressure (COP), the following formulas were used.  $M_y$  represents the moments generated by the static pressure and multiplied with the lever arm to the reference point (nose tip, see Table 3.3 below). The centre of pressure is then determined by dividing the sum of all moments by the sum of all static pressures.

$$M_y = p_{static} \times x_{arm} \quad (3.3)$$

$$COP = \frac{\sum M_y}{\sum p_{static}} \quad (3.4)$$

TABLE 3.3: Position of the static pressure ports measured from the tip of the nose of the model

Static Pressure Port #	Distance from Nose Tip [mm]
1	138
2	167
3	176
4	198
5	220
6	242
7	266
8	288
9	306
10	327
11	347
12	367
13	387
14	407
15	427
16	437
17	447
18	457
19	467
20	594
21	614
22	636
23	652
24	682
25	704
26	728

### 3.2.4 Power Supply

In order for the wheels to turn adequately, an adjustable direct current (DC) power supply was used to provide the necessary power to the two motors. The two outputs could each supply up to 3 A and 30 V (up to 90 W) and could be used either in series or in parallel.





FIGURE 3.14: Ningbo FTZ Hopewell power supply, type number PS23023DL

### 3.2.5 GTC TA110 Laser Tachometer

A GTC TA110 Laser Tachometer [27] was used to measure the number of RPM of the wheels by reflecting the beam on a adhesive strip installed on the wheels. The formulas to calculate the angular velocity and therefore the number of RPM are as follows:

$$\omega = \frac{V_{\infty}}{R} \quad (3.5)$$

$$RPM = \frac{60 * \omega}{2\pi} \quad (3.6)$$



FIGURE 3.15: GTC TA110 Laser Tachometer

### 3.2.6 *MATLAB*

*MATLAB* is a programming language and numeric computing platform widely used in many engineering and scientific fields that allows users to plot and analyse data, develop algorithms and create models [28]. The newest version, *MATLAB* R2023a was used for the data processing and visualisation.

### 3.2.7 Tufts

Short red tufts were attached to the model from one end with insulating tape to visualise the airflow around the model. Although very simple, this method is also used in the industry, mainly to visualise local flow fields. The tufts point parallel to the local flow direction in a laminar and attached flow; however, they describe irregular or even chaotic motions in the case of a turbulent boundary layer or separated flow regime [12]. In addition, the use of a thin rod with a tuft attached to the end allowed the flow to be assessed freely in the test section through a small window from the outside, so as not to excessively alter the direction of the airflow.



FIGURE 3.16: Short red tufts attached on the side of the wind tunnel model

### 3.2.8 GoPro Camera

A GoPro HERO8 camera was used to film the flow visualisation process with the tufts because of its capability to film in high definition and in slow motion.



FIGURE 3.17: GoPro HERO8 camera [29]

### 3.3 Test Setup

#### 3.3.1 Test Section Setup

The model was mounted upside-down in the wind tunnel in order to be able to fix the model to the inferior floor of the test section, as can be seen in Figure 3.18 below. The mount is a rectangular metal tube enveloped by a 3D printed NACA0025 symmetrical airfoil. A slot was designed in the airfoil to accommodate the electric cables responsible for powering the sensors and motors so as not to disturb the airflow around the model.

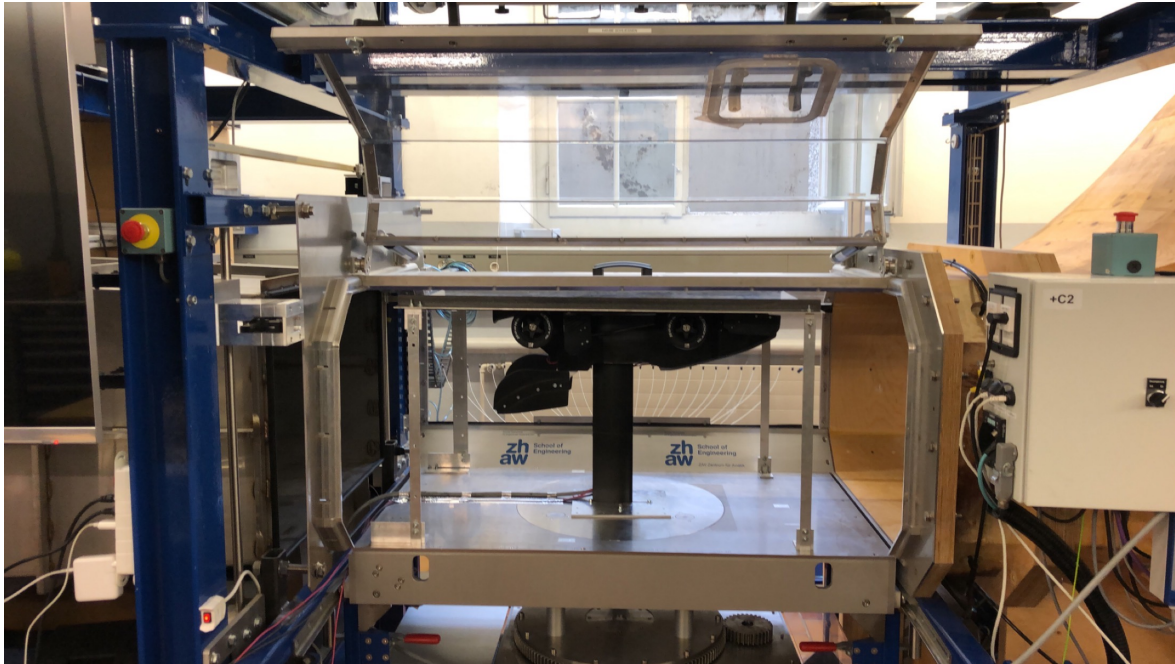


FIGURE 3.18: Model placed in test position in the wind tunnel

Besides, as the ZAV wind tunnel does not offer the possibility to house a rolling floor, a fixed floor with variable height was adopted. Four metal bars, located on each corner of the test section, allowed a precise positioning of the plate with respect to the model, as shown in Figure 3.19 below. Moreover, because of the boundary layer generated by the plate, the displacement thickness was calculated with the help of a *MATLAB* script (see Appendix C.2.1) and the rear height of the plate was lifted by 3 mm. Additional information about boundary layer and displacement thickness are available in Appendix A.5 and A.5.1, respectively.



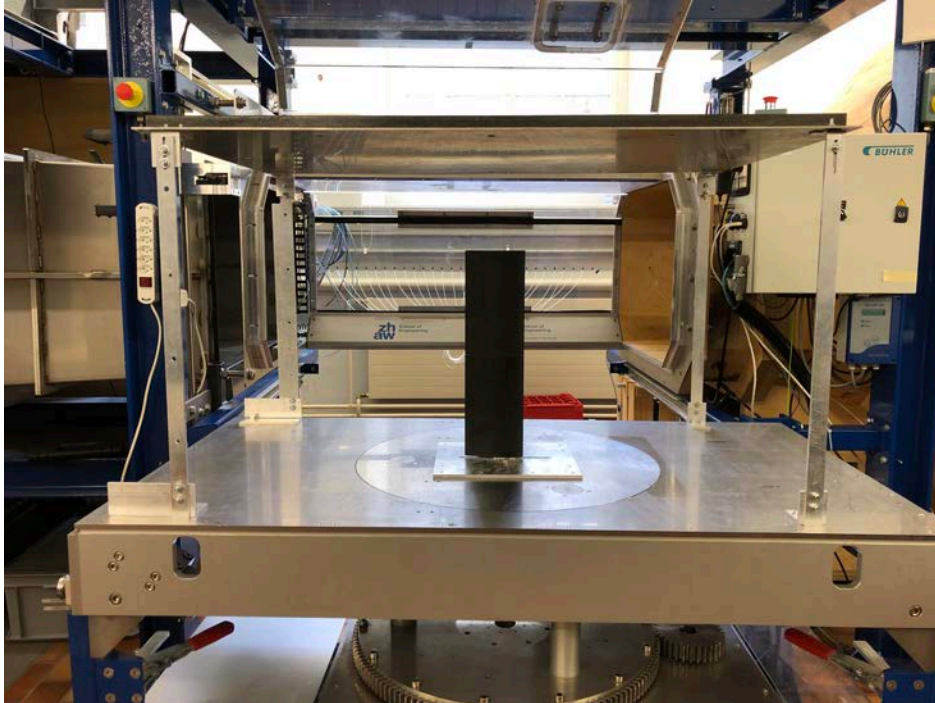


FIGURE 3.19: Wind tunnel setup without the model

### 3.3.2 Flow Similarity

With regard to the two main similarity parameters (see Section 2.2.3) of the wind tunnel model with respect to the full-scale racing car (Reynolds number and Mach number), they are depicted in Equations 3.7 and 3.8 below:

$$Re = \frac{\rho V l}{\mu} \quad (3.7)$$

$$M = \frac{V}{a} \quad (3.8)$$

While the similarity in terms of Mach number is easily achievable since the differences in temperature (proportional to the speed of sound  $a$ ) between the full-scale car and the model are trivial, considering that they operate at the same altitude and therefore at approximately the same temperature, the Reynolds number is more complicated to match. Indeed, the possibilities to alter the parameters specific to  $Re$  are very limited. The only variable that can be freely modified is the velocity  $V$ , but it must still remain within the operational limits of the ZAV wind tunnel (Section 3.8). Hence, the following calculation was done to determine the optimal test speeds. Note the turbulence factor  $TF = 1.4$ , which can be used in low-speed wind tunnel testing [30] (value given by the supervisor of this thesis, Prof. Dr. Leonardo Manfredi).

$$Re_{model} * TF \stackrel{!}{=} Re_{car} \quad (3.9)$$

$$\frac{\rho V_{model} l}{\mu} * TF \stackrel{!}{=} \frac{\rho V_{car} 4l}{\mu} \quad (3.10)$$

Simplifying the equation by removing the density  $\rho$  and the dynamic viscosity  $\mu$  because they are assumed to be constant, this yields:

$$V_{model} = \frac{4}{TF} V_{car} \quad (3.11)$$

The wind tunnel speed is equal to approximately 2.85 times the full-scale race car speed. Therefore, in terms of Reynolds number, the aerodynamic flow while testing the model with 20 m/s is similar to that on the car at only 7 m/s. The authors nevertheless chose test velocities in the order of 20 m/s (see Appendix B.5.2) because higher speeds could break the model, the wings being especially sensitive because of their slimness. In addition, preliminary tests in the wind tunnel in which a speed of 28 m/s was used caused a slight bending of the plate towards the model, which would have affected the validity of the data.

### 3.3.3 Testing Procedure

In addition to the race car model configurations listed in Tables 3.1 and 3.2, several wind velocities were tested. In total, 51 tests were performed, of which a table with the parameters of each tested configuration can be found in Appendix B.5.2. The procedure for each test was the following:

1. Prepare the "CSV" file in which the data will be saved
2. Tare both the *RUAG* balance and the *MicroDaq* pressure scanner
3. Start data recording
4. Accelerate the wheels until stabilised at approximately 1500 RPM
5. Start wind tunnel fan to desired corresponding wind velocity
6. Wait 10 to 15 seconds to allow the devices to measure without any bias
7. Stop wind tunnel fan and model wheels
8. Wait for the wind speed to reach a stable value to stop data recording

### 3.4 Data

#### 3.4.1 Data Filtering

As mentioned in 3.1.2, the rotational speed of the wheels was limited by vibrations. Nevertheless, the data showed oscillations with amplitudes up to +/- 20 Newtons and +/- 0.4 in coefficients. Therefore, all 51 data sets were filtered with the *MATLAB* `lsim` function, which plots the simulated time response of a dynamic system. The used parameters and code can be found in Appendix C.3.2.

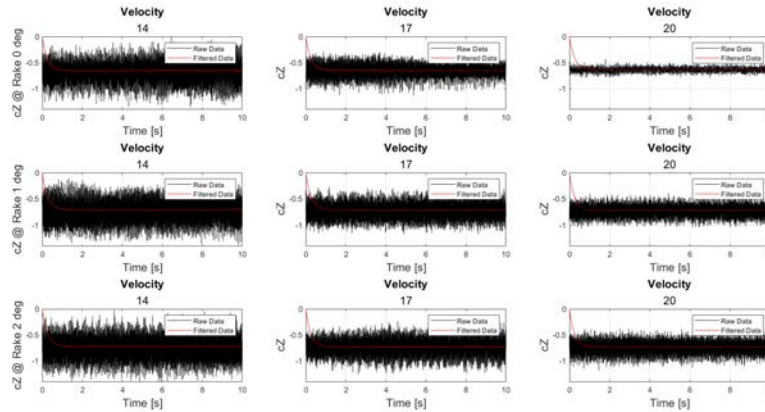


FIGURE 3.20: Filtered and raw data of the downforce coefficient for RH 10.0 mm

Figure 3.20 shows the raw and filtered data, whereas the plots for the two other ride heights can be found in Appendix D. The resulting `lsim` function generates almost no oscillations, which increases the precision of the results. Because the `lsim` function needs around two to three seconds to converge to an acceptable amplitude, the average of raw and filtered data from three to ten seconds of the measurement was calculated. The deviation of these calculations are shown in Figure 3.21 of which a maximum of 0.75% was achieved. Although this deviation is very small, it is an important step to increase the accuracy of the results.

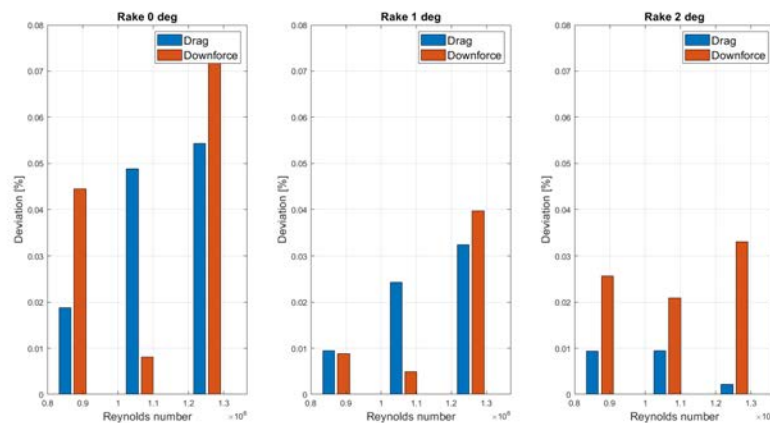


FIGURE 3.21: Deviation between raw and filtered data

### 3.4.2 Repetition Measurement

To make sure that the data gathered is valid and that changes of configurations would not cause any errors, a repetition measurement was conducted. The offset was calculated in percentage and is depicted in Figure 3.22 and shows all the downforce ( $C_z$ ) and drag ( $C_x$ ) measurement errors in percent. Overall, the maximum error over all six measurements, which is depicted in Figure 3.23, was 0.119%.

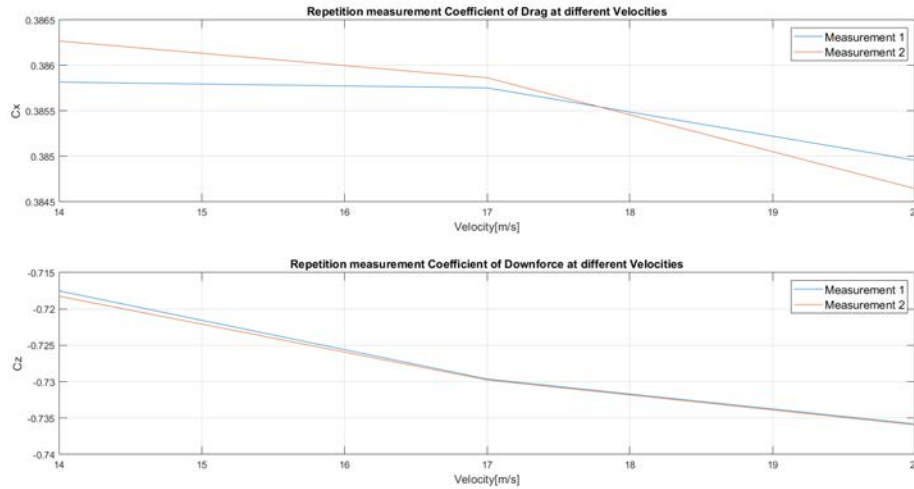


FIGURE 3.22: Line plot of downforce and drag at the three measured velocities with the same setup

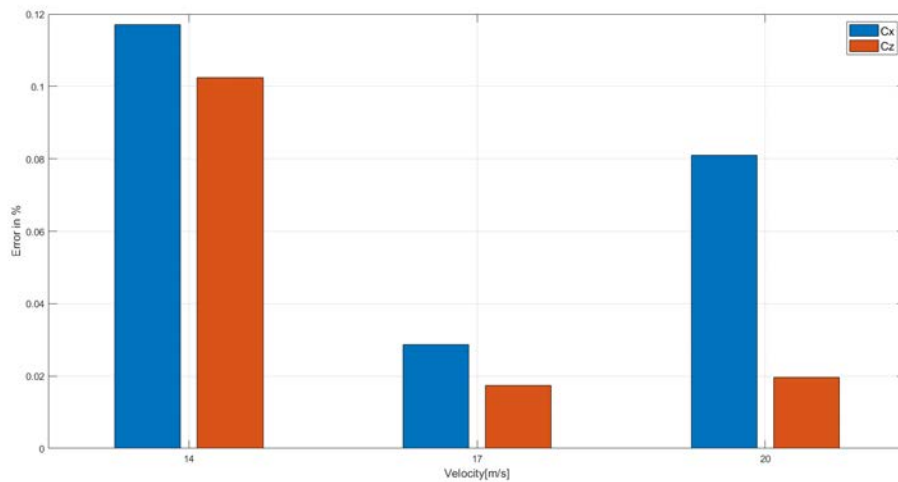


FIGURE 3.23: Resulting error of the repetition measurement in percent

### 3.4.3 Influence of the Reynolds number

As explained in Section 2.2.3, the Reynolds number can change the characteristics of the airflow quite excessively and it is desired to keep it as similar as possible to the real car. Because of the reasons explained, it was decided to test every configuration at three to six different velocities and corresponding Reynolds numbers. Figures 3.24 and 3.25 show the box plots of the measurements at RH 12.5 mm with the filtered



data (the box plots for RH 7.5 mm and 10 mm can be found in Appendix D). The upper and lower quartiles of  $C_z$  and  $C_x$  remain mostly in the same area ( $\pm 3\%$ ) except at the lowest Reynolds number around  $8.9 \times 10^5$ . This trend counts for all measurements except  $C_x$  at  $0^\circ$  RA. Although the results are more thoroughly discussed in Chapter 5, it must be mentioned that it was decided to use the results with the highest Reynolds number to minimise the impact of the Reynolds effect in the overall comparison. This choice is based on the assumption that the results at higher Reynolds numbers better represent the behavior of the real car, as the airflow conditions are more similar.

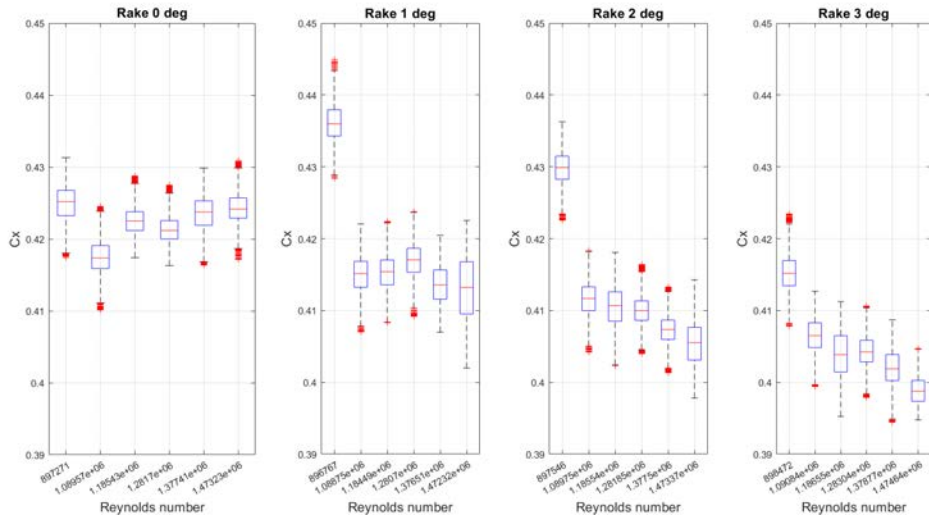


FIGURE 3.24: Boxplot of the filtered drag coefficients at RH 12.5 mm

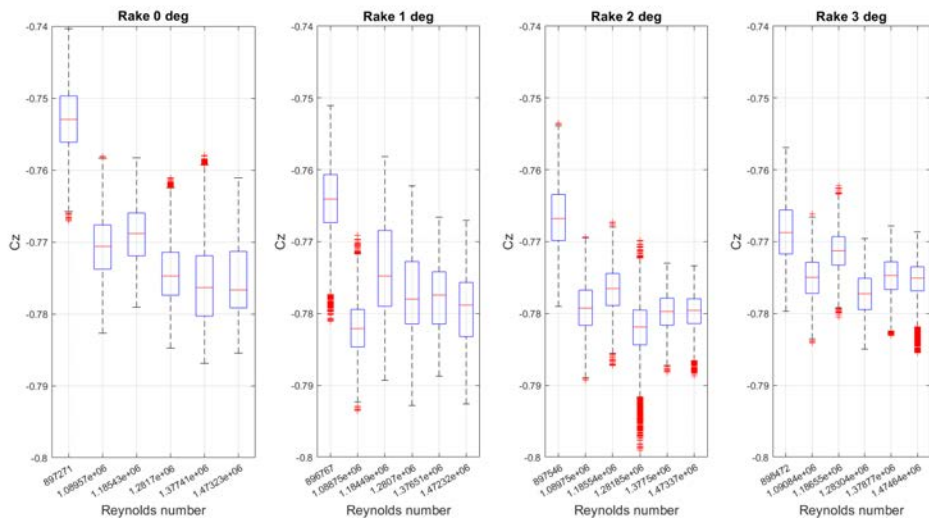


FIGURE 3.25: Boxplot of the filtered downforce coefficients at RH 12.5 mm

Figures 3.26 and 3.27 show the same data sets with the development of the average coefficients. They behave similarly to the medians, where the measurement corresponding to the lowest Reynolds number always shows a large deviation. Furthermore, the order of best to worst performance is even switched at low Reynolds numbers, where drag and downforce at RA  $0^\circ$  have the second best performance.

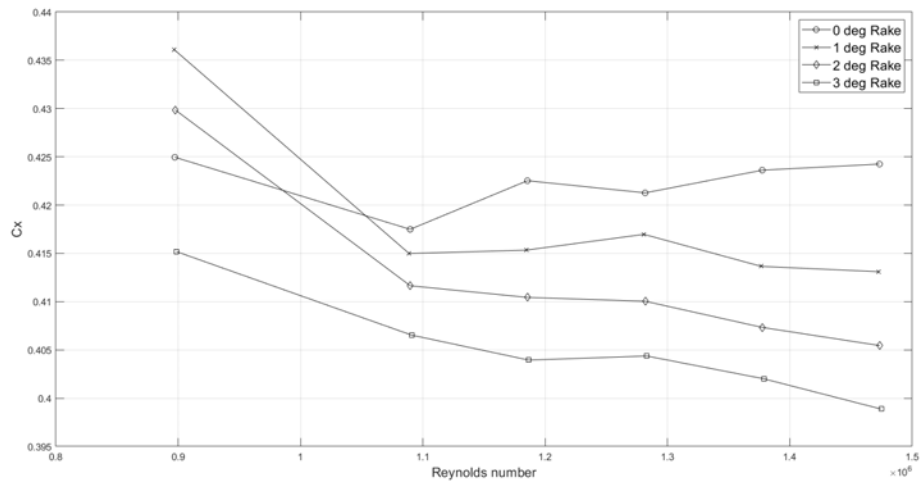


FIGURE 3.26: Development of drag coefficient with Reynolds number at different Rake angles

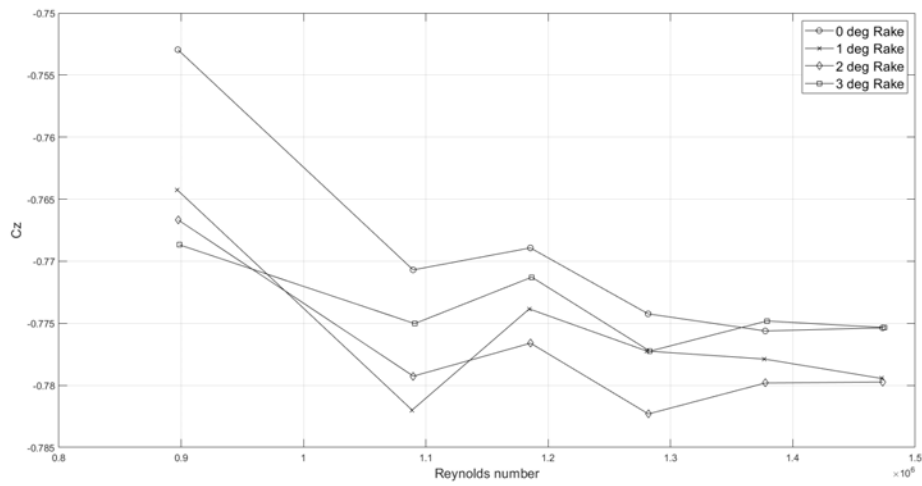


FIGURE 3.27: Development of downforce coefficient with Reynolds number at different Rake angles

## Chapter 4

# Results

### 4.1 Aerodynamic Forces

#### 4.1.1 Downforce and Drag depending on Model Configuration

To fully understand the impact of the setup changes, all results for downforce and drag were plotted together and are represented in this section. Figure 4.1 shows the performance change with increasing rake angle. Overall, it can be seen that the performance declines between 2% and 12% from 7.5 to 10 mm in ride height, although the decline is not constant at every RA. Further, the downforce was maximised at RH 12.5 mm and increased between 2.5% and 19% up to a downforce coefficient of 0.78. The increase of downforce with increasing RA is most noticeable at RH 10 mm and very minor at RH 12.5 mm. Note that at this RH, the performance increase attributed to the RA is very minor.

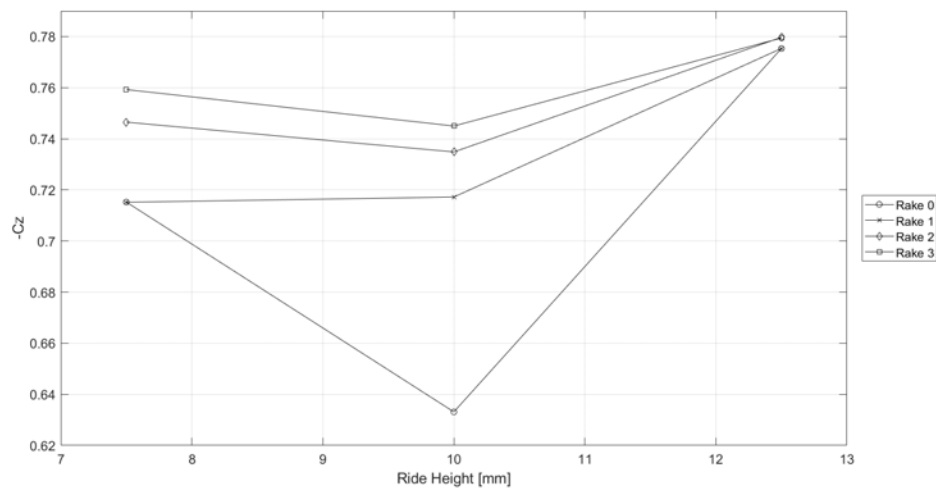


FIGURE 4.1: Line plot of downforce coefficients as a function of the ride height

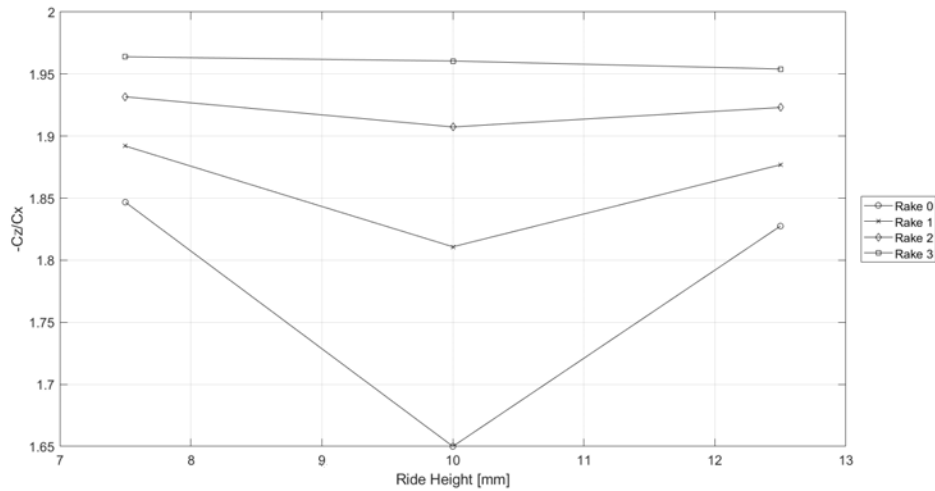


FIGURE 4.2: Line plot of efficiency ( $C_z/C_x$ ) for different rake angles as a function of the RH

Figure 4.2 shows the achieved efficiency ( $C_z/C_x$ ) at all three different ride heights and four different rake angles. The trend with first decreasing and after increasing efficiency only applies for the rake angles  $0^\circ$ ,  $1^\circ$  and  $2^\circ$ , while behaving contrarily for RA  $3^\circ$ . Again, a large drop in downforce and hence, efficiency can be seen for RA  $0^\circ$  at RH 10 mm and again an increase in efficiency from 10 to 12.5 mm. The best efficiency can be achieved at RH 10 mm with RA  $3^\circ$ .

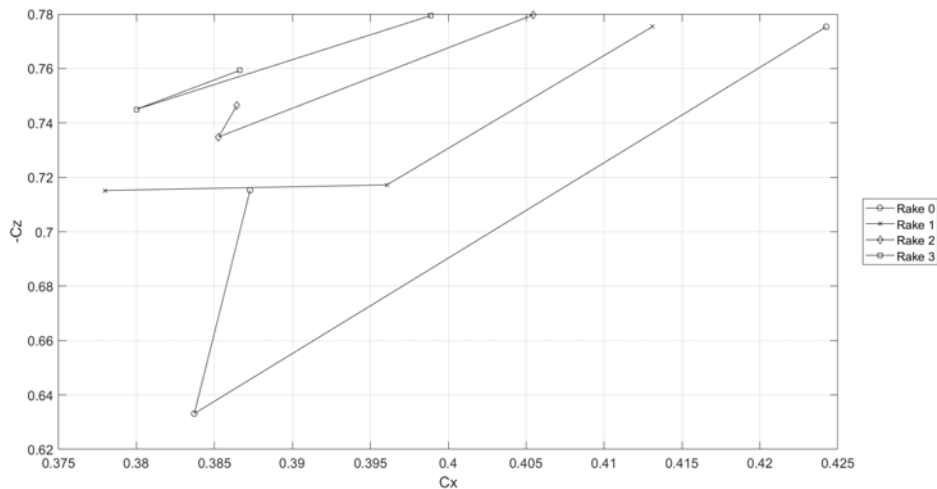


FIGURE 4.3: Line plot of downforce for different rake angles as a function of the drag

The downforce versus drag coefficient is shown in Figure 4.3, in which the best performance can be seen in the top-left corner, where the downforce is maximised and the drag minimised. This correlates with the efficiency shown in Figure 4.2, where the highest efficiency is shown at RA  $3^\circ$ . Similarly as in Figure 4.1, there is no linear correlation between these two parameters, but instead a decrease followed by an increase in performance. The only clear trend can be found with increasing RA, where the downforce coefficient increases with each degree.

### 4.1.2 Contour Plots

The following three contour plots are central to describing the change to overall downforce coefficient and the increase in total downforce if the rear of the car is raised (RA). Further, the aerodynamic balance plot (Figure 4.6) shows that the increase in rear RH or decrease in front RH shifts the downforce distribution towards the rear end.

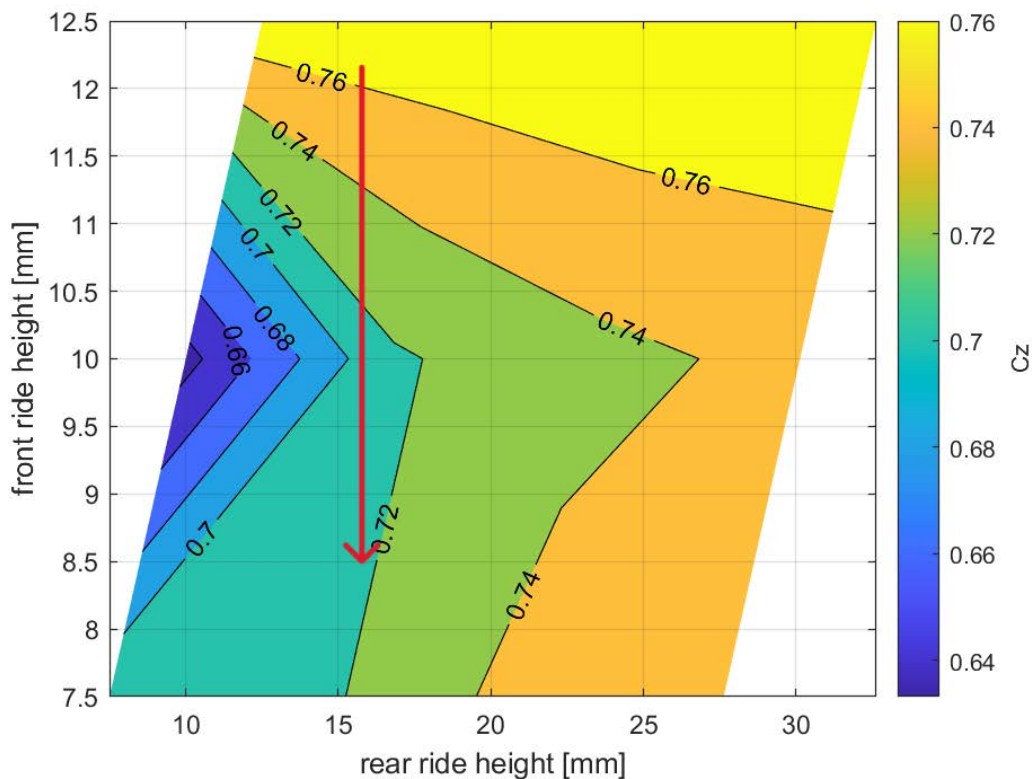


FIGURE 4.4: Influence of RA on total downforce

Figure 4.4 represents the areas with favourable and less favourable ride heights. The downforce in the yellow domain in the top right corner is increased to a coefficient of 0.76 (even up to 0.78 according to Figure 4.1). The contours are cut off on the left side, this denotes the area where the car would have a negative rake angle while the right side indicates that the front wing would touch the floor due to too high rear RH. Similarly as in Figure 4.1, the worst performance is achieved at front RH 10 mm, where the downforce coefficient is as low as 0.64. Furthermore, the highest downforce is achieved at RH 12.5 mm and is less dependent on rear ride height. Thus, the lower the front ride height, the more it is dependent on rear ride height and hence, rake angle (see red arrow in Figure 4.4).

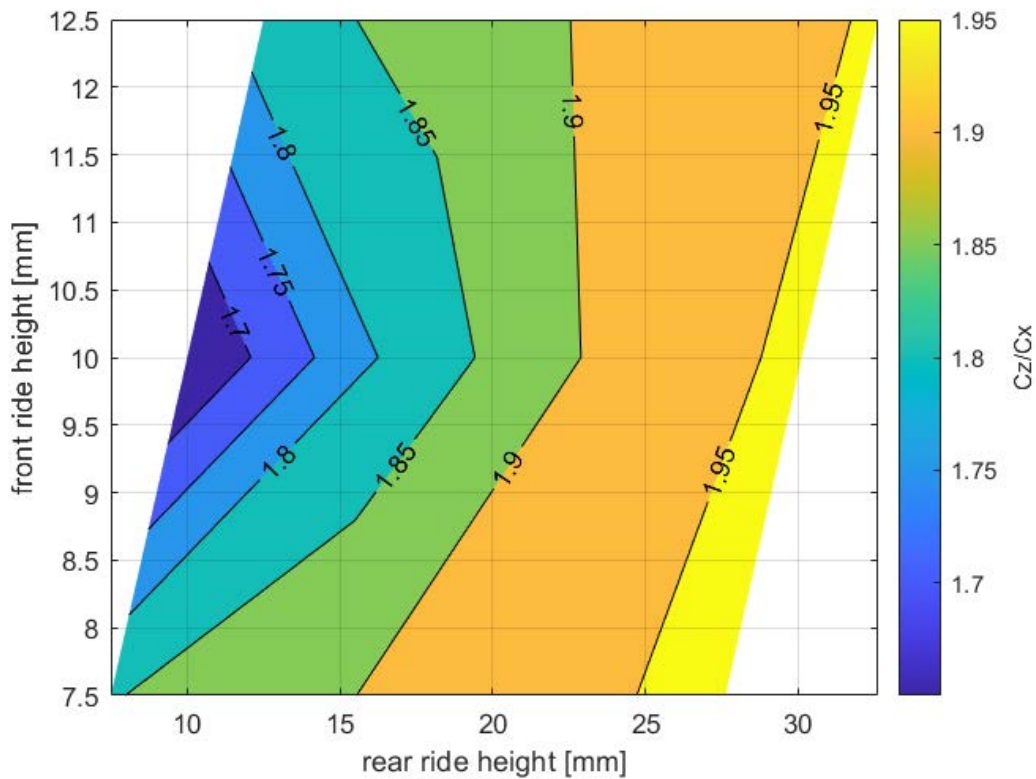


FIGURE 4.5: Line plot of downforce for different rake angles as a function of the drag

The efficiency coefficient is shown in Figure 4.5, in which the better performing configuration is also colored yellow for maximum efficiency, meaning high downforce and low drag. As opposed to the previous figure, that area is positioned on the right side with maximum RA regardless of front RH. Note that the lowest performing area in terms of efficiency corresponds again to 10 mm of front RH.

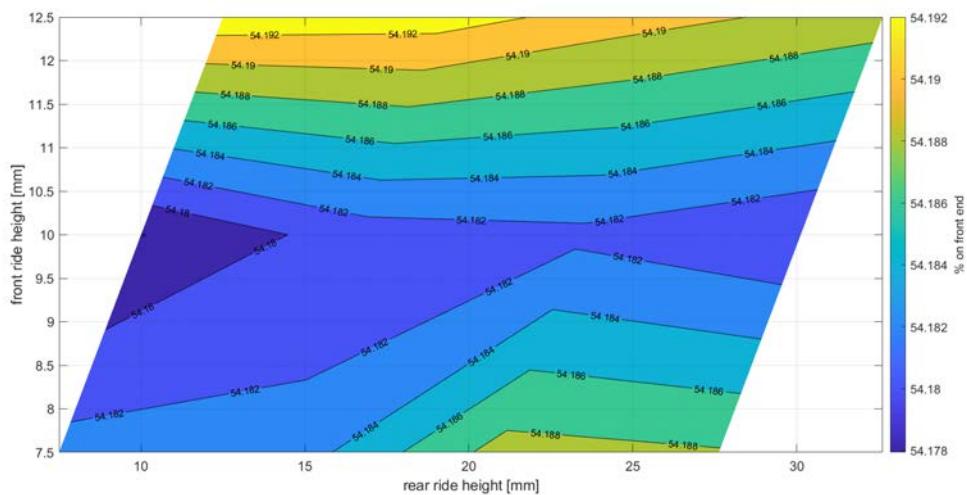


FIGURE 4.6: Influence of RA on front-to-rear aerodynamic balance

At last, Figure 4.6 shows the aerodynamic balance in terms of downforce on the front



axis (front end). The further front the downforce acts, the less under steering can be achieved, which is vital in racing to control the car. For the present car, it can be seen that the aerodynamic balance is limited between 54.178% and 54.192% and can be controlled by setting the front and rear RH.

### 4.1.3 Downforce Distribution

As explained in Section 3.2.3, the static pressure could be calculated from the measurements of the gauge pressure. From the static pressure distribution, the centre of pressure for each configuration was calculated and corresponding force distribution on the front and rear axle. This is displayed in Figure 4.7 and shows that the variation of distribution is very small. The black line represents the location of the calculated centre of pressure according to Section 3.2.3. The comparison shows that the centre of pressure changes with downforce distribution and follows a similar trend.

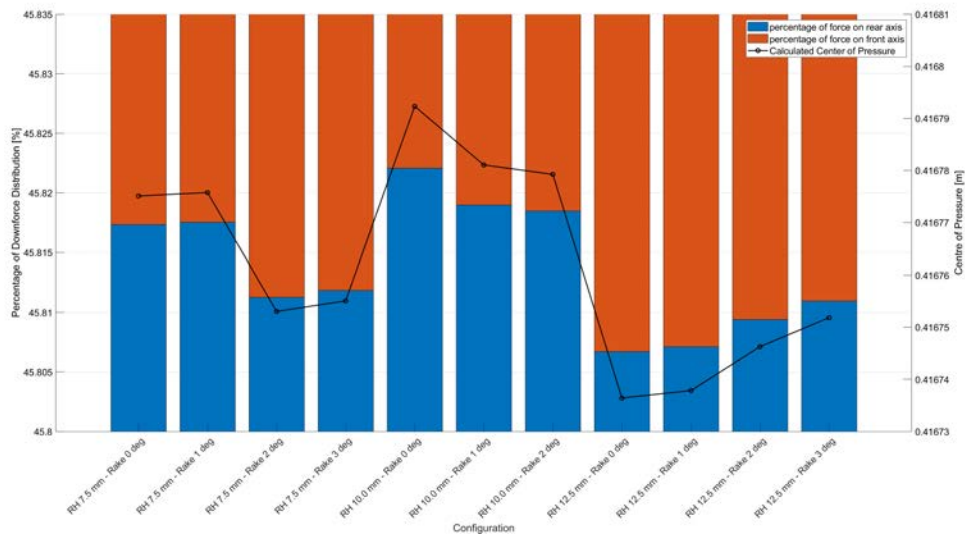


FIGURE 4.7: Force distribution on front and rear axle for all 11 configurations

## 4.2 Pressure Distribution

The gauge pressure was measured along the underbody of the wind tunnel model at 26 defined points (see Section 3.2.3). Two sensors failed and showed measurements with a 100% offset to the other ports, it was therefore decided to exclude these sensors from all calculations. The following three figures display the coefficient of pressure along the underbody, where  $X/c$  represents the position of the sensor relative to the length of the model. The equations used for the coefficient of pressure ( $C_p$ ) calculation can be found in Section 3.2.3 (Equations 3.1 and 3.2), and the corresponding *MATLAB* script can be found in Appendix C.3.6.

For all three rake angles, a similar trend can be observed. The  $C_p$  always rises to almost 0 along the infuser, but decreases rapidly towards the end of the infuser (approximately at 62% of the model length). The  $C_{p_{min}}$  shows no particular tendency at the different rake heights: 7.5, 10 and 12.5 mm yielding -0.84, -0.82 and -1.09, respectively. The position of  $C_{p_{min}}$  at RH 12.5 mm is at approximately 84% of the model length, while it is further forward at RH 7.5 and 10 mm ( $\approx 64\%$ ). Further, it is worth noting that there is no clear trend between the evolution of the  $C_p$  along the underbody and the different rake angles.

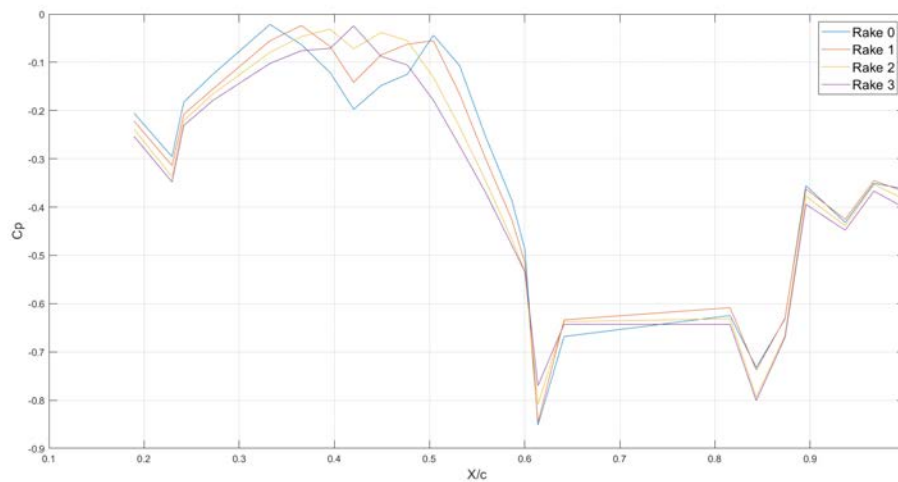


FIGURE 4.8: Coefficient of pressure along the underbody at RH 7.5 mm

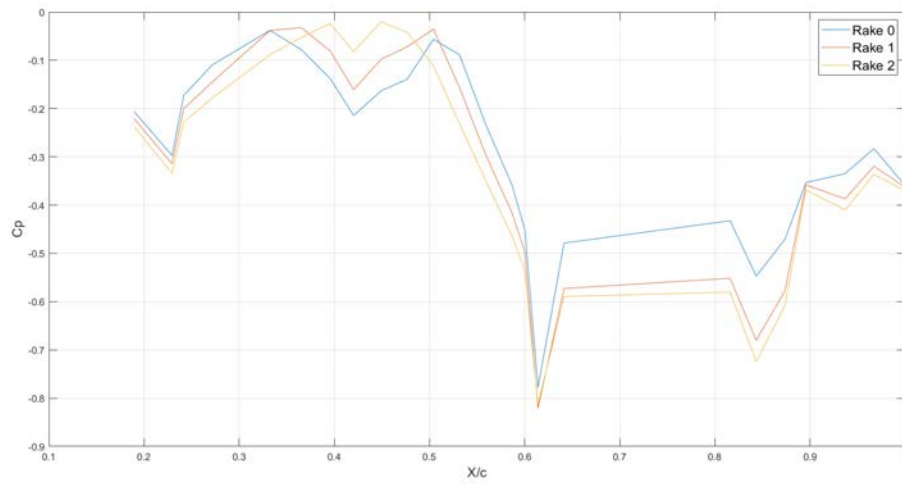


FIGURE 4.9: Coefficient of pressure along the underbody at RH 10 mm

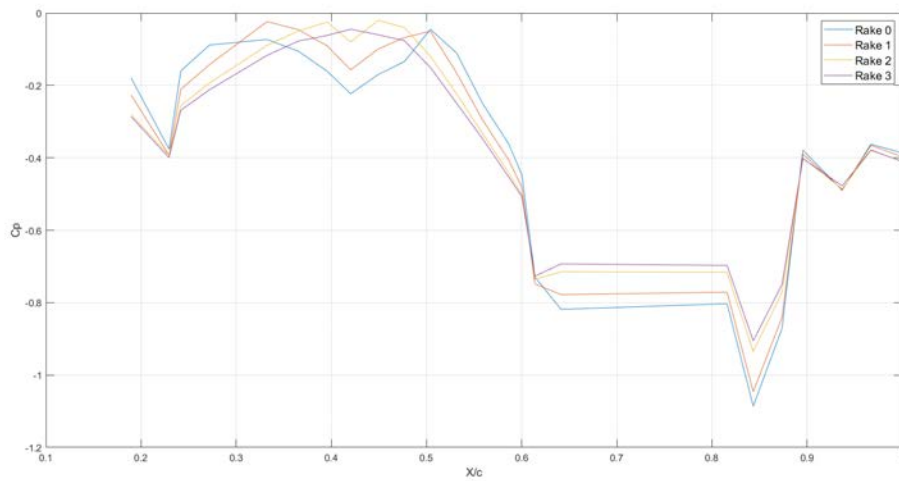


FIGURE 4.10: Coefficient of pressure along the underbody at RH 12.5 mm

### 4.3 CFD Results

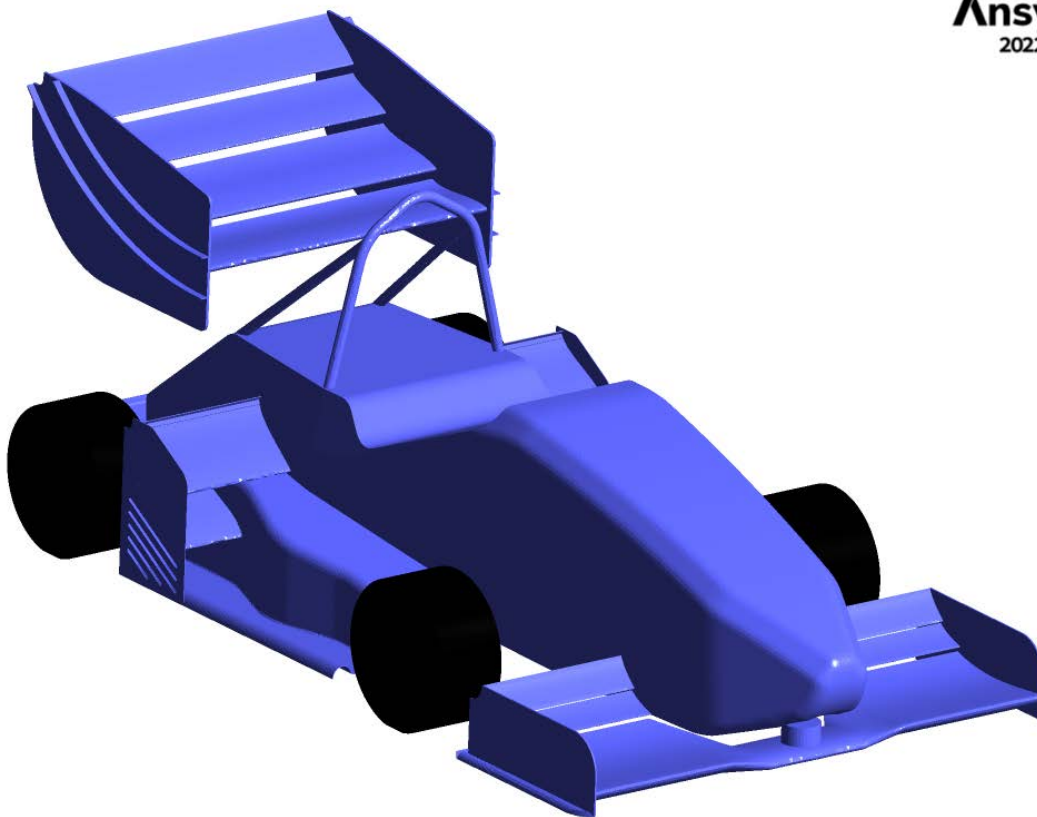
The CFD simulation was performed by Thomas Rüdts, a team member of Zurich UAS Racing, as part of his bachelor's thesis [31], using *Ansys CFX*. The fluid domain settings and the simulation results are presented in Tables 4.1 and 4.2, respectively.

TABLE 4.1: Fluid domain settings used for the CFD simulation

Fluid	Air
Heat Transfer Fluid Temperature	298.15 K (25°C)
Heat Transfer Option	Isothermal
Ambient Pressure	$1 \times 10^5$ Pa
Fluid Free Stream Velocity	$20 \text{ m s}^{-1}$

TABLE 4.2: Results obtained on the scale model by means of CFD

Variable	Value
$C_z$	-0.7
$C_x$	0.27
$F_z$	-37.78 N
$F_x$	16.66 N



**Ansys**  
2022 R2

FIGURE 4.11: 3D scale model used for the CFD simulation

## 4.4 Flow Visualisation

A qualitative analysis of the aerodynamics of the wind tunnel model was also conducted by attaching red tufts to the model to visualise the airflow around it.



FIGURE 4.12: Flow on the side of the model

In Figure 4.12 above, the flow on the side of the wind tunnel model is visualised. It shows the strong wake produced by the rotating front wheel, strongly disrupting the airflow on the sidepod. As for the body of the car, the tufts depict an unsteady motion, probably indicating that the boundary layer has become turbulent, but no apparent flow separation.



FIGURE 4.13: Attached flow in the diffuser

When looking at the diffuser (Figure 4.13), the tufts are steady and show no sign of turbulence or separation.



FIGURE 4.14: Tufts at the leading edge of the plate

With the help of tufts, the state of the flow at the beginning of the plate was confirmed to be laminar, as can be seen in Figure 4.14. To account for the growing boundary layer over the length of the plate (displacement thickness, see Appendix A.5.1) and thus ensure the validity of the results, the rear end of the plate was shifted upwards of 3 mm (see Section 3.3.1).



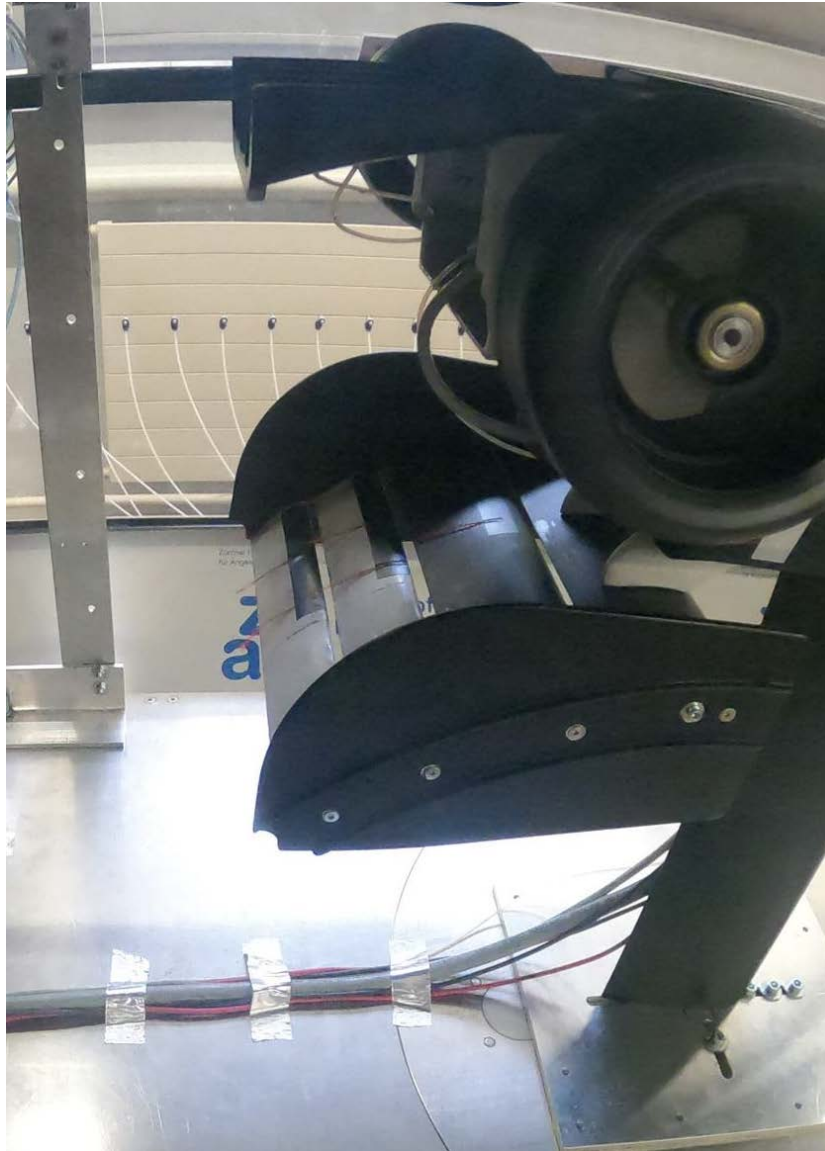


FIGURE 4.15: Airflow on the rear side of the rear wings

In Figure 4.15, there seem to be local flow separations at approximately half the chord of the airfoils due to their incidence with respect to the free airflow. However, the flow at the beginning of each wing is attached, arguably as a result of the energised flow coming from the front side of the rear wing through the gaps between the airfoils.



FIGURE 4.16: Vortex at the end plate of the rear wing

Lastly, a vortex can be observed trailing on the side of the end plate of the rear wing in Figure 4.16. It is generated by the spilling of air from the high pressure zone (above the rear wing) to the lower pressure zone (outside the rear wing). The end plates are there to reduce the magnitude of these vortices, which are harmful to a racing car because they increase drag and reduce downforce.

## Chapter 5

# Discussion and Conclusion

### 5.1 Validity

#### 5.1.1 Wind Tunnel Model

The following factors concerning the 1:4 scale model constructed as part of this project influenced the results obtained during the wind tunnel testing. First, for certain reasons explained in Section 3.1.1, the model was not perfectly geometrically similar to the full-scale racing car, which resulted in a lower aerodynamic similitude. Second, vibrations in the model occurred at high RPM, which forced the implementation of a reduced rotational velocity of the wheels for the wind tunnel testing (see Section 3.1.2), diminishing the fidelity with respect to the real racing car. Third, since the model was hand-processed (see Section 3.1.4), small imperfections remained on the aerodynamic surfaces, increasing surface roughness and decreasing flow laminarity. Moreover, static pressure ports being also installed by hand, a certain measurement error was to be expected (see Figure 3.10). Nevertheless, all of the above factors having minimal influences within tolerances, the results obtained are satisfactory and meet expectations.

#### 5.1.2 Wind Tunnel Testing Setup

In terms of wind tunnel setup, the following elements had a slight impact on the validity of the results. To begin with, the distances between the model and the walls of the wind tunnel test section (see Section 3.8) may be insufficient to conduct an accurate aerodynamics study, because of the possible turbulence of the airflow caused by the relatively large size of the model. Then, the utilisation of a fixed plate to simulate the ground provides rather low flow similitude compared to a moving ground. The plate also tended to lightly bend above a certain speed ( $\approx 25$  m/s), as explained in Section 3.3.1.

#### 5.1.3 Reynolds Effect

As presented in Section 3.4.3, the Reynolds number in the measurements varied greatly with different velocities. Although the calculation of the drag and downforce coefficients should nondimensionalise and therefore eliminate effects of the velocity. But the occurring offset of up to 10% in downforce and drag in Figure 3.25 has shown the need to test with as high velocities as possible. Furthermore, downforce depicted in Figures 3.24 to 3.27 do not develop linearly but rather exponentially

and tend to converge towards higher  $Re$ . Therefore, the higher the Reynolds number, the higher the accuracy of the results. The findings from this study highlight the importance of considering Reynolds effects in wind tunnel testing. While the overall impact on  $C_z$  and  $C_x$  appears relatively minor within the tested range, the significant deviations at low Reynolds numbers emphasise the need for cautious interpretation of results in transitional flow regimes. These results underscore the challenges of replicating real-world aerodynamic conditions accurately in wind tunnels and emphasise the importance of understanding and quantifying Reynolds effects for more reliable aerodynamic predictions.

With the achieved  $Re$  as high as almost  $1.5 \times 10^6$ , the need to satisfy the similarity parameters could not be fully achieved but provides a reference in terms of aerodynamic performance. Further, the largest deviation was found between  $Re = 0.9 \times 10^6$  and  $1.1 \times 10^6$ , which could be eliminated by using the results of the highest  $Re$ .

#### 5.1.4 Comparison with CFD Results

By comparing the results obtained experimentally by wind tunnel testing and by CFD, the following Table (5.1) can be established:

TABLE 5.1: Comparison of the results obtained by wind tunnel testing and CFD

Variable	Wind Tunnel	CFD
$C_z$	-0.77	-0.7
$C_x$	0.42	0.27
$F_z$	-33.55 N	-37.78 N
$F_x$	18.24 N	16.66 N

Note that the wind tunnel results correspond to the RH 12.5 mm and RA 0°, since the 3D model used in the full-scale CFD simulation had 50 mm ground clearance and was not tilted. At first glance, the results are reasonably similar, with the exception of the drag coefficient  $C_x$  being 55% higher in the wind tunnel testing than in the CFD simulation. Discrepancies between the values are probably mainly due to three factors: the difference in geometry between the models, the respective sizes of the control volumes and the influence of the rotating wheels. First, on the wind tunnel model, components present on the 3D model used in CFD such as the sensor (driverless sensor) placed in the centre of the front wing, under the nose, were not reproduced. Furthermore, as explained in Section 3.1.1, some parts of the wind tunnel model were simplified or reinforced for the sake of stiffness and stability which led to a slight geometric difference with respect to the full-scale race car. Second, the CFD simulation was performed using a greater control volume (3.25m X 1m X 1.125m) than the wind tunnel’s test section (1.2m X 0.9m X 0.6m). The airflow in the restrained test section may have been overly disrupted by the presence of the model, which could have resulted in a widely turbulent airflow and thus an increase in drag. Finally, the CFD simulation was realised with the wheels turning at the exact rotational speed corresponding to the free stream velocity (3569.83 RPM at 20 m/s using Equations 3.5 and 3.6), whereas the wind tunnel model’s wheels were limited to approximately 1500 RPM (see Section 3.1.2). This should be responsible for a slight increase in drag, according to the hypothesis formulated in Section 3.1.2.

Unfortunately, it is not possible to assess the validity of said hypothesis. Although there is no way of knowing exactly what the cause of the increase in drag coefficient is in the case of wind tunnel tests, it is reasonable to assume that it is the product of all three factors mentioned previously.

Moreover, the CFD analysis was only used to compare the aerodynamic forces. Due to the presence of a sensor at the entry of the infuser on the 3D model used for CFD, the airflow would not have behaved similarly as on the wind tunnel model and it was thus decided not to compare the pressure distribution along the underbody of the models. As for the flow visualisation, the CFD simulation shows qualitatively similar results to the tuft study performed in the wind tunnel, although it is difficult to visualise the streamlines as accurately experimentally as with CFD. For example, the vortices generated by the rear wing's end plates shown experimentally with a tuft in Figure 4.16 can be found in Figure 5.1 below.

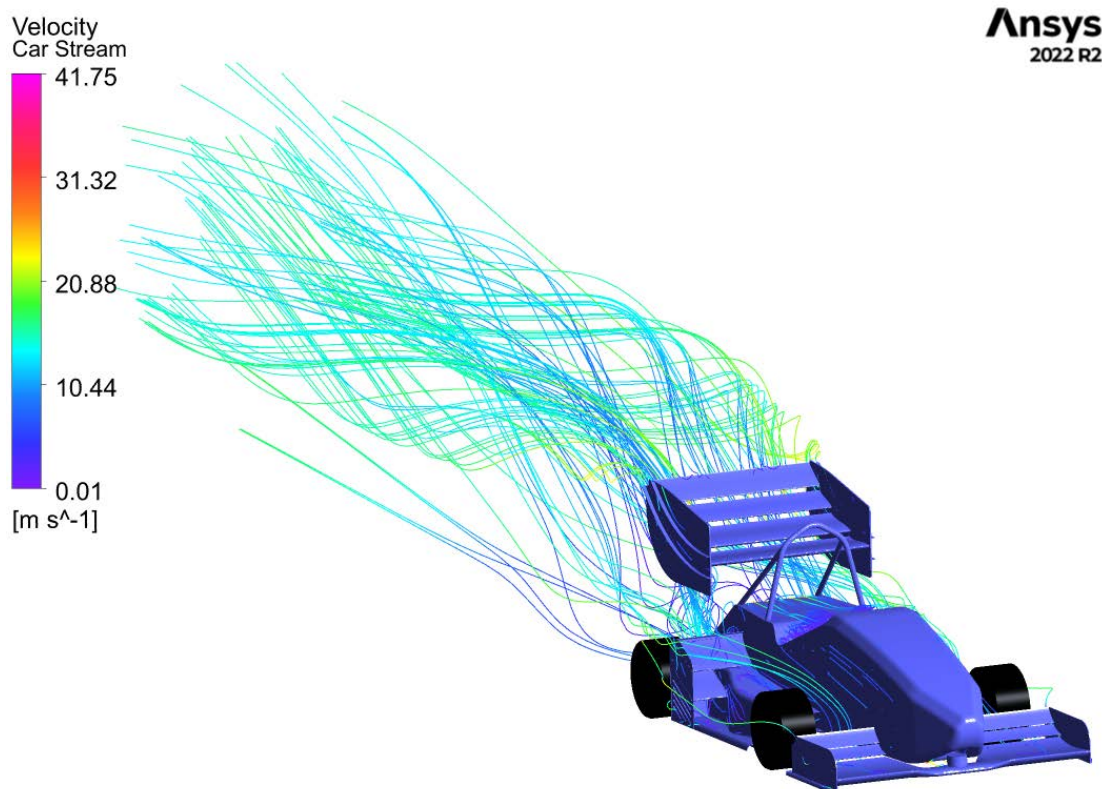


FIGURE 5.1: Streamlines around the scale model



## 5.2 Improvements

### 5.2.1 Model Manufacturing

First, manufacturing the most sensitive parts of the model in stronger materials like metal alloys or carbon fibre would make the model more robust and thus allow higher wind speeds for the wind tunnel tests, which in turns would increase flow similarity 3.3.2. Another possibility to improve the model itself would be to 3D print the delicate parts like wings with resin, since resin structures are less limited by minimum thickness. It must be noted that resin printed parts are stiffer but also much more brittle, this could greatly increase the time invested in constructing and design engineering. Second, simulating the influence of the driver on the aerodynamics by implementing a helmet-shaped structure would enhance the validity of the results by adding a further interest to the research. Third, the choice to use timing belts with pulleys instead of rubber bands reduced the risk of breakage and thus the time spent in configuration changes and repairs. On the other hand, this came with great friction increase in the drive system overall. For future projects with the model it is recommended to use stronger DC-motors, not to be limited by the power required to reach the appropriate rotational velocity of the wheels. Finally, although the adaptability of the ride height settings was very practical, the internal parts were difficult to reach at certain times. It is advisable to cut through the model horizontally to increase efficiency while changing the setup.

### 5.2.2 Test Section Setup

To start with, in order to avoid flow turbulence in the test section that could cause inconsistencies in the results (see Section 5.1.2), building a 1:4.5 or 1:5 scale model could allow the airflow to be less influenced by the relative size of the car model with respect to the test section. Additionally, to improve the floor in the wind tunnel, the plate could be made from another metal like steel to reduce or even rule out bending. Another solution would be to add supports (e.g. 6 metal bars instead of 4) to secure the plate more firmly without disturbing the airflow. Moreover, the influence of the rotating wheels should have been more thoroughly investigated. Since vibrations prevented the wheels to reach the exact angular velocity specific to the free stream wind velocity (see Section 3.1.2), different rotational speeds should have been tested to better understand the evolution of their respective drag component. In addition, a proposal to improve the airflow at the entry of the test section was made by Mr. Marco Giachi, external advisor of this thesis. The idea was to add an adjustable flap at the end of the plate to prevent the model from influencing the upstream flow and causing turbulence. Although a good idea, it was not implemented because the efforts were focused on the wind tunnel model manufacturing. The laminarity of the flow was simply assessed with tufts, as mentioned in Section 4.4 (see Figure 4.14), whereas CFD simulations would make it possible to determine the incidence of the flap producing the least amount of turbulence at the entry of the test section. Lastly, trip wires were not used on the different wings of the model because of the relative complexity of the geometry but would be a way of further studying the effect of the Reynolds number.

### 5.2.3 CFD Simulation

More precise forces and coefficients of drag and downforce could be achieved and a comparison of the pressure distribution along the underbody could be established



between the CFD simulation and the wind tunnel testing if the geometry of the CFD model were more similar to that of the wind tunnel model, in particular with regard to the flow along the underbody (sensor under the nose of the car in Figure 5.1, see Section 5.1.4). Furthermore, the dimensions of the control volume used in the CFD simulation should be identical to the wind tunnel test section's dimensions (see Section 3.8) to obtain results closer to reality.

## 5.3 Conclusion

### 5.3.1 Performance

The three contour plots (Figures 4.4, 4.5 and 4.6) represent the overall performance of the car. As explained in Chapter 2, the ground effect has a large impact on the increase of airflow velocity and hence, pressure reduction. Therefore, as several studies conducted confirm [5]-[32], the downforce is not automatically optimised at minimal RH, but depend on boundary layer expansion and mass flow along the underbody. At too low RH, the boundary layer may expand to the floor beneath it and "choke" the airflow. This might be the effect observed at front RH 7.5 and 10 mm in Figure 4.4. Upon increasing the rear RH, the downforce increases, which supports this hypothesis because the boundary layer could expand freely. Compared to [5], the highest performing setup can be found at minimal front and maximal rear RH, corresponding to the right-bottom area, which contradicts the results of this study. Reasons for that might be that the front wing creates a flow blockage at RA 0° but increases the velocity at higher rake angles and hence, reduce the  $C_p$  below the car.

### 5.3.2 Goals and Research Questions

In conclusion, the objectives of this project (see Appendix B.1) were achieved. In terms of functionality and adaptability of the model, ride height and rake angle could be changed with a newly designed system. The design and manufacturing of the wind tunnel model was successful and eventual wind tunnel test projects in future seasons will be able to build on the progress made in this thesis. Furthermore, all planned test could be performed, including measurements of aerodynamic forces, pressure distribution along the underbody and tuft study. A comparison of experimental testing with CFD simulations could be established (see Section 5.1.4), although, as explained in the previous Section 5.2.3, the configurations should be previously matched for CFD and wind tunnel testing for better comparability.

The research questions mentioned in Section 1.2 were answered as follows:

- What are key considerations when building a wind tunnel model of a racing car, and how can they affect the accuracy and reliability of the test results?

It was shown that the modular design of a wind tunnel model can have positive and negative impacts. On the one hand it increases the adaptability of certain settings (RH and RA) and thus allows a deeper study of the model. On the other hand, it decreases the stability of the model, which can limit the testing possibilities such as velocity.

- How can 3D printing and other advanced manufacturing techniques be used to build a high-fidelity wind tunnel model of a racing car?

As explained in the previous section, 3D printing has both advantages and disadvantages. While it made the manufacturing process of the model very simple, it first needed to be mastered and the various printing settings had to be adjusted correctly. Further, the time-consuming manual processing (see Section 3.1.4) could have been avoided with resin 3D printing.

- What are the potential limitations and trade-offs of building a wind tunnel model of a racing car, and how can they be minimised or mitigated?

Clearly, the advantages of building and testing a 1:4 wind tunnel model are costs and time savings. Trade-offs had to be made in regards to the similarity parameters, because the Reynolds number corresponding to the full-scale car could not be reached (see Section 3.3.2). Also, the effects of the boundary layer had to be mitigated by calculation and compensation of the displacement thickness (see Section 3.3.1). Finally, the size of the model could not be reduced further due to the usage of the RUAG balance, whose dimensions are fixed. This definitely had an impact on the flow around the model, which could have been influenced by the relatively small size of the test section.

- How does adjusting the ride height affect the aerodynamic performance of a racing car in a wind tunnel test?

The study of the model configurations clearly showed that the ride height influences the aerodynamic performance. The most notable fact was the performance decrease at RH 10 mm, while it peaked at 12.5 mm. The reasons behind it are discussed and some hypotheses were formulated but the exact cause remains unclear.

- What is the optimal rake angle for a racing car in a wind tunnel test, and how does it affect the car's aerodynamic performance?

Of the four tested rake angles, the configuration with  $3^\circ$  clearly showed the best performance. While research on that topic [4] suggested that  $2^\circ$  RA is the optimum, this is not the case here and more thorough studies with other RA need to be conducted. Each degree of increase came with an efficiency gain of approximately 2%.

# Bibliography

- [1] *Zurich UAS Racing*. Zurich UAS Racing. URL: <https://zurichuasracing.ch/> (visited on 10/10/2022).
- [2] Formula Student Germany. *Formula Student Rules 2023*. URL: [https://www.formulastudent.de/fileadmin/user\\_upload/all/2023/rules/FS-Rules\\_2023\\_v1.1.pdf](https://www.formulastudent.de/fileadmin/user_upload/all/2023/rules/FS-Rules_2023_v1.1.pdf).
- [3] Romain Seppey and Aaron Sütsch. "Aerodynamic Package of a Formula Student Racing Car". Project Thesis (Unpublished). Winterthur: ZHAW School of Engineering, 2022.
- [4] Joseph Katz. *Race Car Aerodynamics: Designing for Speed*. 2nd ed. Cambridge, Massachusetts: Bentley Publishers, 1995.
- [5] Simon McBeath. *Competition Car Aerodynamics*. 3rd. 2017. ISBN: 978-1-78711-086-1.
- [6] Leonardo Manfriani. "Principles of Flight". Course. Winterthur: ZHAW School of Engineering.
- [7] Gary Anderson. *What 2022-Style Ground Effect looks like*. The Race. Jan. 25, 2022. URL: <https://the-race.com/formula-1/gary-anderson-what-2022-style-f1-ground-effect-looks-like/> (visited on 12/13/2022).
- [8] Jeff Scott. *Nacelle Vortex Generator*. aerospaceweb. Dec. 18, 2005. URL: <http://www.aerospaceweb.org/question/aerodynamics/q0255.shtml> (visited on 12/13/2022).
- [9] Mauro Forghieri and Marco Giachi. *Capire la FORMULA1*. 5th ed. Bologna, Italy: Minerva, June 2022.
- [10] Romain Seppey and Aaron Sütsch. *Gurney Flap for a Formula Student Racing Car - CFD Project in Numerical and Experimental Aerodynamics*. Report (Unpublished). Winterthur: ZHAW School of Engineering, 2023.
- [11] NASA - National Full-Scale Aerodynamics Complex (NFAC). Publisher: Brian Dunbar. URL: <https://www.nasa.gov/centers/ames/multimedia/images/2005/nfac.html> (visited on 06/05/2023).
- [12] Leonardo Manfriani and Xinying Liu. "Numerical and Experimental Aerodynamics". Course. Winterthur: ZHAW School of Engineering.
- [13] *Aerodynamic Force Model*. URL: <https://www.grc.nasa.gov/www/k-12/airplane/tunmodel.html> (visited on 05/19/2023).
- [14] J. Gordon Leishman. "Dynamic Similarity". In: (Jan. 1, 2023). Book Title: Introduction to Aerospace Flight Vehicles Publisher: Embry-Riddle Aeronautical University. DOI: 10.15394/eaglepub.2022.1066.n14. URL: <https://eaglepubs.erau.edu/introductiontoaerospaceflightvehicles/chapter/dynamic-similarity/> (visited on 06/02/2023).
- [15] *Similarity Parameters*. URL: <https://www.grc.nasa.gov/www/k-12/airplane/airsim.html> (visited on 06/01/2023).

- [16] Lawrence Barretto. *How F1's new sliding scale aero testing rules work – and what impact they will have on racing* | Formula 1®. URL: <https://www.formula1.com/en/latest/article.how-f1s-new-sliding-scale-aero-testing-rules-work-and-what-impact-they-will.pn0sG8N4A0cjbNRbdYx8a.html> (visited on 05/23/2023).
- [17] *The Seven Stages of Developing an F1 Car*. Mercedes-AMG PETRONAS F1 Team. URL: <https://www.mercedesamgf1.com/news/the-seven-stages-of-developing-an-f1-car> (visited on 05/23/2023).
- [18] *Dassault Systèmes*. Dassault Systèmes. Apr. 28, 2022. URL: <https://www.3ds.com/> (visited on 05/16/2023).
- [19] Massimiliano Tondi and Nicola Schneider. “Design and Optimization of an Aerodynamic Package for a Formula Student Car”. Bachelor Thesis (Unpublished). Winterthur: ZHAW School of Engineering, 2022.
- [20] S. Karabelas and N.C. Markatos. “Aerodynamics of Fixed and Rotating Spoked Cycling Wheels”. In: *Journal of Fluids Engineering* 134 (Jan. 1, 2012), p. 011102. DOI: [10.1115/1.4005691](https://doi.org/10.1115/1.4005691).
- [21] A. T. Sayers and P. Stanley. “Drag force on rotating racing cycle wheels”. In: *Journal of Wind Engineering and Industrial Aerodynamics* 53.3 (Dec. 1, 1994), pp. 431–440. ISSN: 0167-6105. DOI: [10.1016/0167-6105\(94\)90094-9](https://doi.org/10.1016/0167-6105(94)90094-9). URL: <https://www.sciencedirect.com/science/article/pii/0167610594900949> (visited on 06/08/2023).
- [22] Fabio Malizia, T. van Druenen, and B. Blocken. “Impact of wheel rotation on the aerodynamic drag of a time trial cyclist”. In: *Sports Engineering* 24.1 (Feb. 3, 2021), p. 3. ISSN: 1460-2687. DOI: [10.1007/s12283-021-00341-6](https://doi.org/10.1007/s12283-021-00341-6). URL: <https://doi.org/10.1007/s12283-021-00341-6> (visited on 06/07/2023).
- [23] *ALFA Laboratory*. ZHAW Centre for Aviation ZAV. URL: <https://www.zhaw.ch/en/engineering/institutes-centres/zav/air-vehicle-design-and-technology/aerodynamics/alfa-laboratory/> (visited on 05/26/2023).
- [24] *Strain gauge balances and instrumentation: Precise – stiff – reliable* | RUAG. URL: <https://ruag-ch.picturepark.com/v/0idnPspo/> (visited on 05/26/2023).
- [25] *Leaders in Pressure, Vacuum & Gas Flow Solutions* | Chell Instruments. Sept. 21, 2022. URL: <https://chell.co.uk/> (visited on 05/31/2023).
- [26] Tony Arts et al. “Measurement techniques in fluid dynamics. An introduction, von Karman institute for fluid dynamics”. In: *Rhode-Saint-Genese* (Jan. 1, 2001), pp. 43–274.
- [27] *TA110 Ergonomic Laser Tachometer and Counter*. General Technologies Corp. URL: <https://gtc.ca/blog/ta110-ergonomic-laser-tachometer-and-counter/> (visited on 05/31/2023).
- [28] *MATLAB - MathWorks*. URL: <https://ch.mathworks.com/products/matlab.html> (visited on 05/31/2023).
- [29] *GoPro HERO8 Black - 4K Waterproof Action Camera*. URL: <https://gopro.com/en/ch/shop/cameras/hero8-black/CHDHX-801-master.html> (visited on 06/06/2023).
- [30] Jewel B. Barlow, William H. Rae, and Alan Pope. *LOW-SPEED WIND TUNNEL TESTING*. 3rd. 1999.
- [31] Thomas Rüdts. “Untersuchung der aerodynamischen Gesamtperformance eines Rennboliden”. Bachelor Thesis (Unpublished). Winterthur: ZHAW School of Engineering, 2023.

- [32] Jason Knight et al. "Investigation of vehicle ride height and diffuser ramp angle on downforce and efficiency". In: *Proceedings of the Institution of Mechanical Engineers, Part D: Journal of Automobile Engineering* 233.8 (July 2019), pp. 2139–2145. ISSN: 0954-4070, 2041-2991. DOI: [10.1177/0954407018776767](https://doi.org/10.1177/0954407018776767). URL: <http://journals.sagepub.com/doi/10.1177/0954407018776767> (visited on 06/07/2023).
- [33] Raymond Serway. "Bernoulli's Principle". In: *Physics for Scientists and Engineers* Fourth Edition, Volume 1 (Saunders College Publishing).
- [34] John P. Heller. "An Unmixing Demonstration". In: *American Journal of Physics* 28.4 (Apr. 1, 1960), pp. 348–353. ISSN: 0002-9505. DOI: [10.1119/1.1935802](https://doi.org/10.1119/1.1935802). URL: <https://doi.org/10.1119/1.1935802> (visited on 06/01/2023).
- [35] The Efficient Engineer. *Understanding Laminar and Turbulent Flow*. Sept. 8, 2020. URL: <https://www.youtube.com/watch?v=9A-uUG0WR0w> (visited on 06/01/2023).
- [36] Abtin Ameri. "Improving the Numerical Stability of Higher Order Methods with Applications to Fluid Dynamics". PhD thesis. Dec. 2019. DOI: [10.13140/RG.2.2.25335.78247](https://doi.org/10.13140/RG.2.2.25335.78247).
- [37] Osborne Reynolds | *British engineer and physicist* | *Britannica*. Apr. 14, 2023. URL: <https://www.britannica.com/biography/Osborne-Reynolds> (visited on 06/01/2023).
- [38] Reynolds Number. URL: <https://www.grc.nasa.gov/www/k-12/airplane/reynolds.html> (visited on 06/01/2023).
- [39] Bastian E. Rapp. "Chapter 9 - Fluids". In: *Microfluidics: Modelling, Mechanics and Mathematics*. Ed. by Bastian E. Rapp. Micro and Nano Technologies. Oxford: Elsevier, 2017, pp. 243–263. ISBN: 978-1-4557-3141-1. DOI: <https://doi.org/10.1016/B978-1-4557-3141-1.50009-5>. URL: <https://www.sciencedirect.com/science/article/pii/B9781455731411500095>.
- [40] *Boundary Layer*. Glenn Research Center | NASA. URL: <https://www1.grc.nasa.gov/beginners-guide-to-aeronautics/boundary-layer-3/> (visited on 06/01/2023).
- [41] Giuseppe Fiore et al. "ANALYTICAL VISCOUS FLOW MODEL AND TEST VALIDATION OF A SWIRL INJECTOR FOR ROCKET ENGINE APPLICATION". In: (July 3, 2015).



# List of Figures

1.1	Zurich UAS Racing Formula Student racing car for the 2022/2023 season . . . . .	1
2.1	Main mechanical and aerodynamic forces acting on a racing car, illustration from [4] annotated with vectors and labels for clarity purposes	4
2.2	Difference between a GT race car (left) and a <i>Formula 1</i> race car (right) [5] . . . . .	5
2.3	Turning speed vs turn radius for different downforce coefficients ( $C_z$ ) .	6
2.4	Lotus 79, first racing car to utilise the ground effect on the sidepods in the 1977/1978 <i>Formula 1</i> season [7] . . . . .	7
2.5	Illustration of the effect of vortex generators (VGs) on a wing with increasing angle of attack [8] . . . . .	8
2.6	Main vortex generator types used on wings or other aerodynamic surfaces [4] . . . . .	8
2.7	Theoretical effect of a Gurney flap on the airflow circulation around a wing [4] . . . . .	9
2.8	Actual effect of a Gurney flap on the airflow at the trailing edge of a wing profile, visualised by means of CFD ( <i>Ansys Fluent</i> ) [10] . . . . .	9
2.9	Full-scale F/A-18 fighter aircraft undergoing high angle of attack (AOA) wind tunnel tests at NASA's Ames Research Center [11] . . . . .	11
2.10	F/A-18 wind tunnel scale model with interchangeable parts to reproduce different flight configurations [13] . . . . .	12
2.11	Scale model of a <i>Formula 1</i> car in a wind tunnel with moving belt, courtesy of Mr. Marco Giachi, standing in the picture . . . . .	13
3.1	Final version of the 3D wind tunnel model, designed and assembled on <i>3DEXPERIENCE</i> . . . . .	14
3.2	Wheel drive system used for the wind tunnel model . . . . .	15
3.3	Effect of rotational versus stationary wheels on drag coefficient . . . . .	16
3.4	Effect of rotational versus stationary wheels on downforce coefficient .	17
3.5	Resulting error of rotational versus stationary wheels on drag and downforce . . . . .	17
3.6	Axle holder (highlighted in red) used to adjust the axle height . . . . .	18
3.7	Fully assembled wind tunnel model . . . . .	19
3.8	ALFA low speed wind tunnel of the ZAV [23] . . . . .	20
3.9	<i>RUAG 798-C</i> block-type balance . . . . .	21
3.10	Static pressure errors depending on the geometry of the orifices [26] . .	21
3.11	<i>MicroDaq 32</i> Pressure Scanner . . . . .	22
3.12	<i>MicroDaq 32</i> Pressure Scanner connected to plastic hoses spread along the underbody and diffuser . . . . .	22
3.13	Static pressure ports on the underbody of the wind tunnel model . . .	23
3.14	<i>Ningbo FTZ Hopewell</i> power supply, type number PS23023DL . . . . .	25

3.15	GTC TA110 Laser Tachometer . . . . .	26
3.16	Short red tufts attached on the side of the wind tunnel model . . . . .	27
3.17	GoPro HERO8 camera [29] . . . . .	27
3.18	Model placed in test position in the wind tunnel . . . . .	28
3.19	Wind tunnel setup without the model . . . . .	29
3.20	Filtered and raw data of the downforce coefficient for RH 10.0 mm . . . . .	31
3.21	Deviation between raw and filtered data . . . . .	31
3.22	Line plot of downforce and drag at the three measured velocities with the same setup . . . . .	32
3.23	Resulting error of the repetition measurement in percent . . . . .	32
3.24	Boxplot of the filtered drag coefficients at RH 12.5 mm . . . . .	33
3.25	Boxplot of the filtered downforce coefficients at RH 12.5 mm . . . . .	33
3.26	Development of drag coefficient with reynolds number at different Rake angles . . . . .	34
3.27	Development of downforce coefficient with reynolds number at different Rake angles . . . . .	34
4.1	Line plot of downforce coefficients as a function of the ride height . . . . .	35
4.2	Line plot of efficiency ( $C_z/C_x$ ) for different rake angles as a function of the RH . . . . .	36
4.3	Line plot of downforce for different rake angles as a function of the drag . . . . .	36
4.4	Influence of RA on total downforce . . . . .	37
4.5	Line plot of downforce for different rake angles as a function of the drag . . . . .	38
4.6	Influence of RA on front-to-rear aerodynamic balance . . . . .	38
4.7	Force distribution on front and rear axle for all 11 configurations . . . . .	39
4.8	Coefficient of pressure along the underbody at RH 7.5 mm . . . . .	40
4.9	Coefficient of pressure along the underbody at RH 10 mm . . . . .	41
4.10	Coefficient of pressure along the underbody at RH 12.5 mm . . . . .	41
4.11	3D scale model used for the CFD simulation . . . . .	42
4.12	Flow on the side of the model . . . . .	43
4.13	Attached flow in the diffuser . . . . .	43
4.14	Tufts at the leading edge of the plate . . . . .	44
4.15	Airflow on the rear side of the rear wings . . . . .	45
4.16	Vortex at the end plate of the rear wing . . . . .	46
5.1	Streamlines around the scale model . . . . .	49
A.1	Converging tube annotated with vectors . . . . .	64
A.2	Difference between laminar and turbulent flow going through a pipe [36] . . . . .	67
A.3	Boundary layer concept in the case of laminar and turbulent flow [40] . . . . .	69
A.4	Evolution of the boundary layer along a flat plate . . . . .	70
A.5	Boundary layer displacement thickness [41] . . . . .	70
D.1	Filtered and raw data of the downforce coefficient for RH 7.5mm, RA 0° and 1° . . . . .	97
D.2	Filtered and raw data of the downforce coefficient for RH 7.5mm, RA 2° and 3° . . . . .	97
D.3	Filtered and raw data of the downforce coefficient for RH 12.5mm . . . . .	98
D.4	Deviation between raw and filtered data for RH 7.5 mm, RA 0° and 1° . . . . .	98
D.5	Deviation between raw and filtered data for RH 7.5 mm, RA 2° and 3° . . . . .	99
D.6	Deviation between raw and filtered data for RH 12.5mm . . . . .	99

D.7 Boxplot of the filtered drag coefficients at RH 7.5mm . . . . . 100  
D.8 Boxplot of the filtered downforce coefficients at RH 7.5mm . . . . . 100  
D.9 Boxplot of the filtered drag coefficients at RH 10 mm . . . . . 101  
D.10 Boxplot of the filtered downforce coefficients at RH 10 mm . . . . . 101  
D.11 Line plots of  $F_x$ ,  $F_z$  and  $q$  for RH 7.5 mm . . . . . 102  
D.12 Line plots of  $F_x$ ,  $F_z$  and  $q$  for RH 7.5 mm . . . . . 102  
D.13 Line plots of  $F_x$ ,  $F_z$  and  $q$  for RH 12.5 mm . . . . . 103  
D.14 Line plots of filtered  $F_x$  in the measurement range for RH 7.5 mm . . . 103  
D.15 Line plots of filtered  $F_z$  in the measurement range for RH 7.5 mm . . . 104  
D.16 Line plots of filtered  $F_x$  in the measurement range for RH 10 mm . . . 104  
D.17 Line plots of filtered  $F_z$  in the measurement range for RH 10 mm . . . 105  
D.18 Line plots of filtered  $F_x$  in the measurement range for RH 12.5 mm . . 105  
D.19 Line plots of filtered  $F_z$  in the measurement range for RH 12.5 mm . . 106

# List of Tables

3.1	Initial list of the test configurations with their corresponding ride heights (RH) and rake angles (RA) . . . . .	18
3.2	Additional configurations tested to further determine the influence of the rake angle . . . . .	19
3.3	Position of the static pressure ports measured from the tip of the nose of the model . . . . .	24
4.1	Fluid domain settings used for the CFD simulation . . . . .	42
4.2	Results obtained on the scale model by means of CFD . . . . .	42
5.1	Comparison of the results obtained by wind tunnel testing and CFD . . . . .	48

# List of Abbreviations

<b>FS</b>	<b>Formula Student</b>
<b>ZUR</b>	<b>Zurich UAS Racing</b>
<b>ZHAW</b>	<b>Zürcher Hochschule für Angewandte Wissenschaften</b> <b>Zurich University of Applied Sciences</b>
<b>FSG</b>	<b>Formula Student Germany</b>
<b>ZAV</b>	<b>Zentrum für AViatik</b> <b>Centre for Aviation</b>
<b>CFD</b>	<b>Computational Fluid Dynamics</b>
<b>RH</b>	<b>Ride Height</b>
<b>RA</b>	<b>Rake Angle</b>
<b>AOA</b>	<b>Angle Of Attack</b>
<b>GT</b>	<b>Grand Touring</b>
<b>FIA</b>	<b>Fédération Internationale de l'Automobile</b>
<b>CAD</b>	<b>Computer-Aided Design</b>
<b>RC</b>	<b>Remote-Controlled</b>
<b>RPM</b>	<b>Revolutions Per Minute</b>
<b>DC</b>	<b>Direct Current</b>
<b>NEA</b>	<b>Numerical and Experimental Aerodynamics</b>
<b>ISA</b>	<b>International Standard Atmosphere</b>
<b>BL</b>	<b>Boundary Layer</b>

# Physical Constants

Acceleration of Gravity	$g = 9.806\,65\text{ m s}^{-2}$
Temperature at Sea Level	$T_s = 288.15\text{ K}$
Pressure at Sea Level	$p_s = 101\,325\text{ N m}^{-2}\text{ (Pa)}$
Density at Sea Level	$\rho_s = 1.225\text{ kg m}^{-3}$
Specific Gas Constant (Air)	$R = 287.053\text{ J kg}^{-1}\text{ K}^{-1}$
Ratio of Specific Heats (Air)	$\gamma = 1.4$
Absolute Viscosity at Sea Level	$\mu_s = 1.7894 \times 10^{-5}\text{ kg m}^{-1}\text{ s}^{-1}$



# List of Symbols

$m$	Mass	kg
$F$	Force	N
$g$	Acceleration of Gravity	$\text{m s}^{-2}$
$T$	Temperature	K
$T_\infty$	Free Stream Temperature	K
$p$	Pressure	$\text{N m}^{-2}$ (Pa)
$p_\infty$	Free Stream Static Pressure	$\text{N m}^{-2}$ (Pa)
$q$	Dynamic Pressure	$\text{N m}^{-2}$ (Pa)
$q_\infty$	Free Stream Dynamic Pressure	$\text{N m}^{-2}$ (Pa)
$\rho$	Density	$\text{kg m}^{-3}$
$\rho_\infty$	Free Stream Density	$\text{kg m}^{-3}$
$C_l$	Lift Coefficient	–
$C_z$	Downforce Coefficient	–
$C_x$	Drag Coefficient	–
$C_f$	Friction Coefficient	–
$C_p$	Pressure Coefficient	–
$V$	Velocity	$\text{m s}^{-1}$
$V_\infty$	Free Stream Velocity	$\text{m s}^{-1}$
$S$	Reference Area	$\text{m}^2$
$R$	Radius	m
$Re$	Reynolds Number	–
$l$	Length $l$	m
$\mu$	Dynamic Viscosity	$\text{kg m}^{-1} \text{s}^{-1}$
$M$	Mach Number	–
$a$	Speed of Sound	$\text{m s}^{-1}$
$M_y$	Moment around the y-Axis	Nm
$COP$	Centre of Pressure	m
$x$	Distance in the x-Direction	m
$I$	Electric Current	A
$U$	Electric Potential	$\text{kg m}^2 \text{s}^{-3} \text{A}^{-1}$ (V)
$P$	Power	$\text{kg m}^2 \text{s}^{-3}$ ( $\text{J s}^{-1}$ or W)
$\omega$	Angular Velocity	$\text{rad s}^{-1}$
$RPM$	Revolutions per Minute	$\frac{60}{2\pi} \times \text{rad s}^{-1}$
$TF$	Turbulence Factor	–
$c$	Chord Length	m
$z$	Distance in the z-Direction	m

## Appendix A

# Basic Aerodynamics Knowledge

In the present Appendix, some basic principles of aerodynamics will be explained. The Principles of Flight course [6] was of great use for the writing of this appendix.

### A.1 Continuity Equation

The continuity equation states that the mass flow of a fluid is conserved. The following Figure (A.1) and equations mathematically describe the concept of the continuity equation.

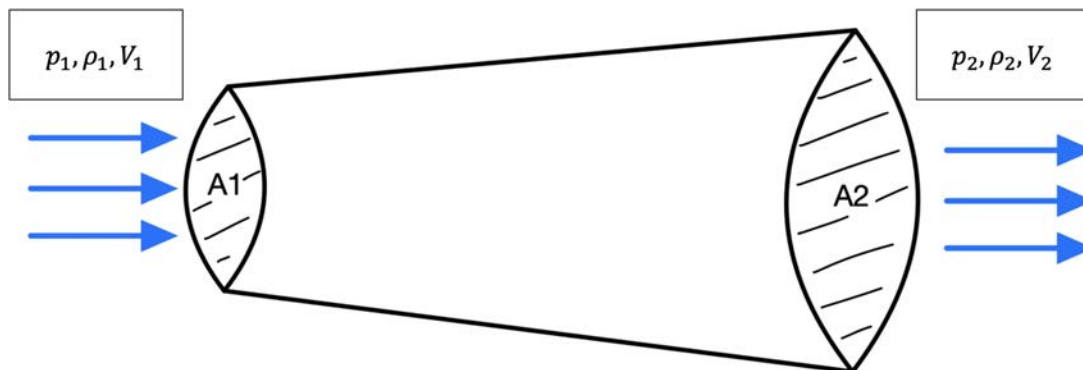


FIGURE A.1: Converging tube annotated with vectors

The mass flow per unit of time  $\dot{m}$  [kg/s] must therefore remain constant from the beginning to the end of the tube, according to the continuity equation. Furthermore,  $\dot{m}$  can be converted into  $\rho VA$ , which yields:

$$\dot{m} = \dot{m}_2 = \text{const.} \quad (\text{A.1})$$

$$\rho_1 V_1 A_1 = \rho_2 V_2 A_2 = \text{const.} \quad (\text{A.2})$$

It is then possible to determine the flow velocity at the outlet of the duct as follows:

$$V_2 = \frac{\rho_1 V_1 A_1}{\rho_2 A_2} \quad (\text{A.3})$$

However, for flows with a relatively low velocity (up to approximately 100 m/s), as is the case of Formula Student racing cars for example, the density can be assumed to remain constant, since the compressibility effects are very small and therefore negligible. The continuity equation (A.2) can then be rewritten in an even simpler form, from which it becomes clear that the velocity depends on the ratio between the initial and final cross-sectional areas:

$$V_1 A_1 = V_2 A_2 \quad (\text{A.4})$$

$$V_2 = V_1 \frac{A_1}{A_2} \quad (\text{A.5})$$

## A.2 Bernoulli Principle

For the application of the Bernoulli principle, an inviscid flow and incompressible must be assumed.

The Bernoulli equation sums the kinetic energy per unit volume  $E_k = \frac{1}{2}\rho V^2$ , potential energy per unit volume  $E_z = \rho g z$  and the energy due to the work of pressure forces  $E_p = p$  along a streamline [33]:

$$\frac{1}{2}\rho V^2 + \rho g z + p = \text{const.} \quad (\text{A.6})$$

In the present case, the potential energy  $E_z$  is assumed to be null because the height  $z$  remains constant along a streamline. The remaining parameters are in fact two variables with similar units: the dynamic pressure  $q = \frac{1}{2}\rho V^2$  and the static pressure  $p$ ; summed, they represent the total pressure  $p_0$  (or stagnation pressure) [6].

$$\frac{1}{2}\rho V^2 + p = p_0 \quad (\text{A.7})$$

From this equality, a variety of formulas can be developed. For instance, in the case of a streamline flowing along a body, with the free stream static pressure  $p_\infty$  (away from the body as not to be influenced by it) and the local static pressure  $p$  at a certain point close to the body, the compressibility effects being negligible, the coefficient of pressure  $C_p$  can be defined as follows [6]:

$$\frac{1}{2}\rho V^2 + p = \frac{1}{2}\rho V_\infty^2 + p_\infty \quad (\text{A.8})$$

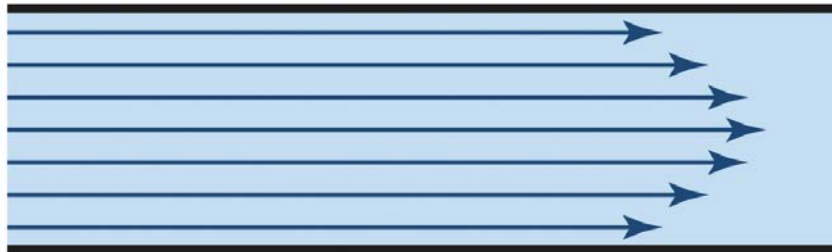
$$p - p_\infty = \frac{1}{2}\rho V_\infty^2 - \frac{1}{2}\rho V^2 \quad (\text{A.9})$$

$$\frac{p - p_\infty}{\frac{1}{2}\rho V_\infty^2} = 1 - \frac{V^2}{V_\infty^2} = C_p \quad (\text{A.10})$$

### A.3 Laminar and Turbulent Flow

In order to understand concepts such as Reynolds number and boundary layer, it is essential to be familiar with the notions of laminar and turbulent flows. A laminar flow, on the one hand, is a flow where infinitesimal fluid layers (laminae) slide over each other without any fluid exchange between layers [6]. The particularity of laminar flows is that they are theoretically "reversible", which means that if the path of each streamline was marked and if a stream flew in one direction, then stopped and went back in time to the starting point  $t_0$ , the lines would be in the same exact place as they were at  $t_0$ , as demonstrated by a famous experiment [34]. On the other hand, turbulent flow is characterized by chaotic motions and contains swirling regions (eddies) resulting in strong mixing of the fluid. Note that most of the phenomena happening in nature tend to be turbulent (e.g. flow of air behind a car on the motorway), and laminar flows (e.g. blood flow in vessels) are seldom [35].

#### Laminar Flow



#### Turbulent Flow

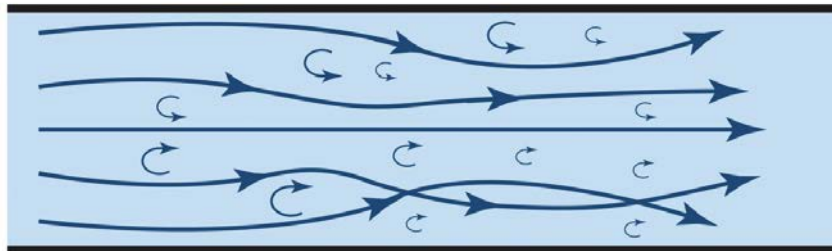


FIGURE A.2: Difference between laminar and turbulent flow going through a pipe [36]

## A.4 Reynolds Number

The Reynolds number, named after its originator Osborne Reynolds (1842-1912) [37], is a non-dimensional parameter which is used to determine whether a flow will be laminar or turbulent.

$$Re = \frac{\rho V l}{\mu} \quad (\text{A.11})$$

The Reynolds number is essentially the ratio between inertial forces and viscous forces in the flow:  $Re = \frac{\text{inertial forces}}{\text{viscous forces}}$  [6][38]. On the one hand, if  $Re$  is small, meaning that the viscous forces are large, the flow is more likely to be laminar because the friction forces due to high viscosity will dampen any initial turbulent disturbance. On the other hand, if  $Re$  is large, which implies that the inertial forces dominate, "an object is able to force its way through a flow field even across the streamlines" [39], characteristic of a turbulent flow. In the case of aeronautics and motorsports, the Reynolds number tends to be large since the velocity (inertia) is considerable and the viscosity of the air is small ( $\mu_s = 1.7894 \times 10^{-5} \text{ kg m}^{-1} \text{ s}^{-1}$ , at sea level under ISA conditions).



## A.5 Boundary Layer

Introduced by Ludwig Prandtl (1875-1953) in the early 1900's, the boundary layer (BL) concept is a revolution in modern aerodynamics. As an object passes through a gas, the gas molecules stick to its surface. This results in the formation of a so-called boundary layer near the body. Prandtl's idea was to divide the flow field into the boundary layer, a limited area around the surface where the viscosity effects are strong and impact the velocity (as shown in Figure A.5 below), and the outside flow where the velocity can be calculated using Bernoulli's principle because the viscosity effects are negligible [6]. Moreover, the velocity exactly on the surface of the body is null, this is called no-slip condition. In addition, the edge of the BL is conventionally defined as the position where the local velocity is 99% of the free stream velocity.

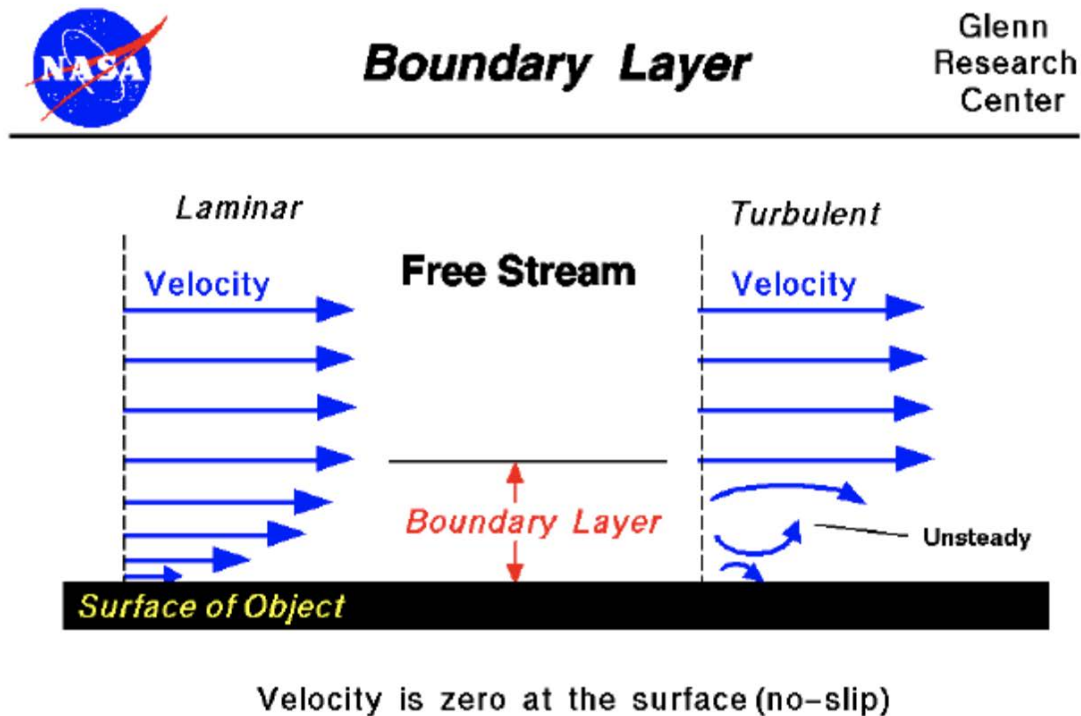


FIGURE A.3: Boundary layer concept in the case of laminar and turbulent flow [40]

Thereafter, the evolution of the boundary layer on a flat plate will be explained. At first the BL is laminar (small  $Re$ ) until it reaches the so-called transition point, at which the length  $l$  is large enough as to increase the Reynolds number above its critical value. The BL then becomes turbulent and continues its path. Depending on some conditions, the boundary layer could eventually detach from the surface, what is called flow separation [6]. The phenomena that lead to the separation are complex and will not be explained in this thesis.

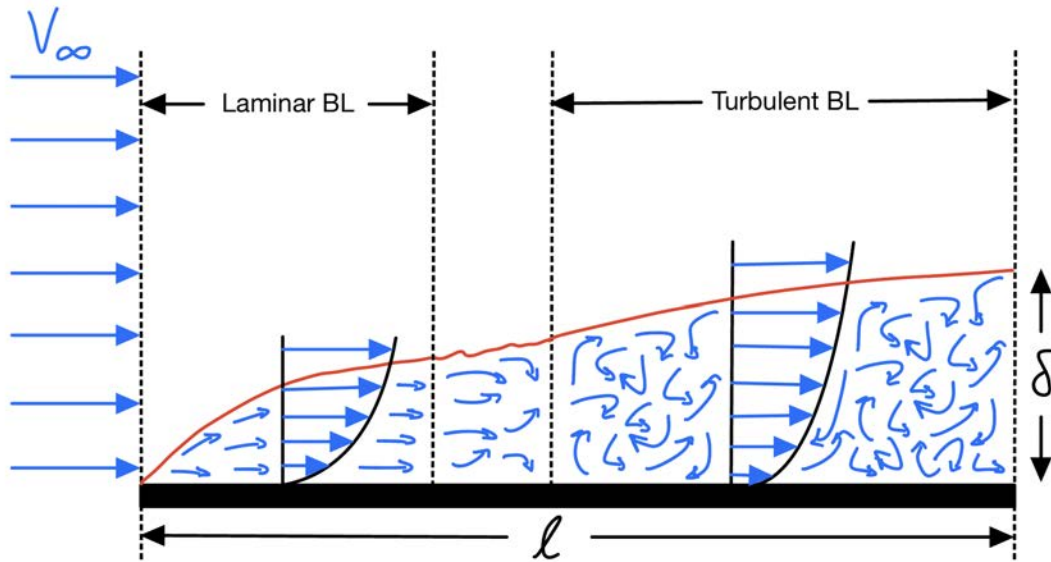


FIGURE A.4: Evolution of the boundary layer along a flat plate

### A.5.1 Displacement Thickness

As seen previously, the viscosity effects in the boundary layer strongly influence the velocity. Thus, it can be deduced that the mass flow ( $\text{kg s}^{-1}$ ) is reduced in the BL. In order to fictitiously maintain the mass flow constant along a body with a BL, the wall is shifted by a length  $\delta^*$ , this value is effectively the thickness that should be added to the wall in order to create a corresponding uniform flow, with uniform velocity equal to that outside the BL and with mass flow equal to that derived by integrating the actual velocity profile, as shown in Figure A.5 [41].

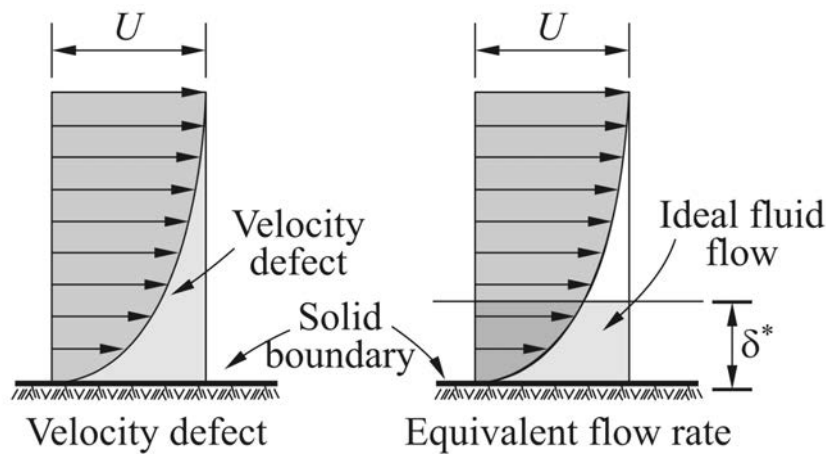


FIGURE A.5: Boundary layer displacement thickness [41]

## Appendix B

# Project Management

### B.1 Project Objectives

BA 2023 : Aerodynamic Package of a Formula Student Racing Car

*Supervisor : Leonardo Manfredi*

*Supervisor assistant : Tobias Zihlmann*

*Students : Aaron Sütsch, Romain Seppey*

Objectives of the BA

Project Milestones

- Manufacturing of the car model for the wind tunnel with the following functions:
  - o Ride height setting
  - o Rake angle setting
- Wind tunnel testing
  - o Downforce / drag
  - o Underbody pressure distribution
  - o Flow separation (Tuft study)
- Comparison with full CFD model of Thomas Rüdli (ZUR Team member) and own project thesis
- Manufacturing of the aerodynamic surfaces
- Writing of the bachelor thesis

Organizational Objectives

- Overall improvements over Project Thesis
- Systematic problem solving and communication between the students and the supervisors
- Realistic project planning and risk management
- Students' motivational and undertaking behavior
- Assistance seeking in case of problems
- Successful cooperation with Zurich UAS Racing

Personal Objectives (Students)

- Successful wind tunnel planning and testing
- Work in a big project environment (Zurich UAS Racing)
- Project management and successful communication with supervisors, ZUR team members, external partners (manufacturers, sponsors, ...)

## B.2 Research Questions

# Research questions Bachelor thesis

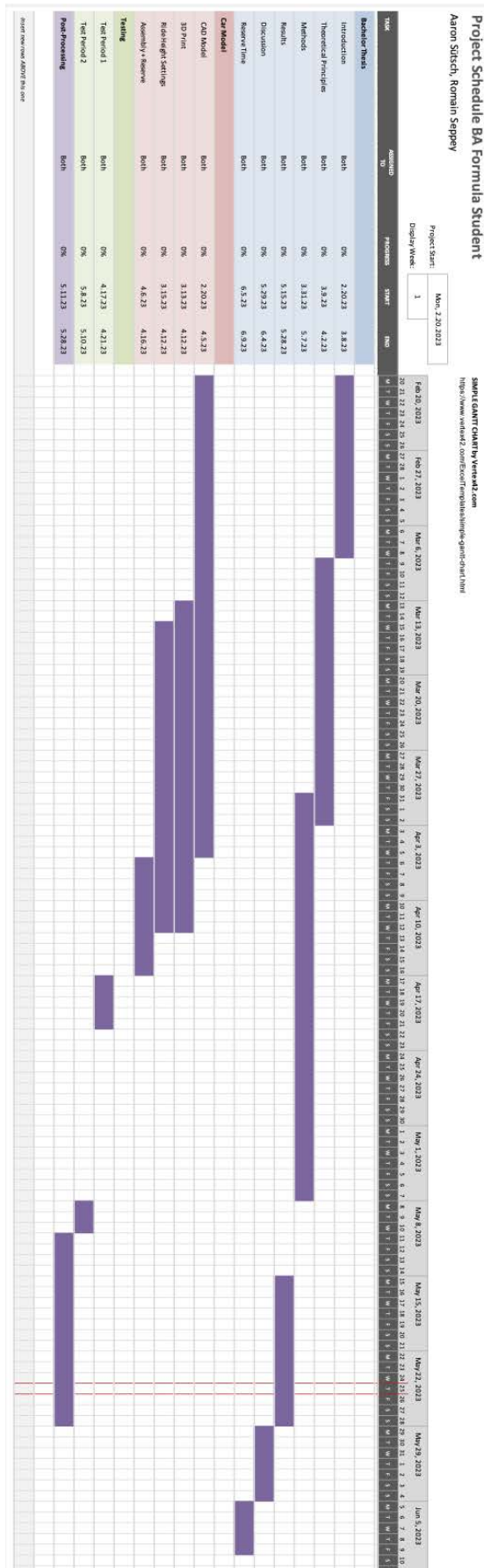
### Modeling

1. What are the key considerations when building a wind tunnel model of a racing car, and how can they affect the accuracy and reliability of the test results?
2. What materials and techniques are best suited for constructing a wind tunnel model of a racing car, and *how can they be optimized for maximum precision?*
3. How can 3D printing and other advanced manufacturing techniques be used to build a high-fidelity wind tunnel model of a racing car?
4. What are the most important components to include in a wind tunnel model of a racing car, and how can they be designed to accurately simulate real-world conditions?
5. How can the accuracy and precision of wind tunnel model testing be validated against CFD simulation data, and what metrics should be used to evaluate the results?
6. What are the potential limitations and trade-offs of building a wind tunnel model of a racing car, and how can they be minimized or mitigated?
7. How can the wind tunnel model of a racing car be modified or adjusted to test specific design changes or performance improvements?

### Performance

1. How does adjusting the ride height affect the aerodynamic performance of a racing car in a wind tunnel test?
2. What is the optimal rake angle for a racing car in a wind tunnel test, and how does it affect the car's aerodynamic performance?
3. How do changes in ride height and rake angle affect the overall aerodynamic balance of a racing car in a wind tunnel test?
4. How can wind tunnel testing be used to improve the overall performance and efficiency of a racing car?

### B.3 Project Gantt Chart



## B.4 Project Risk Matrix

Risk assessment		Severity		
		Low	Medium	High
Probability	High	5	2	1
	Medium	7	4	3
	Low	9	8	6

<b>Risk 1</b>	Prolonged delay in the planning
<b>Cause</b>	Absence of one or more students/difficulty with a step of the planning
<b>Mitigation</b>	Absence sheet, good project management and communication
Classification in the matrix	
Before mitigation :	2
After mitigation :	5

<b>Risk 2</b>	Technical difficulties with a software
<b>Cause</b>	diverse
<b>Mitigation</b>	Seeking help by supervisors/ZUR team members/other organisations
Classification in the matrix	
Before mitigation :	2
After mitigation :	5

<b>Risk 3</b>	Loss of data/document
<b>Cause</b>	Technical problem
<b>Mitigation</b>	Systematic work and regular saves
Classification in the matrix	
Before mitigation :	3
After mitigation :	6



## B.5 Wind Tunnel

### B.5.1 Wind Tunnel Schedule

Wind Tunnel Test Week 1					
	April 17th	April 18th	April 19th	April 20th	April 21st
0800-1000	Setup and calibration	Occupied	Occupied	Testing	Testing
1000-1200	Lunch break			Lunch break	
1200-1300	Lunch break	Occupied	Occupied	Testing	Reserve time
1300-1500	Setup and calibration			Occupied	
1500-1700					
Review Test Week 1 : Due to several problems, only 1 configuration could be tested. Rework of the axles and ride height setting for next testing session.					
Wind Tunnel Test Week 2					
	May 8th	May 9th	May 10th	May 11th	May 12th
0800-1000	Setup and calibration	Testing 2	Testing 4	Occupied	Occupied
1000-1200		Lunch break			
1200-1300				Occupied	Occupied
1300-1500	Testing 1	Testing 3	Testing 5		
1500-1700					



## Appendix C

# MATLAB Scripts

All the *MATLAB* scripts used during this project may be requested by email to: [suetsaar@students.zhaw.ch](mailto:suetsaar@students.zhaw.ch)

## C.1 Wind Tunnel Model

### C.1.1 Axle Height

```
1 %Initial Values
2 %Units: mm
3
4 l_plate = 1000; % length of floor plate
5 l_car   = 650;  % length of car
6 x_f    = 425;  % position of front axle
7 x_r    = 789;  % position of rear axle
8 wb     = 384;  % wheel base
9 r_wheel = 53.5; % radius of the wheel
10 d_t    = 2.9;  % displacement thickness at end of plate
11 rh     = [7.5 10 12.5]; % ride height that wants to be achieved
12 low_fix = 12.5; % distance to lowest point of underbody
13
14 %Initial Calculations
15
16 %Slope of floor plate:  $y = m * x$ 
17 m      = d_t / l_plate; % slope of floor
18 d_yf   = m * x_f
19 d_yr   = m * x_r
20
21 %Reference height
22
23 %Calculations for reference height without rake angle:
24 h_ref_f = r_wheel - rh - d_yf - low_fix
25 h_ref_r = r_wheel - rh - d_yr - low_fix
26
27 %Calculations for reference height with rake angle:
28 alpha   = [0; 1; 2] ; % rake angle
29 h_ref_r_rake = wb .* tand(alpha)
30 h_ref_r_total = h_ref_r - h_ref_r_rake
31
32 %Calculation of rake angle with axle heights:
33 % h_axle_f = 7.5 ;
34 % h_axle_r = 12.5 ;
35 % delta_h_axle = abs(h_axle_r-h_axle_f)
36 % alpha1 = atand(delta_h_axle/wb)
```

## C.1.2 Drive System

```

1 %%Model Drive System
2
3 %Rear:
4 r_dx = 51;
5 r_dy_low = 86.1; %0
6 r_dy_high = 73.1; %2
7 r_dy_medium = (r_dy_low+r_dy_high)/2; %1
8 r_dy = [r_dy_low r_dy_medium r_dy_high];
9
10 %Front:
11 f_dx = 40;
12 f_dy_low = 77.8; %0
13 f_dy_high = 72.8; %2
14 f_dy_medium = (f_dy_low+f_dy_high)/2; %1
15 f_dy = [f_dy_low f_dy_medium f_dy_high];
16
17 %Transmission belt:
18 outer_length_rear = 275;
19 outer_length_front = 250;
20 width_tb = 9.5;
21
22 %Toothed pulley T5:
23 diameter = 23.87;
24 width_tp = 10;
25
26 %Calculation:
27 length_rear = 2 * sqrt(r_dx^2+r_dy.^2) + diameter*pi
28 length_front = 2 * sqrt(f_dx^2+f_dy.^2) + diameter*pi
29 delta_rear = length_rear(1,1)-length_rear(1,3)
30 delta_front = length_front(1,1)-length_front(1,3)

```

## C.2 Setup

### C.2.1 Displacement Thickness

```

1 %% displacement thickness
2 % distance from the flow to the wheels after 1 meter (where the floor
3 % ends)
4 p = 95860; % pressure
5 T = 294.0; % temperature
6 rho = 1.225 * p / 101325 * 288.15 / T;
7
8 V = 17; % velocity in m/s
9 X = 2.8; % length in m
10 u = (0.000001458 * T ^1.5 / (T+110.4)); % viscosity
11 Tf = 1.4; % turbularity windtunnel
12 REocr = 40000; % defined critical RE
13
14 xcr = u * REocr / (rho*V);
15 X = [0:0.001:X];
16
17 REx = (rho*V.*X/u).*Tf;
18
19 Thic_lam = 1.7208./sqrt(REx).*X;
20 xt = [ zeros(1, round(xcr, 3) / 0.001) [0:0.001:(X-round(xcr,3))]];
21
22 %% something
23 Thic_turb = 0.04625 ./ (REx.^0.2).*xt;
24 Thic_bo = Thic_lam + Thic_turb;
25
26 figure(1)
27 plot(X, Thic_bo.*1000); grid on; hold on;
28 xlabel('Length[m]');
29 ylabel('Thickness [mm]');
30 title('Boundary layer development')
31
32 distance1m = Thic_bo(1, 651) % distance of the floor to the ground in m

```

### C.2.2 Mach Number

```

1 %% Environment
2 gamma_a = 1.4;
3 R = 287.053;
4 U = [14 17 18.5 20 21.5 23];
5
6 % ambient conditions
7 T_amb = [288.15:1:303.15];
8 a_amb = sqrt(gamma_a * R .* T_amb);
9
10 for i = 1:16
11     M_amb(i,:) = U ./ a_amb(i); % Mach number for the velocity
12     and temperature range
13 end
14
15 % Wind tunnel conditions
16 T_w = 297;
17 a_w = sqrt(gamma_a * R * T_w);
18 M_w = U ./ a_w;
19
20 %% Plot Mach number vs Temperature
21 figure
22 plot(U, M_amb)

```

## C.3 Data Processing

### C.3.1 Files Reading

```

1 %% read files
2 % read .csv files and save them into tables
3
4 for i = 1:54
5     filename = sprintf('%02d.csv', i);
6     % construct filename with leading zeros
7     [file, path] = uigetfile(filename);
8     % prompt user to select file
9     filepath = fullfile(path, file);
10    % construct full filepath
11    warning('off', 'MATLAB:table:ModifiedAndSavedVarnames')
12    opts = detectImportOptions(filepath, 'NumHeaderLines', 11);
13    opts.VariableNamesLine = 11;
14    opts.VariableUnitsLine = 10;
15    opts.VariableDescriptionsLine = 6;
16    opts.VariableNamingRule = 'modify';
17    variable_name = sprintf('data_%d', i);
18    % construct variable name with dynamic index
19    eval([variable_name, '= readtable(filepath, opts);']);
20    % evaluate and assign table to variable
21    clear opts
22 end
23
24 %% remove unwanted data
25 for j = 1:54 % loop through all 26 tables
26     % construct variable name for current table
27     varname = sprintf('data_%d', j);
28     % retrieve table with dynamic variable name
29     eval(sprintf('%s = %s;', varname, varname));
30     % retrieve variable names for current table
31     var = eval(sprintf('%s.Properties.VariableNames', varname));
32
33     % loop through variables and remove unwanted columns
34     for i = width(eval(varname))-1:1
35         if contains(var(i), ["unscaled", "Tara", "Raw"])
36             eval(sprintf('%s(:, %d) = [];', varname, i));
37             % remove column from table
38         end
39     end
40
41     % create variable name for cleaned table
42     cleaned_varname = sprintf('data_c%d', j);
43     % copy cleaned table to new variable name
44     eval(sprintf('%s = %s;', cleaned_varname, varname));
45
46     % clear variables to avoid polluting workspace
47     clear var i
48 end

```

### C.3.2 Filtering

```

1 %% Initial values
2 clc; clear;
3 load data_RH75.mat
4
5 ref_area = [0.72 0.196];
6 V = [14 17 20];
7

```



```

 8 %% Plot to read out times
 9 figure
10 subplot(311); plot(data_c1.Time, data_c1.scaleTotalFz, data_c1.Time,
    data_c1.scaleTotalFx, data_c1.Time, data_c1.q);grid on; title('
    measurement 01 @14m/s')
11 subplot(312); plot(data_c2.Time, data_c2.scaleTotalFz, data_c2.Time,
    data_c2.scaleTotalFx,data_c2.Time, data_c2.q);grid on; title('
    measurement 01 @17m/s')
12 subplot(313); plot(data_c3.Time, data_c3.scaleTotalFz, data_c3.Time,
    data_c3.scaleTotalFx,data_c3.Time, data_c3.q);grid on; title('
    measurement 01 @20m/s')
13
14 %% start and end times
15 int = 10000;
16 x_starts = [102991; 83468; 109502];
17 x_ends = x_starts + int;
18
19 %% Calculations
20 % Forces
21 Fx = [];
22 for i = 1:3
23     % extract data from the i-th dataset
24     data_i = eval(sprintf('data_c%d', i));
25     Fx(:,0+i) = data_i.scaleTotalFx(x_starts(i):x_ends(i));
26 end
27
28 Fz = [];
29 for i = 1:3
30     % extract data from the i-th dataset
31     data_i = eval(sprintf('data_c%d', i));
32     Fz(:,0+i) = data_i.scaleTotalFz(x_starts(i):x_ends(i));
33 end
34
35 % Dynamic Pressure
36 q = [];
37 for i = 1:3
38     % extract data from the i-th dataset
39     data_i = eval(sprintf('data_c%d', i));
40     q(:,0+i) = data_i.q(x_starts(i):x_ends(i));
41 end
42
43 % Coefficients
44 for i = 1:3
45     cx(:,0+i) = Fx(:,i) ./ (q(:,i) .* ref_area(1));
46     cz(:,0+i) = Fz(:,i) ./ (q(:,i) .* ref_area(2));
47 end
48 %% Lsim Filter
49 TAU = 0.25;
50 flt = tf([1], [TAU, 1]);
51 dt = 1/1000;
52 t = [0:dt:10.0001];
53
54 cxf(:,1) = lsim(flt, cx(:,1), t);
55 czf(:,1) = lsim(flt, cz(:,1), t);
56
57 %% Plot
58 figure
59 plot(t,cz(:,1), 'k-', t,czf(:,1), 'r-');hold on
60 xlabel('Time [s]'); ylabel('cZ')
61 legend('Raw Data', 'Filtered Data'); title('Data Filtering'); grid on
62
63 cz_m = mean(cz(2001:10001,1));
64 czf_m = mean(czf(2001:10001,1));

```

```
65
66 error = abs((cz_m / czf_m - 1) * 100)
```

### C.3.3 Repetition Measurement

```
1 % Initial Values
2 % f = 1000 Hz;
3 clc; clear;
4 load data_RH75.mat; load data_RH100.mat; load data_RH125.mat
5
6 ref_area = [0.196 0.196];
7 V = [14 17 20];
8
9 %% Plot to read out times
10 clc; close all
11 figure
12 subplot(231); plot(data_c25.Time, data_c25.scaleTotalFz, data_c25.Time,
    data_c25.scaleTotalFx, data_c25.Time, data_c25.q);grid on; title('
    measurement 01 @14m/s')
13 subplot(232); plot(data_c26.Time, data_c26.scaleTotalFz, data_c26.Time,
    data_c26.scaleTotalFx, data_c26.Time, data_c26.q);grid on; title('
    measurement 01 @17m/s')
14 subplot(233); plot(data_c27.Time, data_c27.scaleTotalFz, data_c27.Time,
    data_c27.scaleTotalFx, data_c27.Time, data_c27.q);grid on; title('
    measurement 01 @20m/s')
15 subplot(234); plot(data_c52.Time, data_c52.scaleTotalFz, data_c52.Time,
    data_c52.scaleTotalFx, data_c52.Time, data_c52.q);grid on; title('
    measurement 02 @14m/s')
16 subplot(235); plot(data_c53.Time, data_c53.scaleTotalFz, data_c53.Time,
    data_c53.scaleTotalFx, data_c53.Time, data_c53.q);grid on; title('
    measurement 02 @17m/s')
17 subplot(236); plot(data_c54.Time, data_c54.scaleTotalFz, data_c54.Time,
    data_c54.scaleTotalFx, data_c54.Time, data_c54.q);grid on; title('
    measurement 02 @20m/s')
18
19 %% Start & End Times
20 int = 10000;
21 x_starts1 = [88276; 89476; 61133];
22 x_starts2 = [87242; 88275; 59766];
23 x_ends1 = x_starts1 + int;
24 x_ends2 = x_starts2 + int;
25
26 %% Calculations
27
28 Fx1 = [];
29 for i = 25:27
30     % extract data from the i-th dataset
31     data_i = eval(sprintf('data_c%d', i));
32     Fx1(:,0+i-24) = data_i.scaleTotalFx(x_starts1(i-24):x_ends1(i-24))';
33
34 end
35 Fx2 = [];
36 for i = 52:54
37     % extract data from the i-th dataset
38     data_i = eval(sprintf('data_c%d', i));
39     Fx2(:,0+i-51) = data_i.scaleTotalFx(x_starts2(i-51):x_ends2(i-51))';
40
41 end
42
43 Fz1 = [];
44 for i = 25:27
45     % extract data from the i-th dataset
```

```

46     data_i = eval(sprintf('data_c%d', i));
47     Fz1(:,0+i-24) = data_i.scaleTotalFz(x_starts1(i-24):x_ends1(i-24))';
48 end
49 Fz2 = [];
50 for i = 52:54
51     % extract data from the i-th dataset
52     data_i = eval(sprintf('data_c%d', i));
53     Fz2(:,0+i-51) = data_i.scaleTotalFz(x_starts2(i-51):x_ends2(i-51))';
54 end
55
56 % Dynamic Pressure
57 q1 = [];
58 for i = 25:27
59     % extract data from the i-th dataset
60     data_i = eval(sprintf('data_c%d', i));
61     q1(:,0+i-24) = data_i.q(x_starts1(i-24):x_ends1(i-24))';
62 end
63 q2 = [];
64 for i = 52:54
65     % extract data from the i-th dataset
66     data_i = eval(sprintf('data_c%d', i));
67     q2(:,0+i-51) = data_i.q(x_starts2(i-51):x_ends2(i-51))';
68 end
69
70 % Coefficients
71 for i = 25:27
72     cx1(:,0+i-24) = Fx1(:,i-24) ./ (q1(:,i-24) .* ref_area(1));
73     cz1(:,0+i-24) = Fz1(:,i-24) ./ (q1(:,i-24) .* ref_area(2));
74 end
75 for i = 52:54
76     cx2(:,0+i-51) = Fx2(:,i-51) ./ (q2(:,i-51) .* ref_area(1));
77     cz2(:,0+i-51) = Fz2(:,i-51) ./ (q2(:,i-51) .* ref_area(2));
78 end
79
80 % Mean Coefficients
81 cx1_m = mean(cx1);
82 cz1_m = mean(cz1);
83
84 cx2_m = mean(cx2);
85 cz2_m = mean(cz2);
86
87 %% Plots of Forces and Coefficients
88 Time = (0:1/1000:10.0001);
89
90 figure
91 subplot(221); plot(Time, Fx1); xlabel('Time[s]'); ylabel('Fx'); title('
    Measurement 1'); legend('14m/s','17m/s','20m/s')
92 subplot(222); plot(Time, Fx2); xlabel('Time[s]'); ylabel('Fx'); title('
    Measurement 2'); legend('14m/s','17m/s','20m/s')
93 subplot(223); plot(Time, Fz1); xlabel('Time[s]'); ylabel('Fz'); title('
    Measurement 1'); legend('14m/s','17m/s','20m/s')
94 subplot(224); plot(Time, Fz2); xlabel('Time[s]'); ylabel('Fz'); title('
    Measurement 2'); legend('14m/s','17m/s','20m/s')
95
96 figure
97 subplot(221); plot(Time, cx1); xlabel('Time[s]'); ylabel('cx'); title('
    Measurement 1'); legend('14m/s','17m/s','20m/s')
98 subplot(222); plot(Time, cx2); xlabel('Time[s]'); ylabel('cx'); title('
    Measurement 2'); legend('14m/s','17m/s','20m/s')
99 subplot(223); plot(Time, cz1); xlabel('Time[s]'); ylabel('cz'); title('
    Measurement 1'); legend('14m/s','17m/s','20m/s')
100 subplot(224); plot(Time, cz2); xlabel('Time[s]'); ylabel('cz'); title('
    Measurement 2'); legend('14m/s','17m/s','20m/s')

```

```

101
102 %% Mean Coefficients
103 figure
104 subplot(211)
105 plot(V, -cx1_m); hold on
106 plot(V, -cx2_m);
107 legend('Measurement 1', 'Measurement 2','FontSize', 12); title('drag','
    FontSize', 12); xlabel('Velocity[m/s]','FontSize', 12); ylabel('Cx','
    FontSize', 12); title('Repetition measurement Coefficient of Drag at
    different Velocities','FontSize', 12)
108 grid on
109
110 subplot(212)
111 plot(V, cz1_m); hold on
112 plot(V, cz2_m);
113 legend('Measurement 1', 'Measurement 2','FontSize', 12); title('downforce'
    , 'FontSize', 12); xlabel('Velocity[m/s]','FontSize', 12); ylabel('Cz','
    FontSize', 12); title('Repetition measurement Coefficient of Downforce
    at different Velocities','FontSize', 12)
114 grid on
115
116 %% Error
117 load cp_error.mat
118 close all; clc
119 figure
120 cx_error = (cx2_m ./ cx1_m - 1 ) * 100;
121 cz_error = (cz2_m ./ cz1_m - 1 ) * 100;
122 error_tot = zeros(2,3)
123 error_tot(1,:) = cx_error
124 error_tot(2,:) = cz_error
125
126 bar(V, abs(error_tot));
127 xlabel('Velocity[m/s]','FontSize', 12); ylabel('Error in %','FontSize',
    12); legend('Cx','Cz','FontSize', 12); grid on

```

### C.3.4 RH 12.5 mm, all RA

Note that the following script was used for the data processing of the configurations with RH 12.5 mm, similar scripts for the other ride heights are available on request (suetsaar@students.zhaw.ch).

```

1 %% Initial values
2 clc; clear; close all
3 load data_RH125.mat
4 c = 0.742875;
5 ref_area = [0.196 0.196]; % front 0.196 / top 0.72
6 V = [14 17 18.5 20 21.5 23];
7
8 %% Plot to read out times
9 figure
10 data1 = {data_c28, data_c29, data_c30, data_c31, data_c32, data_c33,
    data_c34, data_c35, data_c36, ...
11     data_c37, data_c38, data_c39, data_c40, data_c41, data_c42,
    data_c43, data_c44, data_c45, ...
12     data_c46, data_c47, data_c48, data_c49, data_c50, data_c51};
13
14 speeds1 = {'14m/s', '17m/s', '18.5m/s', '20/s', '21.5m/s', '23m/s', '14m/s
    ', '17m/s', '20m/s', ...
15     '14m/s', '17m/s', '18.5m/s', '20/s', '21.5m/s', '23m/s', '14m/s
    ', '17m/s', '20m/s', ...

```

```

16     '14m/s', '17m/s', '18.5m/s', '20/s', '21.5m/s', '23m/s', '14m/s
    ', '17m/s', '20m/s'};
17
18 for i = 1:24
19     subplot(6,4,i);
20     plot(data1{i}.Time, data1{i}.scaleTotalFz, data1{i}.Time, data1{i}.
    scaleTotalFx, data1{i}.Time, data1{i}.q);
21     grid on;
22     title(['measurement @', speeds1{i}], 'FontSize', 12);
23 end
24
25 %% start and end times
26 int = 10000;
27 x_starts = [58874; 62482; 58153; 56562; 60375; 55856; 61627; 54776; 53456;
    54762; 58576; 49767; 51897; 51318; 51358; 50890; 58201; 56068; 44274;
    57717; 48533; 41047; 41313; 54684];
28 x_ends = x_starts + int;
29
30 %% Calculations
31 % Forces
32 Fx = [];
33 for i = 28:51
34     % extract data from the i-th dataset
35     data_i = eval(sprintf('data_c%d', i));
36     Fx(:,0+i-27) = data_i.scaleTotalFx(x_starts(i-27):x_ends(i-27));
37 end
38
39 Fz = [];
40 for i = 28:51
41     % extract data from the i-th dataset
42     data_i = eval(sprintf('data_c%d', i));
43     Fz(:,0+i-27) = data_i.scaleTotalFz(x_starts(i-27):x_ends(i-27));
44 end
45
46 % Dynamic Pressure
47 q = [];
48 for i = 28:51
49     % extract data from the i-th dataset
50     data_i = eval(sprintf('data_c%d', i));
51     q(:,0+i-27) = data_i.q(x_starts(i-27):x_ends(i-27));
52 end
53
54 % Coefficients
55 for i = 1:24
56     cx(:,0+i) = Fx(:,i) ./ (q(:,i) .* ref_area(1));
57     cz(:,0+i) = Fz(:,i) ./ (q(:,i) .* ref_area(2));
58 end
59
60 % Re_numbers
61 turb_factor = 1.4;
62 u = zeros(10001,9);
63
64 for i = 28:51
65     data_i = eval(sprintf('data_c%d', i))
66     u(:,0+i-27) = (0.000001458 * data_i.Tinf(x_starts(i-27):x_ends(i-27))
    .^1.5 ./ (data_i.Tinf(x_starts(i-27):x_ends(i-27))+110.4)); %
    viscosity with sutherlands constants
67 end
68
69 RE = zeros(1,24);
70 V = [14,17,18.5,20,21.5,23,14,17,18.5,20,21.5,23,14,17,18.5,20,21.5,23,...
71 14,17,18.5,20,21.5,23]
72

```

```

73 for i = 28:51
74     data_i = eval(sprintf('data_c%d',i))
75     RE(i-27) = mean(data_i.rho) * V(i-27) * c / mean(u(i-27)) .*
        turb_factor;
76 end
77 %% Lsim Filter
78 TAU = 0.25;
79 flt = tf([1], [TAU, 1]);
80 dt = 1/1000;
81 t = [0:dt:10.0001];
82
83 % Forces
84 for i = 1:24
85     Fxf(:,i) = lsim(flt, Fx(:,i), t);
86     Fzf(:,i) = lsim(flt, Fz(:,i), t);
87 end
88
89 for i = 1:24
90     Fxf_mean(i) = mean(Fxf(3001:10001,i));
91     Fzf_mean(i) = mean(Fzf(3001:10001,i));
92 end
93
94 % Coefficients
95 for i = 1:24
96     cxf(:,i) = lsim(flt, cx(:,i), t);
97     czf(:,i) = lsim(flt, cz(:,i), t);
98 end
99
100 %% Plot Filtered data
101 close all; figure
102 name = [14 17 18.5 20 21.5 23 14 17 18.5 20 21.5 23 14 17 18.5 20 21.5 23
        14 17 18.5 20 21.5 23]
103 for i = 1:24
104     subplot(4,6,i)
105
106     plot(t,cz(:,i), 'k-', t,czf(:,i), 'r-');hold on
107     xlabel('Time [s]','FontSize', 12); ylabel('cZ','FontSize', 12)
108     legend('Raw Data','Filtered Data','location','best');
109     title('Velocity', name(i),'FontSize', 12); grid on
110     ylim([-1.6 0])
111
112 end
113
114 deviation1 = zeros(3,3);
115 for i = 1:24
116     cx_mean(i) = mean(cx(2001:10001,i));
117     cxf_mean(i) = mean(cxf(2001:10001,i));
118     cz_mean(i) = mean(cz(2001:10001,i));
119     czf_mean(i) = mean(czf(2001:10001,i));
120     deviation1(i,1) = abs((cx_mean(i) / cxf_mean(i) - 1) * 100);
121     deviation1(i,2) = abs((cz_mean(i) / czf_mean(i) - 1) * 100);
122 end
123
124 % plot deviation
125 figure
126 subplot(141); bar(RE(1:6), deviation1(1:6,:)); grid on; ylim([0 0.07]);
        xlabel('Reynolds number','FontSize', 12), ylabel('Deviation [%]','
        FontSize', 12); legend('Drag','Downforce','FontSize', 12);
127 subplot(142); bar(RE(7:12), deviation1(7:12,:)); grid on; ylim([0 0.07]);
        xlabel('Reynolds number','FontSize', 12), ylabel('Deviation [%]','
        FontSize', 12); legend('Drag','Downforce','FontSize', 12);

```



```

128 subplot(143); bar(RE(13:18), deviation1(13:18,:)); grid on; ylim([0 0.07])
    ; xlabel('Reynolds number','FontSize', 12), ylabel('Deviation [%]','
    FontSize', 12); legend('Drag','Downforce','FontSize', 12);
129 subplot(144); bar(RE(19:24), deviation1(19:24,:)); grid on; ylim([0 0.07])
    ; xlabel('Reynolds number','FontSize', 12), ylabel('Deviation [%]','
    FontSize', 12); legend('Drag','Downforce','FontSize', 12);

130
131 %% prepare data for excel export
132 cxf_mean = [cxf_mean]'
133
134 czf_mean = [czf_mean]'
135
136 %% Plots of Forces vs Time
137 close all
138 figure
139 subplot(131); plot(t, -Fxf(:,1:6)); legend('RE 8.9 x 10^5','RE 1.1 x 10^6'
    , 'RE 1.2 x 10^6', 'RE 1.3 x 10^6', 'RE 1.4 x 10^6', 'RE 1.5 x 10^6',
    'FontSize', 12); title('Rake 0 deg','FontSize', 12); xlabel('Time [s]',
    'FontSize', 12); ylabel('Drag [N]','FontSize', 12); ylim([5 30]); grid
    on
140 subplot(132); plot(t, -Fxf(:,7:12)); legend('RE 8.9 x 10^5','RE 1.1 x 10^6'
    , 'RE 1.2 x 10^6', 'RE 1.3 x 10^6', 'RE 1.4 x 10^6', 'RE 1.5 x 10^6',
    'FontSize', 12); title('Rake 1 deg','FontSize', 12); xlabel('Time [s]',
    'FontSize', 12); ylabel('Drag [N]','FontSize', 12); ylim([5 30]); grid
    on
141 subplot(133); plot(t, -Fxf(:,13:18)); legend('RE 8.9 x 10^5','RE 1.1 x
    10^6', 'RE 1.2 x 10^6', 'RE 1.3 x 10^6', 'RE 1.4 x 10^6', 'RE 1.5 x
    10^6','FontSize', 12); title('Rake 2 deg','FontSize', 12); xlabel('Time
    [s]','FontSize', 12); ylabel('Drag [N]','FontSize', 12); ylim([5 30]);
    grid on
142 subplot(133); plot(t, -Fxf(:,19:24)); legend('RE 8.9 x 10^5','RE 1.1 x
    10^6', 'RE 1.2 x 10^6', 'RE 1.3 x 10^6', 'RE 1.4 x 10^6', 'RE 1.5 x
    10^6','FontSize', 12); title('Rake 3 deg','FontSize', 12); xlabel('Time
    [s]','FontSize', 12); ylabel('Drag [N]','FontSize', 12); ylim([5 30]);
    grid on

143
144 figure
145 subplot(131); plot(t, Fzf(:,1:6)); legend('RE 8.9 x 10^5','RE 1.1 x 10^6',
    'RE 1.2 x 10^6', 'RE 1.3 x 10^6', 'RE 1.4 x 10^6', 'RE 1.5 x 10^6',
    'FontSize', 12); title('Rake 0 deg','FontSize', 12); xlabel('Time [s]');
    ylabel('Downforce [N]','FontSize', 12); ylim([-50 0]); grid on
146 subplot(132); plot(t, Fzf(:,7:12)); legend('RE 8.9 x 10^5','RE 1.1 x 10^6'
    , 'RE 1.2 x 10^6', 'RE 1.3 x 10^6', 'RE 1.4 x 10^6', 'RE 1.5 x 10^6',
    'FontSize', 12); title('Rake 1 deg'); xlabel('Time [s]','FontSize', 12);
    ylabel('Downforce [N]','FontSize', 12); ylim([-50 0]); grid on
147 subplot(133); plot(t, Fzf(:,13:18)); legend('RE 8.9 x 10^5','RE 1.1 x 10^6'
    , 'RE 1.2 x 10^6', 'RE 1.3 x 10^6', 'RE 1.4 x 10^6', 'RE 1.5 x 10^6',
    'FontSize', 12); title('Rake 2 deg'); xlabel('Time [s]','FontSize', 12);
    ylabel('Downforce [N]','FontSize', 12); ylim([-50 0]); grid on
148 subplot(133); plot(t, Fzf(:,19:24)); legend('RE 8.9 x 10^5','RE 1.1 x 10^6'
    , 'RE 1.2 x 10^6', 'RE 1.3 x 10^6', 'RE 1.4 x 10^6', 'RE 1.5 x 10^6',
    'FontSize', 12); title('Rake 3 deg'); xlabel('Time [s]','FontSize', 12);
    ylabel('Downforce [N]','FontSize', 12); ylim([-50 0]); grid on

149
150 %% Standarddeviation
151 std1 = zeros(1,6);
152 for i = 1:6
153     std1(i) = std(cxf(2000:end,i))
154 end
155
156 std2 = zeros(1,12);
157 for i = 1:12
158     std2(i) = std(cxf2(2000:end,i))

```

```

159 end
160
161 figure
162 subplot(221); bar(name(1:3), std1(1:3)); title('Rake 0 deg')
163 subplot(222); bar(name(4:6), std1(4:6)); title('Rake 1 deg')
164 subplot(223); bar(name2(1:6), std2(1:6)); title('Rake 2 deg')
165 subplot(224); bar(name2(7:12), std2(7:12)); title('Rake 3 deg')
166
167 %% Boxplot filtered data vs RE
168 close all; figure
169 % Cx
170 subplot(141); boxplot(-cxf(2000:end,1:6), RE(1:6)); grid on; title('Rake 0
deg', 'FontSize', 12), xlabel('Reynolds number', 'FontSize', 12), ylabel
('Cx', 'FontSize', 12); ylim([0.39 0.45])
171 subplot(142); boxplot(-cxf(2000:end,7:12), RE(7:12)); grid on; title('Rake
1 deg', 'FontSize', 12), xlabel('Reynolds number', 'FontSize', 12),
ylabel('Cx', 'FontSize', 12);ylim([0.39 0.45])
172 subplot(143); boxplot(-cxf(2000:end,13:18), RE(13:18)); grid on; title('
Rake 2 deg', 'FontSize', 12), xlabel('Reynolds number', 'FontSize', 12),
ylabel('Cx', 'FontSize', 12);ylim([0.39 0.45])
173 subplot(144); boxplot(-cxf(2000:end,19:24), RE(19:24)); grid on; title('
Rake 3 deg', 'FontSize', 12), xlabel('Reynolds number', 'FontSize', 12),
ylabel('Cx', 'FontSize', 12);ylim([0.39 0.45])
174
175 % Cz
176 figure
177 subplot(141); boxplot(czf(2000:end,1:6), RE(1:6)); grid on; title('Rake 0
deg', 'FontSize', 12), xlabel('Reynolds number', 'FontSize', 12), ylabel(
'Cz', 'FontSize', 12); ylim([-0.8 -0.74])
178 subplot(142); boxplot(czf(2000:end,7:12), RE(7:12)); grid on; title('Rake
1 deg', 'FontSize', 12), xlabel('Reynolds number', 'FontSize', 12),
ylabel('Cz', 'FontSize', 12); ylim([-0.8 -0.74])
179 subplot(143); boxplot(czf(2000:end,13:18), RE(13:18)); grid on; title('
Rake 2 deg', 'FontSize', 12), xlabel('Reynolds number', 'FontSize', 12),
ylabel('Cz', 'FontSize', 12);ylim([-0.8 -0.74])
180 subplot(144); boxplot(czf(2000:end,19:24), RE(19:24)); grid on; title('
Rake 3 deg', 'FontSize', 12), xlabel('Reynolds number', 'FontSize', 12),
ylabel('Cz', 'FontSize', 12);ylim([-0.8 -0.74])
181 %% Plots of Coefficients vs RE
182
183 close all
184
185 figure
186 plot(RE(1:6), -cxf_mean(1:6), 'o-', 'color', 'k'); hold on
187 plot(RE(7:12), -cxf_mean(7:12), 'x-', 'color', 'k');
188 plot(RE(13:18), -cxf_mean(13:18), 'diamond-', 'color', 'k');
189 plot(RE(19:24), -cxf_mean(19:24), 'square-', 'color', 'k');
190 legend('0 deg Rake', '1 deg Rake', '2 deg Rake', '3 deg Rake', 'FontSize',
12); xlabel('Reynolds number', 'FontSize', 12); ylabel('Cx', 'FontSize',
12)
191 % ylim([-0.12 -0.09])
192 grid on
193
194 figure
195 plot(RE(1:6), czf_mean(1:6), 'o-', 'color', 'k'); hold on
196 plot(RE(7:12), czf_mean(7:12), 'x-', 'color', 'k');
197 plot(RE(13:18), czf_mean(13:18), 'diamond-', 'color', 'k');
198 plot(RE(19:24), czf_mean(19:24), 'square-', 'color', 'k');
199 legend('0 deg Rake', '1 deg Rake', '2 deg Rake', '3 deg Rake', 'FontSize',
12); xlabel('Reynolds number', 'FontSize', 12); ylabel('Cz', 'FontSize',
12)
200 % ylim([-0.12 -0.09])
201 grid on

```

```

202
203 %% Boxplot Coefficients vs Rake
204 close all;
205 rakes1 = [0 1 2 3];
206
207 % Cx
208 box_cx1 = zeros(6,4);
209 box_cx1(:,1) = -cxf_mean(1:6);
210 box_cx1(:,2) = -cxf_mean(7:12);
211 box_cx1(:,3) = -cxf_mean(13:18);
212 box_cx1(:,4) = -cxf_mean(19:24);
213
214 figure
215 boxplot(box_cx1, rakes1); xlabel('rake angle','FontSize', 12); ylabel('Cx'
    , 'FontSize', 12); title('Drag vs Rake Angle','FontSize', 12); grid on;
216
217 % Cz
218 box_cz1 = zeros(6,4);
219 box_cz1(:,1) = czf_mean(1:6);
220 box_cz1(:,2) = czf_mean(7:12);
221 box_cz1(:,3) = czf_mean(13:18);
222 box_cz1(:,4) = czf_mean(19:24);
223
224 figure
225 boxplot(box_cz1, rakes1); xlabel('rake angle','FontSize', 12); ylabel('Cz'
    , 'FontSize', 12); title('Downforce vs Rake Angle','FontSize', 12); grid
    on;
226
227 %% plot coefficients average vs rake
228
229 close all; clc;
230 cxf_plot = zeros(1,4);
231 czf_plot = zeros(1,4);
232
233 for i = 1:4
234     cxf_plot(i) = cxf_mean(6*i);
235     czf_plot(i) = czf_mean(6*i);
236 end
237
238 plot(rakes1, czf_plot); hold on; ylabel('Cz')
239 yyaxis right
240 plot(rakes1, -cxf_plot); grid on; ylabel('Cx')
241
242 %% Pressure calculation
243 % Initialize the cell array to store the data arrays
244 p_stat_array = cell(24, 1);
245
246 % Loop over the datasets
247 % gauge pressure
248 for i = 28:51
249     % Access the columns from Pressure_Scanner18 to Pressure_Scanner49 for
        the current dataset
250     columns = 19:44;
251
252     data_i = eval(sprintf('data_c%d', i));
253
254     % Extract the data and convert it to a numeric array
255     p_gauge = table2array(data_i(x_starts(i-27):x_ends(i-27), columns));
256
257     % Store the data array in the cell array
258     p_gauge_array{i-27} = abs(p_gauge);
259 end
260

```

```

261 % calculate mean pressure
262 p_gauge_mean = zeros(26,24);
263 for i = 28:51
264     p_gauge_mean(:,i-27) = mean(p_gauge_array{i-27});
265 end
266
267 % exclude failed sensors
268 p_gauge_mean = [p_gauge_mean(1:4,:); p_gauge_mean(6:16,:); p_gauge_mean
    (18:26,:)];
269
270 p_ref = [];
271 for i = 28:51
272     % extract data from the i-th dataset
273     data_i = eval(sprintf('data_c%d', i));
274     p_ref(:,0+i-27) = mean(data_i.Patm(x_starts(i-27):x_ends(i-27)));
275 end
276
277 ps = p_ref - p_gauge_mean;
278
279 %% calculation pressure coefficient
280 p_inf = [];
281 for i = 28:51
282     % extract data from the i-th dataset
283     data_i = eval(sprintf('data_c%d', i));
284     p_inf(:,0+i-27) = mean(data_i.Pinf(x_starts(i-27):x_ends(i-27)));
285 end
286
287 q_inf = [];
288 for i = 28:51
289     % extract data from the i-th dataset
290     data_i = eval(sprintf('data_c%d', i));
291     q_inf(:,0+i-27) = mean(data_i.q(x_starts(i-27):x_ends(i-27)));
292 end
293
294 cp = [];
295
296 for i = 28:51
297     cp(:,i-27) = (ps(:,i-27) - p_inf(i-27)) ./ q_inf(i-27);
298 end
299
300 x = ps - p_inf;
301
302 %% plot pressure
303 clc; close all
304 load static_ports_corrected.mat
305 x_ports = x_static_ports(:,1) ./ 728;
306
307 figure
308 plot(x_ports, cp(:,6)); hold on
309 plot(x_ports, cp(:,12));
310 plot(x_ports, cp(:,18));
311 plot(x_ports, cp(:,24));
312 legend('Rake 0', 'Rake 1', 'Rake 2', 'Rake 3', 'FontSize', 12)
313 grid on
314 xlabel('X/c', 'FontSize', 12); ylabel('Cp', 'FontSize', 12)

```

### C.3.5 Overall Comparison

```

1 clc; clear;
2 load comparison_all.mat; load data_all.mat
3
4 %% Init

```

```

5 front_RH = zeros(4,3);
6 front_RH(:,1) = table2array(data_all(1:4,2));
7 front_RH(:,2) = table2array(data_all(5:8,2));
8 front_RH(:,3) = table2array(data_all(9:12,2));
9
10 % rear Ride Height
11 rear_RH = zeros(4,3);
12 rear_RH(:,1) = table2array(data_all(1:4,3));
13 rear_RH(:,2) = table2array(data_all(5:8,3));
14 rear_RH(:,3) = table2array(data_all(9:12,3));
15
16 % Cz
17 cz = zeros(4,3);
18 cz(:,1) = table2array(data_all(1:4,4));
19 cz(:,2) = table2array(data_all(5:8,4));
20 cz(:,3) = table2array(data_all(9:12,4));
21 cz = cz .* -1
22
23 % Cx
24 cx = zeros(4,3);
25 cx(:,1) = table2array(data_all(1:4,5));
26 cx(:,2) = table2array(data_all(5:8,5));
27 cx(:,3) = table2array(data_all(9:12,5));
28
29 % Efficiency
30 eff = - cz ./ cx
31 %% comparison of all ride heights
32 % plot Cz vs Ride Height vs
33 close all; figure
34 plot(front_RH(1,:), cz(1,:), 'o-', 'color', 'k'); hold on
35 plot(front_RH(2,:), cz(2,:), 'x-', 'color', 'k')
36 plot(front_RH(3,:), cz(3,:), 'diamond-', 'color', 'k')
37 plot(front_RH(4,:), cz(4,:), 'square-', 'color', 'k')
38 legend('Rake 0', 'Rake 1', 'Rake 2', 'Rake 3', 'location', 'eastoutside'); xlim
    ([7 13]); ylim([0.62 0.79]);
39 xlabel('Ride Height [mm]'); ylabel('-Cz')
40 grid on
41
42 figure
43 plot(front_RH(1,:), eff(1,:), 'o-', 'color', 'k'); hold on
44 plot(front_RH(2,:), eff(2,:), 'x-', 'color', 'k')
45 plot(front_RH(3,:), eff(3,:), 'diamond-', 'color', 'k')
46 plot(front_RH(4,:), eff(4,:), 'square-', 'color', 'k')
47 legend('Rake 0', 'Rake 1', 'Rake 2', 'Rake 3', 'location', 'eastoutside'); xlim
    ([7 13])
48 xlabel('Ride Height [mm]'); ylabel('-Cz/Cx')
49 grid on
50
51 %% Rear RH vs front RH vs Cz
52 close all; figure
53 contourf(rear_RH, front_RH, cz, ShowText="on")
54 xlabel('rear ride height [mm]')
55 ylabel('front ride height [mm]')
56 a = colorbar; a.Label.String = '-Cz'; grid on
57
58 %% Rear RH vs front RH vs Cz/Cx
59 close all; figure
60 contourf(rear_RH, front_RH, eff, ShowText='on')
61 xlabel('rear ride height [mm]')
62 ylabel('front ride height [mm]')
63 a = colorbar;
64 a.Label.String = '-Cz/Cx';
65 grid on

```

```

66
67 %% Cz vs Cx
68 close all; figure
69 plot(-cx(1,:), cz(1,:), 'o-', 'color', 'k'); hold on
70 plot(-cx(2,:), cz(2,:), 'x-', 'color', 'k')
71 plot(-cx(3,:), cz(3,:), 'diamond-', 'color', 'k')
72 plot(-cx(4,:), cz(4,:), 'square-', 'color', 'k')
73 legend('Rake 0', 'Rake 1', 'Rake 2', 'Rake 3', 'location', 'eastoutside');
74 xlabel('Cx'); ylabel('-Cz')
75 grid on

```

### C.3.6 Pressure Distribution

```

1 clc; clear; close all;
2 load data_RH75.mat; load data_RH100.mat ;load data_RH125.mat; load
  data_downforce_dis.mat; load data_all.mat
3
4 %% Pressure distribution
5 clc; close all
6 % p_stat = [];
7 int = 10000;
8 x_starts = [103118; 82886; 116206; 132029; 62103; 100122; 81754; 126792;
  376576; 65076; 180074; 168671; 232335; 141053; 62082; 270415; 63356;
  66036; ...
9           80586; 392404; 79008; 119276; 122139; 109276; 89671; 91463;
  63144; ...
10          58874; 62482; 58153; 56562; 60375; 55856; 61627; 54776; 53456;
  54762; 58576; 49767; 51897; 51318; 51358; 50890; 58201; 56068; 44274;
  57717; 48533; 41047; 41313; 54684; ...
11          87242; 88275; 59766];
12 x_ends = x_starts + int;
13
14 % Initialize the cell array to store the data arrays
15 p_stat_array = cell(54, 1);
16
17 % Loop over the datasets
18 % gauge pressure
19 for i = 1:54
20     % Access the columns from Pressure_Scanner18 to Pressure_Scanner49 for
  the current dataset
21     columns = 19:44;
22
23     data_i = eval(sprintf('data_c%d', i));
24
25     % Extract the data and convert it to a numeric array
26     p_gauge = table2array(data_i(x_starts(i):x_ends(i), columns));
27
28     % Store the data array in the cell array
29     p_gauge_array{i} = abs(p_gauge);
30 end
31
32 % calculate mean pressure
33 p_gauge_mean = zeros(26,54);
34 for i = 1:54
35     p_gauge_mean(:,i) = mean(p_gauge_array{i});
36 end
37
38 % exclude failed sensors
39 p_gauge_mean = [p_gauge_mean(1:4,:); p_gauge_mean(6:16,:); p_gauge_mean
  (18:26,:)];
40
41 p_ref = [];

```



```

42 for i = 1:54
43     % extract data from the i-th dataset
44     data_i = eval(sprintf('data_c%d', i));
45     p_ref(:,0+i) = mean(data_i.Patm(x_starts(i):x_ends(i)));
46 end
47
48 ps = p_ref - p_gauge_mean;
49
50 %% calculation pressure coefficient
51 p_inf = [];
52 for i = 1:54
53     % extract data from the i-th dataset
54     data_i = eval(sprintf('data_c%d', i));
55     p_inf(:,0+i) = mean(data_i.Pinf(x_starts(i):x_ends(i)));
56 end
57
58 q_inf = [];
59 for i = 1:54
60     % extract data from the i-th dataset
61     data_i = eval(sprintf('data_c%d', i));
62     q_inf(:,0+i) = mean(data_i.q(x_starts(i):x_ends(i)));
63 end
64
65 cp = [];
66
67 for i = 1:54
68     cp(:,i) = (ps(:,i) - p_inf(i)) ./ q_inf(i);
69 end
70
71 x1 = ps - p_inf;
72
73 %% plot pressure
74 clc; close all
75 load static_ports_corrected.mat
76 x_ports = x_static_ports(:,1) ./ 728;
77
78 figure
79 % subplot(131);
80 plot(x_ports, cp(:, 25:27), 'r'); grid on; hold on
81 plot(x_ports, cp(:, 52:54), 'k')
82 % subplot(132); plot(x_ports, cp(:,19:27)); grid on
83 % subplot(133); plot(x_ports, cp(:,28:51)); grid on
84
85 xlabel('X/c'); ylabel('c_p')
86
87 %% error calculation
88 clc; close all
89 cp1 = cp(:,25:27);
90 cp2 = cp(:,52:54);
91 error = (abs(cp1 ./ cp2 - 1)) .* 100
92
93 figure
94 xlab = {'1','2','3','4','5','6','7','8','9','10','11','12','13','14','15',
95         '16','17','18','19','20','21','22','23','24'}
96 bar(error)
97 legend('Measurement @ 14m/s', 'Measurement @ 17m/s', 'Measurement @ 20m/s'
98         ); grid on;
99 xlabel('Sensor No. '); ylabel('Error [%]')
100
101 %% reduce data
102 clc, close all
103 % cp
104 % RH 7.5 mm

```

```

103 cp75 = zeros(24,4);
104 cp75(:,1) = cp(:,3);
105 cp75(:,2) = cp(:,6);
106 cp75(:,3) = cp(:,12);
107 cp75(:,4) = cp(:,18);
108
109 % RH 10.0 mm
110 cp100 = zeros(24,3);
111 cp100(:,1) = cp(:,21);
112 cp100(:,2) = cp(:,24);
113 cp100(:,3) = cp(:,27);
114
115 % RH 12.0 mm
116 cp125 = zeros(24,4);
117 cp125(:,1) = cp(:,33);
118 cp125(:,2) = cp(:,39);
119 cp125(:,3) = cp(:,45);
120 cp125(:,4) = cp(:,51);
121
122 % ps
123 % RH 7.5 mm
124 ps75 = zeros(24,4);
125 ps75(:,1) = ps(:,3);
126 ps75(:,2) = ps(:,6);
127 ps75(:,3) = ps(:,12);
128 ps75(:,4) = ps(:,18);
129
130 % RH 10.0 mm
131 ps100 = zeros(24,3);
132 ps100(:,1) = ps(:,21);
133 ps100(:,2) = ps(:,24);
134 ps100(:,3) = ps(:,27);
135
136 % RH 12.0 mm
137 ps125 = zeros(24,4);
138 ps125(:,1) = ps(:,33);
139 ps125(:,2) = ps(:,39);
140 ps125(:,3) = ps(:,45);
141 ps125(:,4) = ps(:,51);
142
143 ps_new = zeros(24,11);
144 ps_new(:,1:4) = ps75
145 ps_new(:,5:7) = ps100
146 ps_new(:,8:11) = ps125
147
148 % Fz
149 % RH 7.5 mm
150 Fz_total = table2array(data_downforce_dis(:,1))
151 Fz_new = zeros(1,11);
152 Fz_new(:,1) = Fz_total(3);
153 Fz_new(:,2) = Fz_total(6);
154 Fz_new(:,3) = Fz_total(12);
155 Fz_new(:,4) = Fz_total(18);
156 Fz_new(:,5) = Fz_total(21);
157 Fz_new(:,6) = Fz_total(24);
158 Fz_new(:,7) = Fz_total(27);
159 Fz_new(:,8) = Fz_total(33);
160 Fz_new(:,9) = Fz_total(39);
161 Fz_new(:,10) = Fz_total(45);
162 Fz_new(:,11) = Fz_total(51);
163
164 Load static_ports_corrected.mat
165

```

```

166 figure;
167 subplot(311); plot(x_ports,cp75); legend('Rake 0','Rake 1','Rake 2','Rake
    3','location','eastoutside'); title('Ride Height 7.5 mm'); grid on
168 subplot(312); plot(x_ports,cp100); legend('Rake 0','Rake 1','Rake 2','
    location','eastoutside'); title('Ride Height 10.0 mm'); grid on
169 subplot(313); plot(x_ports,cp125); legend('Rake 0','Rake 1','Rake 2','Rake
    3','location','eastoutside'); title('Ride Height 12.5 mm'); grid on
170
171 %% plot cp again
172
173 %% determine CoP
174 my      = ps_new .* (x_static_ports ./ 1000); % calculate the moments to
    the reference point nose
175 my_sum = sum(my); % sum up all the moments
176 ps_sum = sum(ps_new);
177
178 format long
179 cop = my_sum ./ ps_sum;
180 %% downforce distribution
181 close all
182
183 d_total = 0.364; % [mm] distance between axles
184 d_front = cop - 0.25; % [mm] distance to front axle
185 d_rear  = 0.650 - 0.036 - cop; % [mm] distance to rear axle
186
187 Fz_rear = (Fz_new ./ d_total) .* d_front;
188 Fz_front= (Fz_new ./ d_total) .* d_rear;
189
190 Fz_dis = zeros(2, 11);
191 Fz_dis(2,:) = Fz_front ./ Fz_new .* 100;
192 Fz_dis(1,:) = Fz_rear  ./ Fz_new .* 100;
193
194 figure
195 Configuration = 1:1:11;
196 x1 = {'RH 7.5 mm - Rake 0 deg', 'RH 7.5 mm - Rake 1 deg', 'RH 7.5 mm -
    Rake 2 deg', 'RH 7.5 mm - Rake 3 deg', ...
197      'RH 10.0 mm - Rake 0 deg', 'RH 10.0 mm - Rake 1 deg', 'RH 10.0 mm -
    Rake 2 deg', ...
198      'RH 12.5 mm - Rake 0 deg', 'RH 12.5 mm - Rake 1 deg', 'RH 12.5 mm -
    Rake 2 deg', 'RH 12.5 mm - Rake 3 deg'}
199 bar(Configuration, Fz_dis,'stacked'), legend('percentage of force on rear
    axis','percentage of force on front axis');
200 ylim([45.8 45.835]), xlabel('Configuration'), ylabel('Percentage of
    Downforce Distribution [%]');
201 xticklabels(x1);xticks(Configuration), xtickangle(45)
202 text(1:length(Fz_dis(2,:)),Fz_dis(2,:),num2str(Fz_dis(2,:)),'vert','
    bottom','horiz','center');
203 box off; grid on
204
205 %% contour plot downforce distribution
206 load RHforcontour.mat
207 Fz_dis_contour = zeros(4,3)
208 Fz_dis_contour(:,1) = Fz_dis(2,1:4)
209 Fz_dis_contour(1:3,2) = Fz_dis(2,5:7)
210 Fz_dis_contour(:,3) = Fz_dis(2,8:11)
211 Fz_dis_contour(4,2) = mean(Fz_dis_contour(1:3,2)) % interpolated with
    average !!!
212
213 close all; figure
214 contourf(rear_RH, front_RH, Fz_dis_contour, ShowText='on')
215 xlabel('rear ride height [mm]')
216 ylabel('front ride height [mm]')
217 a = colorbar;

```

```
218 a.Label.String = '% on front end';  
219 grid on
```

## Appendix D

# Additional Plots

### D.1 Filtering

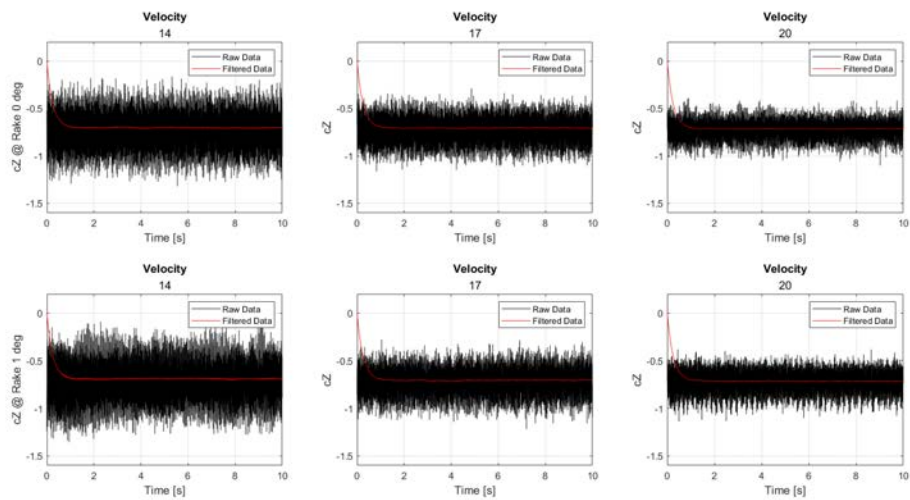


FIGURE D.1: Filtered and raw data of the downforce coefficient for RH 7.5mm, RA 0° and 1°

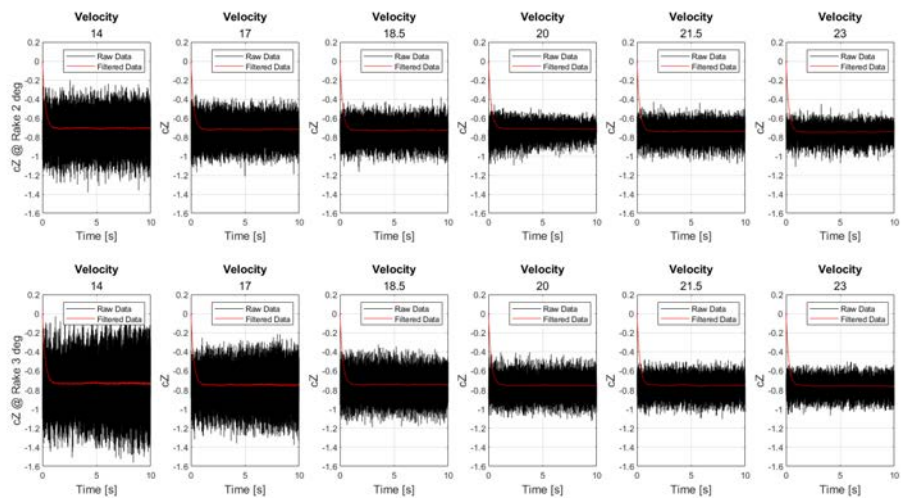


FIGURE D.2: Filtered and raw data of the downforce coefficient for RH 7.5mm, RA 2° and 3°

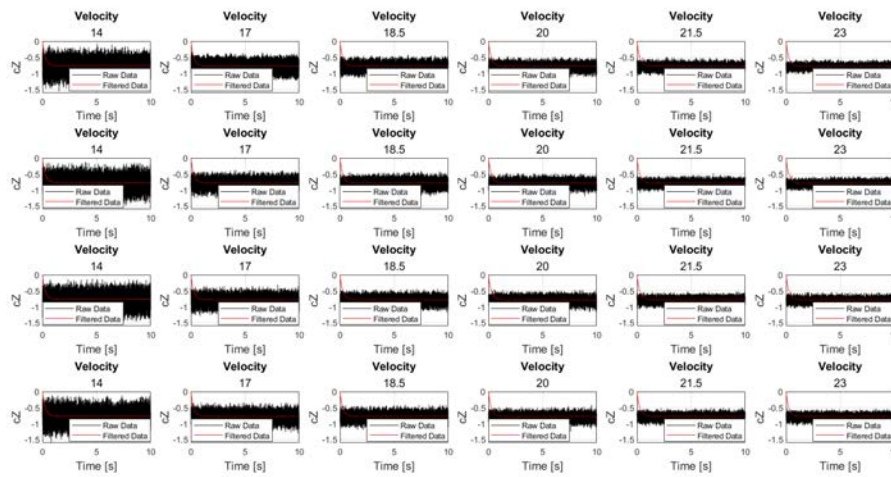


FIGURE D.3: Filtered and raw data of the downforce coefficient for RH 12.5mm

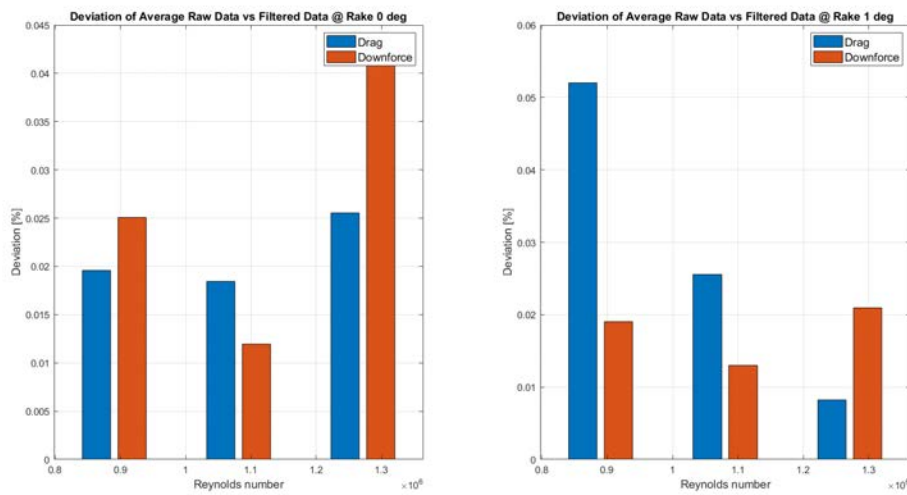


FIGURE D.4: Deviation between raw and filtered data for RH 7.5 mm, RA 0° and 1°

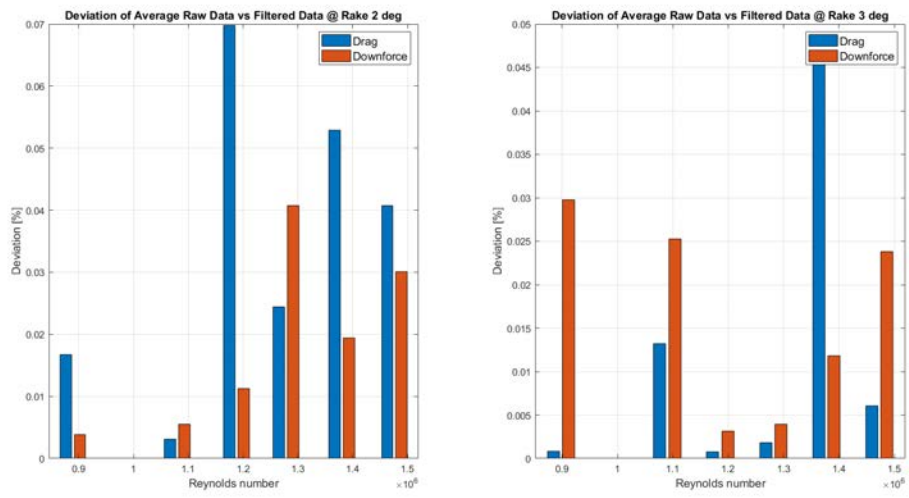


FIGURE D.5: Deviation between raw and filtered data for RH 7.5 mm, RA 2° and 3°

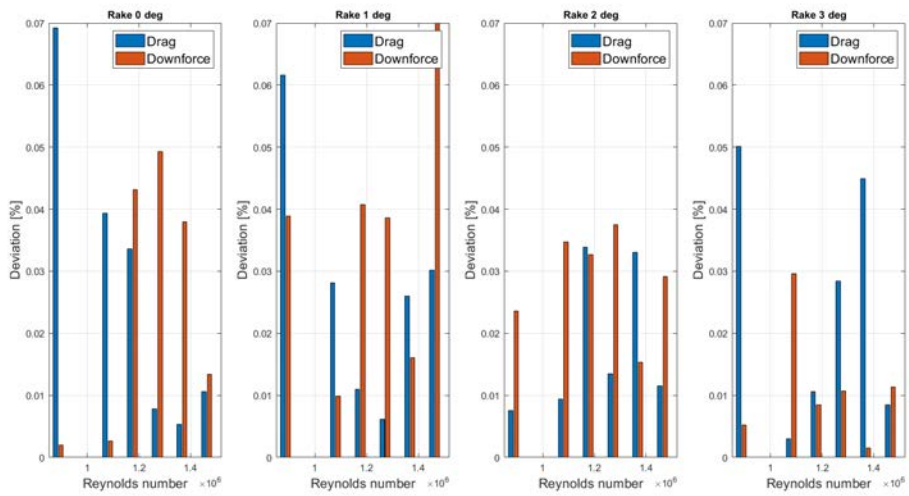


FIGURE D.6: Deviation between raw and filtered data for RH 12.5mm



## D.2 Boxplots

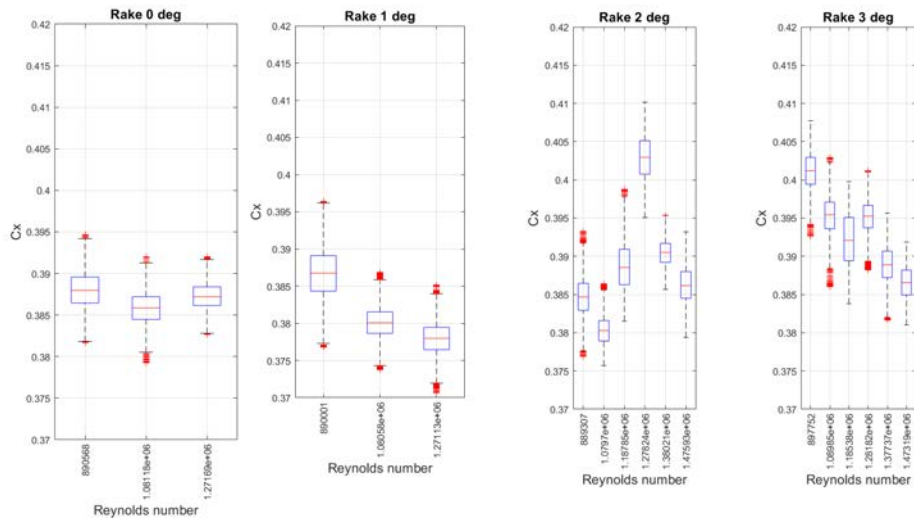


FIGURE D.7: Boxplot of the filtered drag coefficients at RH 7.5mm

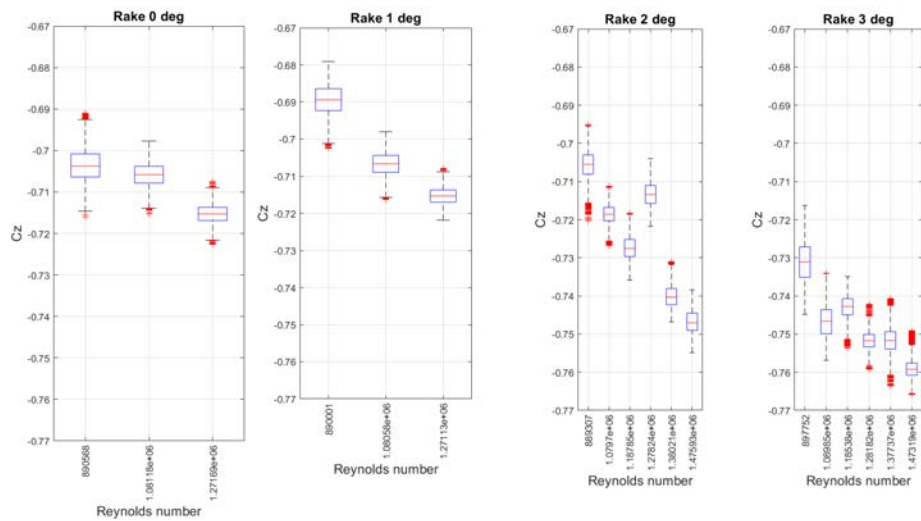


FIGURE D.8: Boxplot of the filtered downforce coefficients at RH 7.5mm

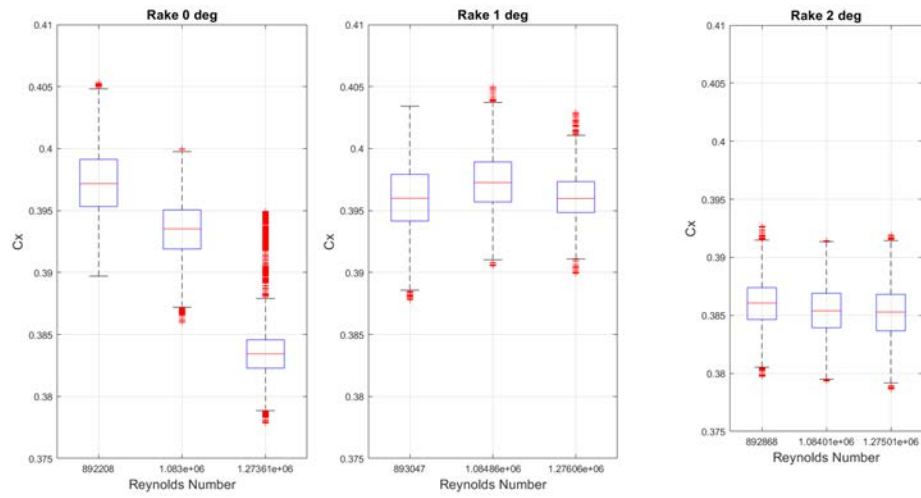


FIGURE D.9: Boxplot of the filtered drag coefficients at RH 10 mm

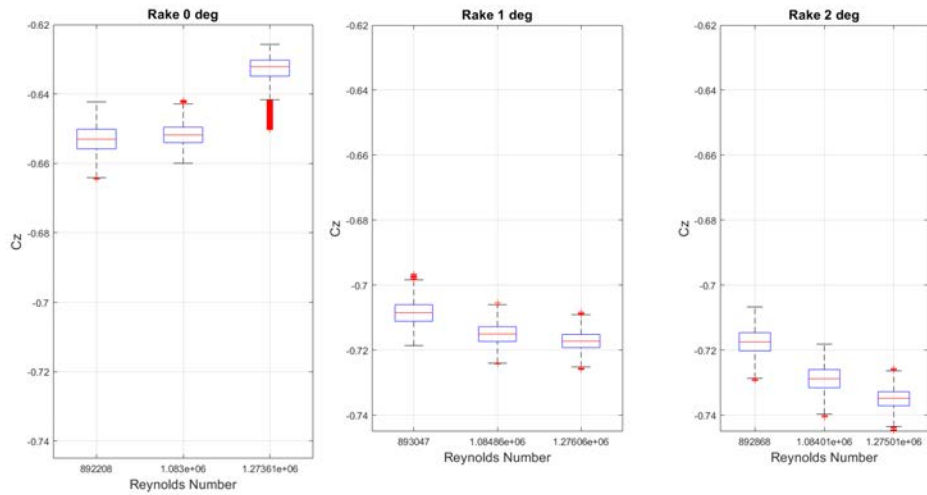


FIGURE D.10: Boxplot of the filtered downforce coefficients at RH 10 mm

### D.3 Line Plots

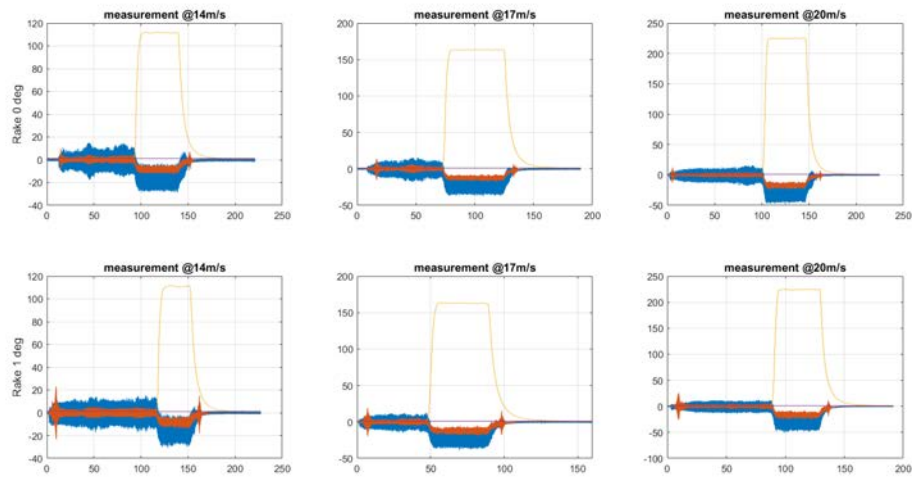


FIGURE D.11: Line plots of  $F_x$ ,  $F_z$  and  $q$  for RH 7.5 mm

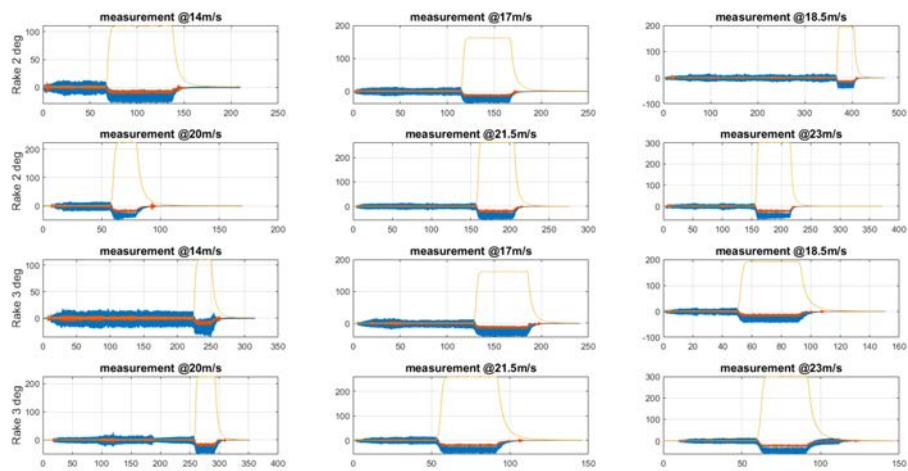


FIGURE D.12: Line plots of  $F_x$ ,  $F_z$  and  $q$  for RH 7.5 mm

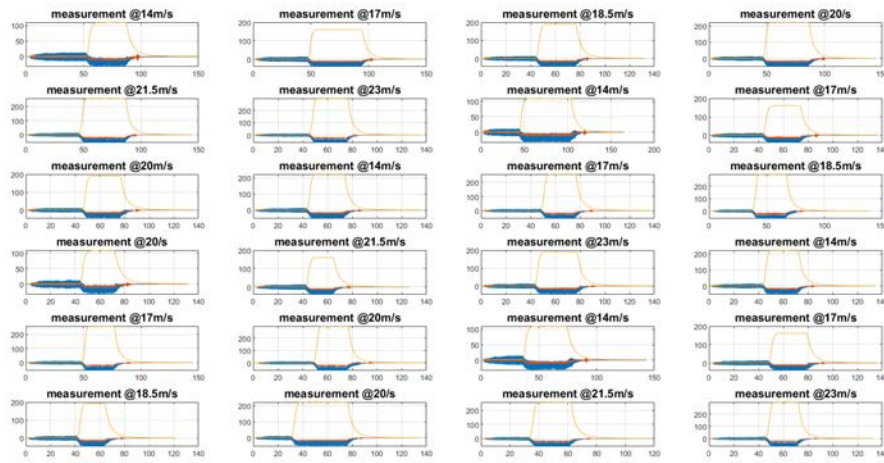


FIGURE D.13: Line plots of  $F_x$ ,  $F_z$  and  $q$  for RH 12.5 mm

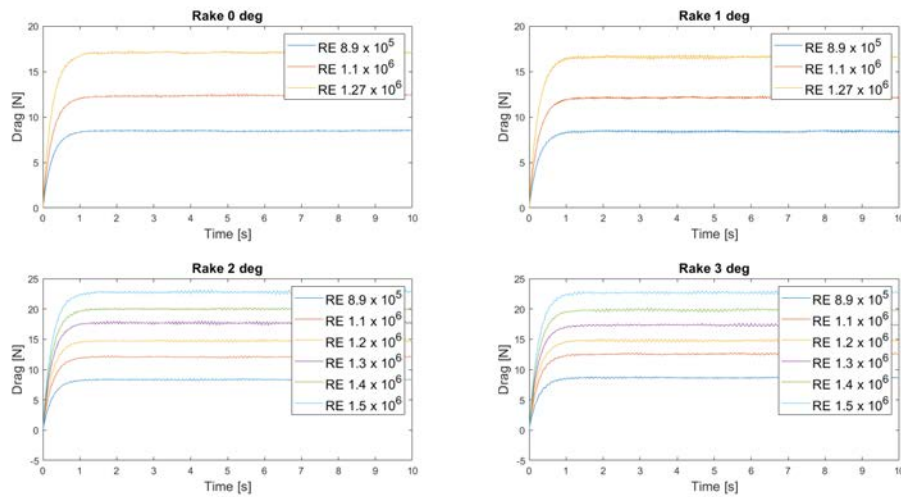


FIGURE D.14: Line plots of filtered  $F_x$  in the measurement range for RH 7.5 mm

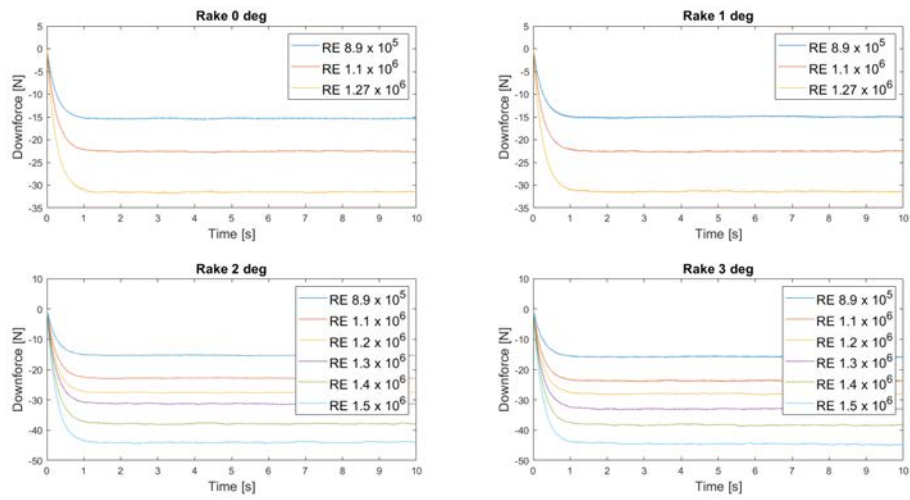


FIGURE D.15: Line plots of filtered  $F_z$  in the measurement range for RH 7.5 mm

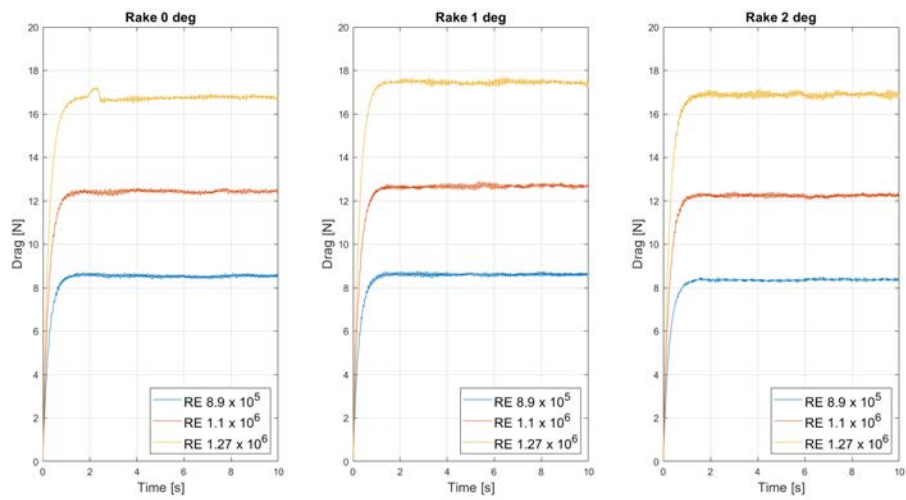


FIGURE D.16: Line plots of filtered  $F_x$  in the measurement range for RH 10 mm

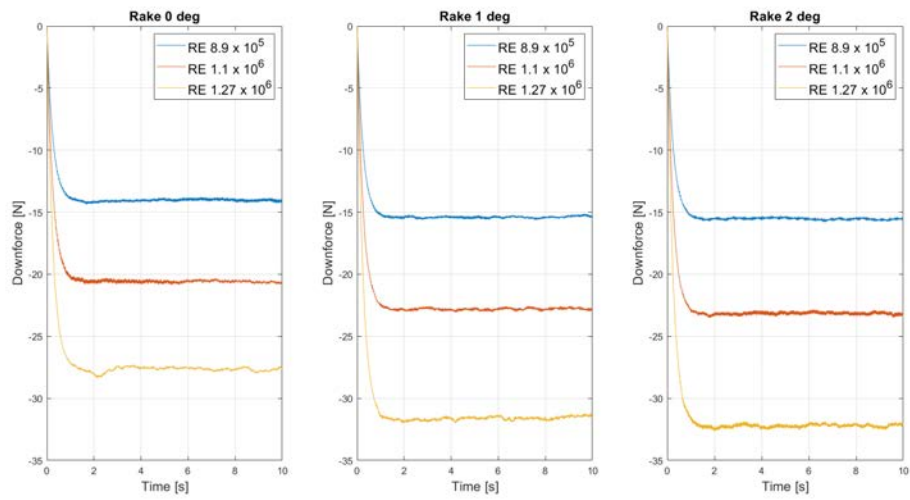


FIGURE D.17: Line plots of filtered  $F_z$  in the measurement range for RH 10 mm

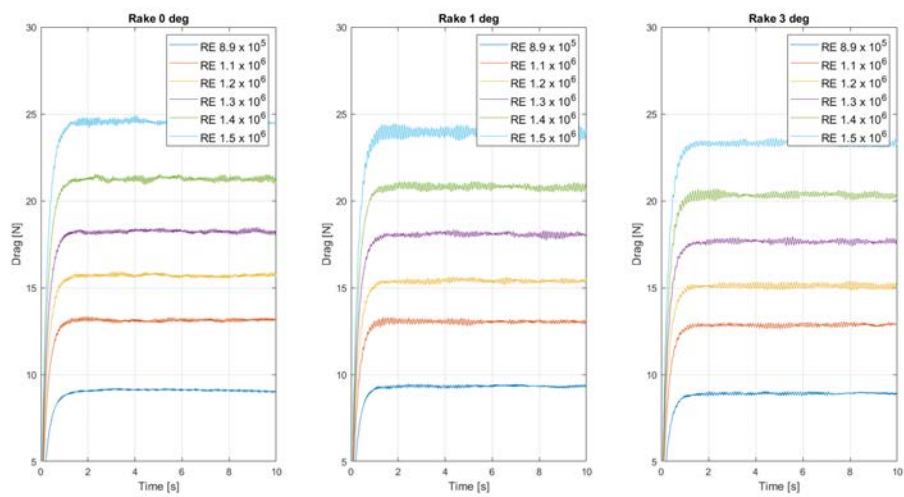


FIGURE D.18: Line plots of filtered  $F_x$  in the measurement range for RH 12.5 mm

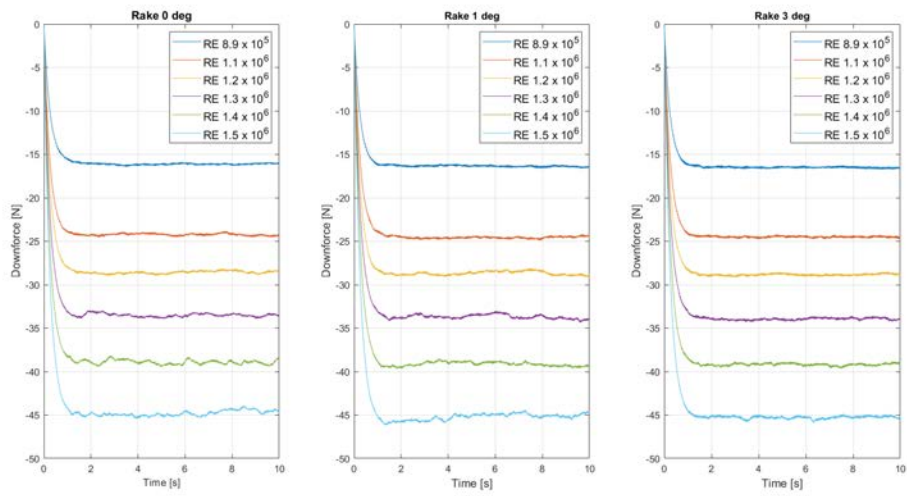


FIGURE D.19: Line plots of filtered  $F_z$  in the measurement range for RH 12.5 mm